ÇUKUROVA UNIVERSITY
INSTITUTE OF NATURAL AND APPLIED SCIENCES

PhD. THESIS

Çağlar ZORBİLMEZ

MEASUREMENT OF ENERGY DENSITY AS A FUNCTION OF PSEUDORAPIDITY IN PROTON-PROTON COLLISIONS AT $\sqrt{s}$= 13 TeV WITH THE CMS EXPERIMENT AT THE LHC

DEPARTMENT OF PHYSICS

ADANA-2019

ÇUKUROVA UNIVERSITY
INSTITUTE OF NATURAL AND APPLIED SCIENCES

MEASUREMENT OF ENERG DENSITY AS A FUNCTION OF PSEUDORAPIDITY IN PROTON-PROTON COLLISIONS AT $\sqrt{s}$= 13 TeV WITH THE CMS EXPERIMENT AT THE LHC

Çağlar ZORBILMEZ

PhD THESIS

DEPARTMENT OF PHYSICS

We certify that the thesis titled above was reviewed and approved for the award of degree of the Doctor of Philosophy by the board of jury on 11/10/2019.

…………………..	………..………………	....
Prof. Dr. Eda EŞKUT SUPERVISOR	Prof. Dr. Ayşe POLATÖZ MEMBER	Prof. Dr. Aysel KAYIŞ TOPAKSU MEMBER
…………………………....	……………………….......	
Assoc. Prof. Dr. Salim ÇERÇİ MEMBER	Assist. Prof. Dr. İlknur HOŞ MEMBER	

This PhD Thesis is performed in Department of Physics of Institute of Natural And Applied Sciences of Çukurova University.
Registration Number:

Prof. Dr. Mustafa GÖK
Director
Institute of Natural and Applied Sciences

This Study was supported by Çukurova University Scientific Research Fund.Project Number: FDK-2015-3838

To my elder sister.
Pınar Zorbilmez
for her endless love, support and encouragement

ABSTRACT

PhD. THESIS

MEASUREMENT OF ENERGY DENSITY AS A FUNCTION OF PSEUDORAPIDITY IN PROTON-PROTON COLLISONS AT √s = 13 TeV WITH THE CMS EXPERIMENT AT THE LHC

Çağlar ZORBİLMEZ

ÇUKUROVA UNIVERSITY
INSTITUTE OF NATURAL AND APPLIED SCIENCES
DEPARTMENT OF PHYSICS

Supervisor	: Prof. Dr. Eda EŞKUT
II. Supervisor	: Assoc.Prof. Dr. Deniz SUNAR ÇERÇİ
	Year: 2019, Page: 103
Jury	: Prof. Dr. Eda EŞKUT
	: Prof. Dr. Ayşe POLATÖZ
	: Prof. Dr. Aysel KAYIŞ TOPAKSU
	: Assoc. Prof. Dr. Salim ÇERÇİ
	: Asst. Prof. Dr. İlknur HOŞ

In this thesis, measurement of energy density is presented using data which taken through the Compact Muon Solenoid (CMS) detector in proton-proton collision for center of mass energy of √s = 13 TeV. The data have been collected at low luminosity in 2015 without magnetic field. The energy density as well as transverse energy density measurements within the pseudorapidity ranges of $3.15 < |\eta| < 5.2$ and -$6.6 < \eta < -5.2$ is performed. The data used in this analysis were also compared with the data collected with magnetic field at the same energy. The results obtained from analysis and prediction of models that describe high-energy hadronic interactions are compared with each other. All models considered suggest a different form of the pseudorapidity dependence for the energy density compared to that observed in the data. An additional comparison is made with earlier proton-proton collision data at √s = 0.9 TeV and √s = 7 TeV which allows to test the hypothesis of limiting fragmentation.

Key Words: CMS, Energy Density, Transverse Energy Density, Low Luminosity

ÖZ

DOKTORA TEZİ

BHÇ'DE CMS DENEYİ İLE √s = 13 TeV'LİK PROTON-PROTON ÇARPIŞMALARINDA PSÜDORAPİDİTENİN BİR FONKSİYONU OLARAK ENERJİ YOĞUNLUĞUNUN ÖLÇÜLMESİ

Çağlar ZORBİLMEZ

ÇUKUROVA ÜNİVERSİTESİ
FEN BİLİMLERİ ENSTİTÜSÜ
FİZİK ANABİLİM DALI

Danışman : Prof. Dr. Eda EŞKUT
II. Danışman : Doç. Dr. Deniz SUNAR ÇERÇİ
Yıl: 2019, Sayfa: 103
Jüri : Prof. Dr. Eda EŞKUT
: Prof. Dr. Ayşe POLATÖZ
: Prof. Dr. Aysel KAYIŞ TOPAKSU
: Doç. Dr. Salim ÇERÇİ
: Dr. Ögr. Üyesi İlknur HOŞ

Bu tezde, bir proton-proton çarpışmasında, √s=13 TeV'lik kütle merkezi enerjisinde, CMS tarafından alınan veri kullanılarak yapılan enerji akış yoğunluğu ölçümü sunulmaktadır. Veri, 2015 yılında düşük ışıklılık değerinde manyetik alan olmadan toplanmıştır. Hem enerji akışı hem de dik enerji akış yoğunluğu ölçümü $3.15 < |\eta| < 5.2$ ve $-6.6 < \eta < -5.2$ psüdorapidite aralıklarında çalışılmıştır. Analizde kullanılan veri manyetik alanda alınan veri ile karşılaştırılmıştır. Analizden elde edilen sonuçlar ve yüksek-enerjili hadron etkileşimlerini tanımlamak için kullanılan model öngörüleri birbirleri ile karşılaştırılmıştır. Düşünülen bütün modeller verilerde gözlenenlerden farklıdır. Ayrıca daha önce √s = 0.9 TeV ve √s = 7 TeV kütle merkezi enerjilerinde kaydedilmiş proton-proton çarpışma verileri ile de karşılaştırılmıştır. Bu ölçüm sınırlayıcı parçalanma hipotezini test etmeye sağlar.

Anahtar Kelimeler: CMS, Enerji Akış Yoğunluğu, Dik Enerji Akış Yoğunluğu, Düşük Işıklılık

GENİŞLETİLMİŞ ÖZET

İçinde yaşadığımız evren ve evrenin hangi temel yapı taşlarından oluştuğu insanoğlunun en merak ettiği konulardan biridir. Bu merak fiziğin bir alt dalı olan parçacık fiziğinin doğmasını sağlamıştır. 19. yüzyılda J. J Thomson'nun temel parçacıklardan biri olan elektronu keşfetmesi bilim dünyasını heyecanlandırmış ve bunu takip eden yıllarda maddenin temel yapı taşlarını keşfetme yarışı başlamıştır. Hızlandırıcılar ve atmosfere giren kozmik ışınlar kullanılarak birçok parçacık keşfedilmiştir. Bu keşiflerin rehberliğinde bilim insanları bulunan bu parçacıkları 1970'lerde Standart Model (SM) adı verilen kuramsal bir modelde sınıflandırmıştır.

SM, maddeyi oluşturan temel parçacıkları, onların birbirleri ile olan etkileşimlerini ve doğadaki temel kuvvetleri (güçlü, elektromanyetik ve zayıf kuvveti) açıklamakta oldukça başarılı bir kuramdır. SM geliştirilen hızlandırıcılar ve kozmik ışın deneyleri yardımı ile pek çok kez test edilmiştir. SM'ye göre etrafımızda bilinen bütün maddeler fermiyon adı verilen spini 1/2 olan parçacıklardan oluşur. Fermiyonlar, kuarklar ve leptonlar olarak adlandırılan iki sınıfa ayrılır. Bilinen en ünlü lepton ilk keşfedilen elektrondur. Altı tane kuark ve altı tane lepton vardır. Kuarklar yukarı (up-*u)*, aşağı (down-*d*) cazibeli (charm-*c*), acayip (strange- *s*), üst (top-*t*) ve alt (bottom-*b*) kuark olarak adlandırılmıştır. Leptonlar ise elektron *(e)*, elektron nötrinosu (ν_e), müon (μ), müon nötrinosu (ν_μ), tau (τ) ve tau nötrinosudur (ν_τ). SM kuramında tam sayılı spine sahip parçacıklara bozon denir. Bozonlar, etkileşmelere aracılık yapan parçacıklardır. Güçlü etkileşmenin ara parçacıkları gluon (g)'lar, elektromanyetik etkileşmeden sorumlu olan foton (γ) ve zayıf etkileşmenin ara parçacıkları $W^{\pm}$, Z'dir. Yerçekimi kuvveti (gravitasyon) hariç, madde parçacıkları arasındaki bütün kuvvetler SM içinde çok iyi bir şekilde açıklanmıştır. Bu nedenle SM temel parçacıklar ve temel parçacıklar arasındaki etkileşmeleri açıklamakta iyi olsa da hala yanıtlayamadığı "Karanlık madde nedir?", "Büyük patlamadan (Big Bang) sonra evrendeki anti-maddeye ne olmuştur?" gibi birçok soru vardır.

Kuarklar ilk kez 1968 yılında Amerika'daki Stanford Çizgisel Hızlandırıcı (SLAC)'da gerçekleştirilen derin esnek olmayan saçılma (DIS) deneyinde gözlenmiştir. Yüksek enerjili bir elektronun bir protondan saçılması ile oluşan bu süreç aynı zamanda bir hadronun iç yapısı hakkında önemli bilgiler vermektedir. Bu sürecin sonunda Feynman ve Bjorken tarafından 1968'in sonlarında bir model önerilmiştir. Bu modele göre hadronlar parton (kuarklar ve gluonlar) adı verilen temel parçacıkların bağlı durumlarından oluşur. Kuarklar arasındaki etkileşme bir hadronun içindeki partonun momentum dağılım fonksiyonuna bağlıdır. Bu fonksiyon parton dağılım fonksiyonu olarak bilinir.

Kuantum Renk Dinamiği (KRD), SM içinde güçlü etkileşmeleri tanımlayan bir ayar kuramıdır. Elektromanyetik etkileşmelerin kuramı olan kuantum elektro dinamiği (KED)'nde bir elektrik yükü söz konusu iken güçlü etkileşmelerin kuramı KRD'de renk yükleri de vardır. Bu renk yükleri Kırmızı, Mavi ve Yeşil olarak adlandırılır (KMY). KED kuramında karşıt parçacıklar karşıt (zıt) işaretli bir yüke sahiptir. Benzer bir şekilde KRD'de ise karşıt kuarkların zıt işaretli renk yükleri ($\overline{K}, \overline{M}, .\overline{Y}$) vardır. Kuarklar deneysel olarak gözlenmiş olmakla birlikte doğada serbest halde bulunmazlar. Kuarkların serbest halde bulunmayışı renk hapsi hipotezi ile açıklanmaktadır. Bu durum Bölüm 2'de ayrıntılı biçimde tartışılmıştır. KRD'de güçlü etkileşmenin kuvvet taşıyıcısı olan gluon, elektromanyetik etkileşmenin kuvvet taşıyıcısı foton gibi sıfır elektrik yüküne sahiptir. Kuarklar hem bir elektrik hem de bir renk yüküne sahip iken gluonlar sadece bir çift renk (renk-zıt renk) yüküne sahiptir. Ayrıca kuarklar üç renk yüküne sahip iken gluonlar sekiz renk durumda bulunabilirler. Kuarkların ve gluonların renk durumların ayrıntıları da Bölüm 2'de tartışılmıştır.

Deneylerden elde edilen veriler ile kuramsal öngörüleri karşılaştırmak ve etkileşmelerin simülasyonlarını oluşturarak çarpışmalarda oluşan durumları daha iyi açıklayabilmek için Monte Carlo (MC) olay üreteçleri kullanılmaktadır. Bir fizik analizinin daha iyi anlaşılması ve kuramsal çatının geliştirilmesi için MC olaylar ile gerçek verilerin karşılaştırılması önemli fırsatlar sunmaktadır. Bu analizde 2015 yılında CMS deneyinde toplanan gerçek veriler kullanılarak ölçülen ileri bölgedeki enerji ve dik enerji yoğunluğu, çeşitli MC olay üreticinden elde edilen tahminlerle karşılaştırılmıştır. Bu olay üreteçleri farklı ayarlardaki (TuneMONASH2018, CUERP8M1, CUETP8S1 ve MBR) PYTHIA 8, EPOS (versiyon 1.99) ve QGSJETII.4'dir. PYTHIA 8, DGLAP (Dokshitzer-Gribov-Lipatov-Altarelli-Parisi) eşitliğine göre pertürbatif KRD ve parton duşlarında hesaplanan saçılma matrisinin elemanlarına dayanan bir olay üretecidir. EPOS LHC ve QGSJETII olay üreteçleri ise genellikle atmosfere giren kozmik ışınların sebep olduğu hava duşlarını tanımlamak için kullanılır. Analizlerde kullanılan MC üreteçlerinin ayrıntıları Bölüm 2 ve 4'de verilmiştir.

Bu tezde kullanılan deneysel veri Büyük Hadron Çarpıştırıcısı (BHÇ)'ındaki CMS (Compact Muon Solenoid- Sıkı Müon Selonoid), deneyi tarafından toplanmıştır. İsviçre-Fransa sınırında yerin yaklaşık 100 m altında inşa edilen BHÇ dünya üzerindeki en büyük ve en güçlü dairesel parçacık hızlandırıcısıdır. Toplam 10^{34} $cm^{-2}s^{-1}$ ışıklılığa ulaşması hedeflenen BHÇ üzerinde dört büyük deney bulunmaktadır. Bu deneyler halkanın 1 numaralı noktasına yerleştirilen ATLAS (A Toroidal LHC ApparatuS - Büyük Toroidal Detektör) 5 numaralı noktasında bulunan CMS, 8 numaralı noktaya yerleştirilen LHCb (The Large Hadron Collider beauty - Büyük Hadron güzellik Çarpıştırıcı) ve 2 numaralı bölgesinde bulunan ALICE (A Large Ion Collider Experiment – Büyük İyon Çarpıştırıcı Deneyi) dir. Bunlardan CMS ve ATLAS genel amaçlı detektörlerdir ve genel fizik konularını araştırmak için tasarlanmıştır. Diğer deneylerden LHCb, b-fiziği çalışmaları yaparken ALICE ise ağır iyon çarpışmalarına odaklanmıştır.

BHÇ halkasının Fransa'daki Cessy kasabasında yer alan CMS deneyi genel amaçlı fizik konularını araştırmaktadır. CMS deneyinin karakteristik özellikleri kısaltmada kullanılan harfler ile özetlenebilir. CMS ilk harften de anlaşılacağı gibi kompakt (sıkı-katı) bir yapıdadır. Bunun anlamı kütlesine göre büyüklüğü azdır. CMS dedektörü 28,7 m uzunluğunda, 14,6 m yarıçapında ve 14 500 ton ağırlığında soğansı yapıda, sıkıştırılmış silindirik bir geometriye sahiptir. Kısaltmadaki ikinci harf ise CMS deneyinin müonları tespit etme sistemine sahip olduğu anlamındadır. CMS detektörü farklı parçacıkları belirleyebilmek için bazı alt detektörlerden oluşmuştur. Bunlar dedektörün en iç kısmından dışarıya doğru İzleyici sistem, Elektromanyetik Kalorimetre (EKAL), Hadronik Kalorimetre (HKAL) ve Müon sistemidir. CMS kısaltmasının son harfi ise detektörün içinde ilerleyen parçacıkların kimliklerinin belirlenmesi için parçacıkların yollarının bükülmesini sağlayan güçlü solenoid mıknatıstır.

CMS'in alt detektörlerinden olan İzleyici sistem BHÇ'de meydana gelen çarpışmalardan kaynaklanan yüklü parçacıkların izlerinin iyi bir şekilde ölçülmesini sağlamak için tasarlanmıştır. İzleyici sistem etkileşim noktasına en yakın olan bir piksel ve silikon şerit dedektörden oluşmuştur. EKAL ise elektromanyetik olarak etkileşen parçacıkları ölçmek amacı ile tasarlanmıştır. Elektromanyetik fıçı (EB) ve elektromanyetik son kapak (EE) olmak üzere iki bölümden oluşur. CMS detektörünün alt detektörlerinden biri olan HKAL hadron jetleri ve nötrinoları ölçmektedir. HKAL kendi içinde dört alt detektörden oluşur. Bunlar; hadronik fıçı (HB), hadronik dış (HO), hadronik son kapak, (HE) ve ileri hadronik (HF) kalorimerelerdir. Müonların belirlenmesi fizik analizlerinde önemli bir yer tutar. CMS bu bakımdan çok gelişmiş bir müon sistemine sahiptir. Müon sistem üç alt detektörden oluşur. Bu detektörlerin her biri faklı bir teknolojiye sahiptir. Bu detektörler; sürüklenme tüpleri (DT), katot şerit odacıkları (CSC) ve dirençli plaka (RPC) odalarıdır. BHÇ ve CMS hakkında daha ayrıntılı bilgi Bölüm 3'de verilmiştir.

Bölüm 4'de 2015 yılında CMS'de, 13 TeV'lik kütle merkezi enerjisinde, manyetik alan olmadan (B = 0 T), düşük yığınlıkta alınan veri kullanılarak psüdorapiditenin bir fonksiyonu olarak ileri bölgedeki (HF ve CASTOR) enerji ve dik enerji yoğunluğu ölçümü tartışılmıştır. İleri bölgede enerji akış yoğunluğunun ölçülmesi çoklu parton etkileşmeleri (MPI) ve ilk durum radyasyonuna karşı oldukça duyarlıdır. Ayrıca bu analiz MC olay üreteçlerine giriş parametrelerin ayarlanması ve ölçülen bölgedeki kalorimetrelerin performansları hakkında oldukça önemli bilgiler verir.

Bu tez çerçevesinde gerçekleştirilen analiz sonuçları CMS AN-2015/119 ve CMS PAS FSQ-15-006 makalelerinde detaylı biçimde verilmektedir. Analizden elde edilen sonuçlar Ekim 2018'de Türkiye Atom Enerjisi Kurumu (TAEK) bünyesinde geçekleştirilen 1. Ulusal CERN ile İlgili Faaliyetler Çalıştay'ında sunulmuştur. Ayrıca, elde edilen analiz sonuçları uluslararası The European Physics Journal C dergisinde (DOI: 10.11/epjc/s10052-019-6861-x) numarasıyla yayınlanmıştır.

ACKNOWLEDGMENTS

Above all, I am grateful to my supervisor Prof Dr. Eda EŞKUT who patiently support me during my studies. I would like to thank to her because of her comments about my studies and thesis. Also, I am happy that she is the one of my greatest supports in every aspect of this process.

I would like to sincerely thanks to my co-supervisors Assoc. Prof. Dr. Deniz SUNAR ÇERÇİ and Assoc. Prof. Dr. Salim ÇERÇİ who supported and helped me during my studies. Without their guidance and management, this work would not have been possible. Really I am very grateful them.

I would also like to take this opportunity to thank all the people of high energy physics in Çukurova University: Prof. Dr. Gülsen ÖNENGÜT, Prof. Dr. Ayşe POLATÖZ, Prof. Dr. Aysel KAYIŞ TOPAKSU, Prof. Dr. İsa DUMANOĞLU who knew how to train me and supervised me during Ph D. I also wish to thank the members of my thesis Jury who have accepted to evaluate my work with intelligence and kindness (Prof. Dr. Eda EŞKUT, Prof. Dr. Ayşe POLATÖZ, Prof. Dr. Aysel KAYIŞ TOPAKSU, Assoc.Prof. Dr. Salim Çerçi and Assist. Prof. Dr. İlknur HOŞ).

A big thanks to my friends for helps, fun times and chats during my studies Zühal Şeyma DEMİROĞLU, Kadri ÖZDEMİR, Aytül ADIGÜZEL, Emine GÜRPINAR, Yalçın GÜLER, Semiray GİRGİS.

It is also great pleasure for me to thank my family. Especially I would like to thank my elder sister Pınar ZORBİLMEZ who is biggest support in my life.

I would also like to thank to TAEK (project code: 2012K120260) who funded me during this thesis.

CONTENTS **PAGE**

ABSTRACT I
ÖZ II
GENİŞLETİLMİŞ ÖZET III
ACKNOWLEDGMENTS VII
CONTENTS VIII
LIST OF TABLES X
LIST OF FIGURES XII
ABBREVIATIONS XVIII
1. INTRODUCTION 1
2. THEORETICAL FRAMEWORK 5
2.1. The Standard Model of Particle Physics 5
2.2. Key Concepts of Quantum Chromodynamics 7
2.2.1. Asymptotic Freedom and Confinement 9
2.2.2. Running of Coupling Constant 10
2.2.3. Renormalisation 12
2.3. Description of Hadron-Hadron Collision 14
2.3.1. Deep Inelastic Scattering 15
2.3.2. Structure Functions 18
2.3.3. The Quark Parton Model 21
2.3.4. QCD Correction to QCD Parton Model 22
2.3.5. Parton Distribution Functions 25
2.4. Phenomenology of Underlying Event 26
2.4.1. Parton Showers 27
2.4.2. Hadronization and Fragmentation 28
2.4.3. Multiple Parton Interactions 30
2.5. Monte Carlo Event Generators and Tunes 30
2.5.1. PYTHIA 34

2.5.2. Cosmic Ray Event Generators 35
3. EXPERIMENTAL SETUP 37
3.1. The Large Hadron Collider 37
3.2. The CMS Experiment 39
3.2.1. The Coordinate System of CMS 41
3.2.2. Tracking System 43
3.2.3. Electromagnetic Calorimeter 45
3.2.4. Hadronic Calorimeter 46
3.2.5. Magnet 52
3.2.6. Muon System 53
3.2.7. Forward Detectors 55
3.3. Trigger System 57
3.4. Data Acquisition 59
4. MEASUREMENT OF ENERGY DENSITY 61
4.1. Physics Motivation 61
4.2. MC sets used in Analysis 62
4.3. Data and Event Selection Strategy 64
4.4. Calculation of Corrected Events, Noise and Pile up 69
4.5. The Effect of Magnetic Field 72
4.6. Data and MC comparison at the Detector Level 74
4.7. Correction from Detector Level to Particle Level 80
4.8. Systematic Uncertainty 83
4.9. Results 88
5. SUMMARY AND CONCLUSİONS 97
REFERENCES 99
CURRICULUM VITAE 103

LIST OF TABLES **PAGE**

Table 3.1. Particle accelerators and their basic parameters 37
Table 4.1. The MC Samples which were generated at B = 0 T (i.e., Magnet OFF) Used in The Present Analysis 63
Table 4.2. The MC Samples which were generated at B = 3.8 T (i.e., Magnet ON) Used in The Present Analysis 63
Table 4.3. Summary of runs at B = 0T and B = 3.8 T used in the analysis 64
Table 4.4. Summary of event selections used for the different event categories in data at detector level and in simulations at the stable-particle level.. 68
Table 4.5. Selection factor and purities for various event selection categories. The last two rows are derived using the formulae in the text. The porbability ϵ to select a single collision is determined from simulations, and the value quated here is the avarage value from al levent generators, with a maximal model dependence of 2%. The rightmost column quantifies the combined correction due to noise and pileup. All statistical uncertainties are negligible... 71
Table 4.6. The uncertainties in the energy density measurement for the three event selection categories. The results depend slightly on the pseudorapidity. 86

LIST OF FIGURES **PAGE**

Figure 2.1. A schematic view of SM of elementary particles 6
Figure 2.2. Q^2 dependence of α_s 9
Figure 2.3. Measurements of αs as a function of Q 11
Figure 2.4. Fundamental vertices in QCD, interacting particles including self-interaction of gluon 13
Figure 2.5. Components of hadron-hadron collision 14
Figure 2.6. Schematic diagram of DIS event 16
Figure 2.7. The Structure Function as a function of Q2 20
Figure 2.8. The structure of proton (Nathvani, 2017) 21
Figure 2.9. The radiative corrections to the QPM 23
Figure 2.10. The distributions of gluon (left), *u*-valance quark (middle) and *d*-valance quark (right) as a function of *F* at the scale Q^2 = 1.9 GeV^2 26
Figure 2.11. Hadronization process... 29
Figure 3.1. CERN Accelerator System 38
Figure 3.2. Compact Muon Solenoid (CMS) detector 40
Figure 3.3. Detection process of the CMS detector 41
Figure 3.4. A graphical representation of CMS coordinate system 42
Figure 3.5. CMS Coordinate System 43
Figure 3.6. A shematic view of CMS tracking system. Each detector module and back-to-back modules are represented by a line and double lines respectively 44
Figure 3.7. A geometric view of one quarter of the ECAL 45
Figure 3.8. Longitudinal view of the CMS detector... 47
Figure 3.9. The shematic view of the HB wedges 48
Figure 3.10. HO calorimeter and the position of the HO layer in the rings 49
Figure 3.11. The HE calorimeters mounted on the CMS detector 50

Figure 3.12. The cross sectional view of the HF. All dimensions are in mm 51
Figure 3.13. CMS Solenoid Magnets 53
Figure 3.14. CMS Muon System 54
Figure 3.15. The Forward detectors in CMS 55
Figure 3.16. Trigger System 57
Figure 3.17. Trigger Rate 58
Figure 4.1. Event selection strategies (a) INEL selection (b) NSD-Enhanced event selection (c) SD-Enhanced event selection 66
Figure 4.2. The number of the events distribution as a function of the tower energy. The left plot gives the smaller of the two HF calorimeter energies and the right plot gives the higher of the two HF calorimeter energies. The simulations are represented by lines the markers shows the data. The shaded areas correspond to measured detector noise. 67
Figure 4.3. Energy density distributions of Run 247324, has PU of 5% and Run 247920, has PU of 30% before (upper left) and after PU correction (upper right) with ratio of Run 247324 to Run 247920. Lower plots shows the energy density distribution before and after PU correction for Run 247324.............................. 72
Figure 4.4. Energy density distributions of the data and PYTHIA8 4C+MBR (upper left), EPOS-LHC (upper right) and QGSJETII.4 (bottom) MC samples for the cases of magnetic field on and off for CaloTower. The bottom panels of each plot represent the ratios energy density with magnet OFF to the energy density with magnet ON.. 74
Figure 4.5. Comparison of the calorimeter tower energy distribution for soft-INEL selection for data with simulations from MC event generators. All distributions are normalized total number of events per sample.. 76

Figure 4.6. Comparison of the calorimeter tower energy distribution for NSD-Enhanced selection for data with simulations from MC event generators. All distributions are normalized total number of events per sample 77
Figure 4.7. Comparison of the calorimeter tower energy distribution for SD-Enhanced selection for data with simulations from MC event generators. All distributions are normalized total number of events per sample. 78
Figure 4.8. Left: Comparison of the measured energy flow (uncorrected data for soft-INEL selection) with simulations from MC event generators (PYTHIA8 MONASH13 and 4C+MBR tunes, EPOS-LHC and QGSJETII.4) at the detector level. Right: The ratio of the uncorrected data to the MC predictions at the detector level. 79
Figure 4.9. Left: Comparison of the measured energy flow (uncorrected data for NSD-Enhanced selection) with simulations from MC event generators (PYTHIA8 MONASH13 and 4C+MBR tunes, EPOS-LHC and QGSJETII.4) at the detector level. Right: The ratio of the uncorrected data to the MC predictions at the detactor level. 79
Figure 4.10. Left: Comparison of the measured energy flow (uncorrected data for SD-Enhanced selection) with simulations from MC event generators (PYTHIA8 MONASH13 and 4C+MBR tunes, EPOS-LHC and QGSJETII.4) at the detector level. Right: The ratio of the uncorrected data to the MC predictions at the detector level 80
Figure 4.11. Left: Comparison of detector level (for soft-INEL selection) and particle level ($\xi > 10 - 6$) for different MC samples. Points show the detector level results while lines corresponds to predictions obtained from different MC samples. Right: Ratio of detector level to particle level i.e bin-by-bin correction factor. 82

Figure 4.12. Left: Comparison of detector level (for NSD-Enhanced selection) and particle level for different MC samples. Points show the detector level results while lines corresponds to predictions obtained from different MC samples. Right: Ratio of detector level to particle level i.e bin-by-bin correction factor 82
Figure 4.13. Left: Comparison of detector level (for SD-Enhanced selection) and particle level for different MC samples. Points show the detector level results while lines corresponds to predictions obtained from different MC samples. Right: Ratio of detector level to particle level i.e bin-by-bin correction factor. 83
Figure 4.14. Variation of results in data and MC due to variation of the cut applied for selection of events for soft-INEL 84
Figure 4.15. Variation of results in data and MC due to variation of the cut applied for selection of events for NSD-Enhanced events 85
Figure 4.16. Variation of results in data and MC due to variation of the cut applied for selection of events for SD-Enhanced events. 85
Figure 4.17. Variation of results in data and MC due to variation of the cut applied the energy scale uncertainty for soft-INEL selection. 87
Figure 4.18. Variation of results in data and MC due to variation of the cut applied the energy scale uncertainty for NSD-Enhanced selection 87
Figure 4.19. Variation of results in data and MC due to variation of the cut applied the energy scale uncertainty for SD-Enhanced selection 88
Figure 4.20. Comparisons of the data to PYTHIA8 CUETP8M1 tunes with and without MPI effect. Mass diffraction for each selection 89
Figure 4.21. Comparisons of the data to PYTHIA8 CUETP8M1 tunes with various values of P_{Tmin} for each selection. 90

Figure 4.22. Comparisons of the data to PYTHIA8 CUETP8M1 tunes with matter distribution for each selection. 91
Figure 4.23. Energy density measurement at stable-particle level for soft-INEL 92
Figure 4.24. Energy density measurement at stable-particle level for NSD-Enhanced.. 93
Figure 4.25. Energy density measurement at stable-particle level for SD-Enhanced.. 93
Figure 4.26. Energy density at stable-particle level for INEL selection compared to predictions from PYTHIA8 with tunes CUETP8M1, CUETP8M1+MBR and CUETP8S1. The gray band shows the total systamatic uncertainty. The band around PYTHIA8 CUSETS1 corresponds to the uncertainties of tune parameters. The right panel shows the ratio of model predictions to measured data.. 94
Figure 4.27. Energy density at stable-particle level for NSD-Enhanced selection compared to predictions from PYTHIA8 with tunes CUETP8M1, CUETP8M1+MBR and CUETP8S1. The gray band shows the total systamatic uncertainty. The band around PYTHIA8 CUSETS1 corresponds to the uncertainties of tune parameters. The right panel shows the ratio of model predictions to measured data.. 94
Figure 4.28. Energy density at stable-particle level for SD-Enhanced selection compared to predictions from PYTHIA8 with tunes CUETP8M1, CUETP8M1+MBR and CUETP8S1. The gray band shows the total systamatic uncertainty. The band around PYTHIA8 CUSETS1 corresponds to the uncertainties of tune parameters. The right panel shows the ratio of model predictions to measured data.. 95

Figure 4.29. A comparison of measurements of transverse energy density as a function of shifted pseudorapidity to different models and earlier published p-p data for several center-of-mass energies for NSD events.. 96

ABBREVIATIONS

ALICE	: A Large Ion Collider Experiment
ATLAS	: A Toroidal LHC Apparatus
BFKL	: Balitski-Fadin-Kuraev-Lipatov
CASTOR	: Centauro And Strange Object Research
CCFM	: Ciafaloni-Catani-Fiorani-Marchesini
CERN	: Conceil Europeenne pour la Recherche Nucleaire
CMS	: Compact Muon Solenoid
CSC	: Cathode Strip Chambers
DAQ	: Data Acqusition
DCS	: Data Control System
DGLAP	: Dokshitzer-Gribov-Lipatov-Altarelli-Parisi
DIS	: Deep Inelastic Scattering
DT	: Drift Tubes
ECAL	: Electromagnetic CALorimeter
FSR	: Final State Radiation
HB	: Barrel Hadronic Calorimeter
HCAL	: Hadronic CALorimeter
HF	: Hadronic Forward
HLT	: High Level Trigger
HO	: Outer Barrel Hadronic Calorimeter
INEL	: Inclusive Inelastic
ISR	: Initial State Radiation
LEP	: Large Electron Positron Collider
LHC	: Large Hadron Collider
LHCb	: Large Hadron Collider Beauty Experiment
LO	: Leading Order
MC	: Monte Carlo

MPI	: Multi Parton Interaction
NLO	: Next to Leading Order
NSD	: Non-Single-Diffractive
PDF	: Parton Density Function
PS	: Proton Synchrotron
RPCs	: Resistive Plate Chambers
QCD	: Quantum Chromodynamics
QED	: Quantum Electrodynamics
SD	: Single Diffractive
SLAC	: Standard Lineear Accelerator
SM	: Standard Model
SPS	: Super Proton Synchrotron
TEC	: Tracker End Cup
TIB	: Inner Barrel
TID	: Inner Disk
TOB	: Outer Barrel
UE	: Underlying Event
ZDC	: Zero Degree Calorimeter

1 INTRODUCTION

Particle physics, the branch of science, embodies the study of fundamental constituents of matter and interactions between them. It may be said that particle physics have begun with the discovery of the electron structureless point particles by J. J. Thomson in the late 19th century. In following years, a lot of new particles was discovered using the cosmic rays and accelerators which have high energy. Under the guidance of all these discoveries and developments, a model called "Standard Model (SM)" was proposed by scientists in order to find some answers for some questions (How are discovered particles categorised? How do they interact with each other?). The SM is a very successful theory to explain the fundamental parts of matter and their interaction between each other because the SM has been tested by scientists for years using cosmic rays, many accelerators and particle detectors. According to the SM model the known all matter around us made of the fermions which have spin 1/2 particles. There are two basic types of fermions: quarks and leptons. Each group consists of six elementary particles. And also, there are four fundamental forces in nature: the weak force, the electromagnetic force, the strong force and the gravitational force. Each of them has its own corresponding bosons: gluon, photon and $W^{\pm}$, Z^0 bosons. The SM model explains well the behaviours three (the weak force, the electromagnetic force and the strong force) of these forces on all of the matter particles. However, the gravity has not been explained in SM. Even though the SM model has the best description to explain the fundamental particles and their interaction between them it doesn't have all answers about universe such as "What is the dark matter?" or "what happened to the antimatter after big bang?" and doesn't show full picture (Perkins, 2000).

In the late of 1960s, Feynman and Bjorken proposed a model called "Parton Model" which suppose that proton consists of a bound state of partons named fermions (quarks and gluons). The quarks in SM are elementary particles and the first clear evidence for them have been found in deep inelastic scattering (DIS) experiment at the Standard Linear Accelerator Center (SLAC) in early 1970s. DIS is the experiment that has played a fundamental role in the exploration of the structure of the nucleon. The first DIS experiment were carried out on protons by using electron beams. After the first DIS experiment many physicists, theorists and experimenters have embarked on a long-series of so-called inelastic diffusion experiment. The quarks in the proton are strongly interacting fundamental particles and these strong interactions are defined by using a main theory so-called Quantum chromodynamics (QCD) (Thomson, 2013).

The QCD is constructed with the formalism of quantum field theory. It is also gauge theory based on symmetry group SU(3) which involves eight vector bosons. Like photon participating in electromagnetic interactions in quantum electrodynamics (QED), the mediating particles, gluons, massless spin-1 boson, participate in strong interactions by exchanging particles in QCD. Despite the fact that there is just a single sort of photon mediating electromagnetic interactions there are eight kinds of gluons mediating strong interactions. There are three sort of colour charges in QCD: red (*r*), green (*g*) and blue (*b*). Each quark carries a colour and their assemblage in a hadron forms neutral hadrons. While quarks, the fundamental objects participating in strong interactions, have three essential colour-charge states *(r, g and b)* gluons exchanging boson between quarks have two basic colour-charge states (colour-anticolour) (Ellis, 2003).

Colliding the hadrons in high-energy level using the Large Hadron Collider (LHC) is important to understand the basic structure of the universe and matter. A hadron-hadron collision is dominated by soft interaction which is far from being understood in all its aspects. The hadronic activity in the detector is complicated hence it can be separated in two subsets in event. One of them is the hard part of the hadron-hadron collisions and it corresponds to the activity relating to the hard component and contains only the large transverse momentum jets and other objects carrying a hard scale. The other is called underlying event which contains the rest of the hadronic activity. In general, the underlying event is characterized by processes involving partons not directly involved in the hard process. The underlying activity is important to correctly identify background noise contaminating our main process and so it needs to be well modelled. Our analysis, the measurement of the energy density as function of pseudorapidity in proton-proton (p-p) collision at 13 TeV has a significant sensitivity to the underlying events. And also, the results of the measurement of the energy density provide valuable input for tuning of Monte Carlo (MC) models which is used to describe a hadronic activity.

In order to be able to compare the experimental data with theoretical predictions, the simulation of interactions is produced by using MC event generators which is an important tool for every physics analysis. The MC in a physics analysis are used in various steps from estimation of background to obtain the final results. Indeed, a better understanding of the physics analysis is provided by adding detector effect to MC samples obtained from theoretical approaches (Driesch, 2016). In this analysis, various MC event generators was used to correct the real data obtained from the CMS detector. These event generators are PYTHIA 8 (version 8.212) with different tunes (tune MONASH2013, CUETP8M1, CUETP8S1 and MBR), EPOS (version 1.99) and QGSJETII.4.

In chapter 3, the information about experimental setup used in this analysis is presented. The LHC designed to reach a luminosity of 10^{34} $cm^{-2}s^{-1}$ at the CERN (Conseil Europeén pour la Recherche Nucléaire), the most powerful circular particle accelerator in the world, offer a unique opportunity to test the SM. In fact, its main goal is the search for physics beyond the SM and to find the origin of elementary particle masses by using high center-of-mass-energies. Four detectors are installed on the LHC accelerators around the collision point. These detectors are CMS (Compact Muon Solenoid), ATLAS (A Toroidal LHC Apparatus), ALICE (A Large Ion Collider Experiment) and LHCb (Large Hadron Collider

Beauty). CMS and ATLAS was designed to search the general physics subjects while LHCb, located at interaction point 8 of the LHC, was built to probe the B physics. On the other hand, ALICE is focused to heavy ion collisions. ALICE located at interaction point 2 of the LHC.

The data used in this thesis is obtained by CMS detector. It is situated the interaction point 5 around the LHC ring at Cessy in France (Chatrchyan S.,et al., 2008). The CMS is composed of several subdetectors and one solenoid magnet that delivers a magnetic field of 3.8 T. These subdetectors work together in an integrative manner and allow the direct detection of most particles of the SM except neutrinos. The CMS detector is essentially separated into a silicon tracker system, an electromagnetic calorimeter, a hadronic calorimeter and muon system. In this thesis, detailed information about CMS and its subdetectors is given in Chapter 3.

Finally, the last chapter of this analysis, Chapter 4 presents the different stages of the measurement of the energy and transverse energy density analysis. In this section, the energy density as well as transverse energy density as a function of pseudorapidity which covers $3.15 < |\eta| < 5.2$ (Hadronic Forward-HF) and $-6.6 < \eta < -5.2$ (CASTOR) are present with the data which have been collected by the CMS at low luminosity in 2015. Moreover, in this chapter, it can be found that the definition of the selection of events, estimations of background, the study on the systematic errors and the application on the real data.

The results and details of the analysis presented in this thesis are given in the CMS Analysis Note (Cerci, Sunar Cerci, Zorbilmez et al., 2015), CMS Physics Analysis Summary (Sirunyan, 2016) and analysis has been published CMS Collaboration International the European Physics Journal C (EPJ-C) (DOI: 10.11/epjc/s10052-019-6861-x) (CMS Collaboration, 2019). It has also presented by the author in "1st National Workshop on CERN Activities" (Zorbilmez, 2018).

2 THEORETICAL FRAMEWORK

The fundamental constituents of matter and interactions between them is very important to understand the Universe we are in. The purpose of this section is to provide information about the elementary particles and some theoretical ideas.

2.1 The Standard Model of Particle Physics

The Standard Model (SM) formulated in the 1970s helps to explain and understand the fundamental components of matter and interaction between them. The SM describes quite successfully nearly all known particle physics process. The particle content of SM is shown in Figure 2.1. According to the SM, all matter is described by spin 1/2 particles called fermions. There are two types fermions as quark and leptons. Both of them are present in three generations. All visible matter can be explained the first-generation particles (*u, d, e* and ν_e). The first-generation particles are the stable particles but the second and third generation particles except muon neutrino (ν_μ) and tau neutrino (ν_τ) are unstable particles (Perkins, 2000).

Except for gravity, the SM model describes the interaction between the fundamental components of matter. These interactions are strong, electromagnetic and weak interactions. The interactions between fermions are mediated by gauge vector bosons. In SM, there are four types gauge vector boson namely photon (γ), gluon *(g), Z* and $W^{\pm}$ bosons. The gauge vector bosons are shown in Figure 2.1. Fundamentally and vigorously, there are three type interactions. The strong interaction in the SM is described in the QCD as responsible for bind the quark in the hadrons. The gluon is force-carrying particle for strong interaction. The electromagnetic interactions described in the Quantum Electrodynamics (QED) are responsible for the interaction between two particles having electric charge. The force-carrying particle of electromagnetic interactions is the massless photon (γ). The weak interaction responsible for the radioactive decay of subatomic particles, also have three gauge bosons. The one of them with neutral charge is *Z* bosons *(Z^0)*, other two of them with positive and negative charge are respectively W^+ and W^- bosons.

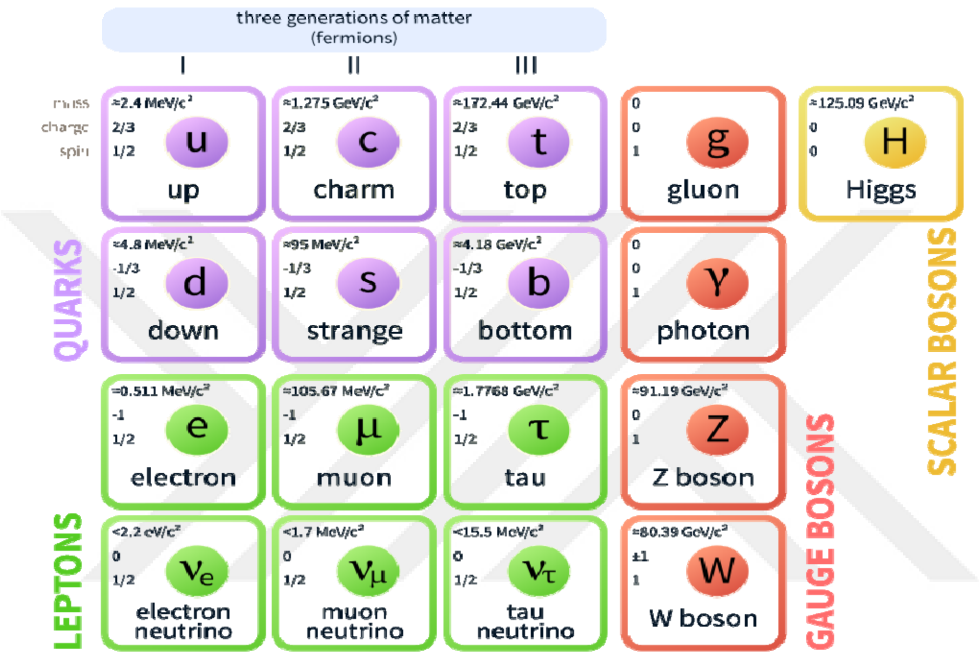

Figure 2.1. A schematic view of SM of elementary particles (Amoroso, 2015)

The SM contains six leptons as elementary particles. Leptons can be observed as free particles. Electrically charged three leptons, electron *(e),* muon (μ) and tau (τ) have a negative charge. Each of them has an electrically neutral counterpart, called the neutrino as known neutral leptons. These are electron neutrino (ν_e), muon neutrino (ν_μ) and tau neutrino (ν_τ) (Robson, 2017).

Within SM, quarks are a part of fermions. There are six flavours of quarks which carry fractional electrical charge of +2/3|e| or -1/3|e|. These are up-quark *(u),* down-quark *(d),* charm-quark *(c),* strange-quark *(s),* top-quark *(t)* and bottom-quark *(b). The u*-quark and *d*-quark in the first generation is the set of lightest particles (Robson, 2017). The second generation with *c*-quark and *s*-quark are heavier from the first generation. Third generation consist of the heaviest particles. Unlike leptons, there is an extra degree of freedom for the quarks, called *colour*. Each flavour of quark is represented through three different colours: red (*r*), green (*g*) and blue (*b*) and corresponding anti-colour ($\overline{r}, \overline{g}$ and $\overline{b}$). Because of this extra property, quarks cannot be observed as free particles but can only exist in bound states. There are two types of bound state of quarks. One of them consist out of three quarks (anti-quarks) (qqq), called *baryons*, the other contains a quark and anti-quark combination, called *mesons* ($q\overline{q}$) (Hos, 2016).

2.2 Key Concepts of Quantum Chromodynamics

QCD is a non-abelian gauge theory to describe the strong interactions which is the one of the four fundamental forces of nature in SM. It based on the formalism of the field theory, local invariant under symmetry of the colour SU(3). Making the invariant theory under the SU(3) group equates to the conservation of an additional quantum number which is colour charge. In order to describe the interaction between quarks and gluons, it is necessary to build the Lagrangian of QCD which can be express according to equation 2.1.

$$\mathcal{L} = -\frac{1}{4} F^{A}_{\alpha\beta} F^{\alpha\beta}_{A} + \sum_{flavors} \overline{q_a} \left(i\gamma_\mu D^\mu - m \right)_{ab} q_b \qquad (2.1.)$$

where α, β and γ represent Lorentz indices while the sum in equation 2.1 is made over the different flavours of quark. The field strength tensor is denoted by $F^{A}_{\alpha\beta}$ and it is derived from the gluon field $\mathcal{A}^{A}_{\alpha}$. The field strength tensor can be expressed according to equation 2.2. (Ellis, 2003).

$$F^{A}_{\alpha\beta} = \left[\partial_{\alpha}\mathcal{A}^{A}_{\beta}\text{-}\partial_{\beta}\mathcal{A}^{A}_{\alpha}\text{-}g_{s}f^{ABC}\mathcal{A}^{B}_{\alpha}\mathcal{A}^{C}_{\beta}\right] \qquad (2.2.)$$

The capital indices A, B and C are related with the eight degrees of freedom for the field of the gluon. The third term in equation 2.2 corresponds to the self-interaction of the gluons. The terms f^{ABC} are called the structure constant of the SU(3) group in the above expression.

The symmetry plays a basic role in theoretical treatments of QCD. Gluons, the spin-1 gauge boson in QCD, have no electric charge but they have two colour charges (colour and anti-colour). Also, as mentioned before, each quark has a colour charges among the three existing ones. There are three different colour states as red *(r),* blue *(b)* and green *(g)*. The colour charges are shown a column vector with three components called vector c:

$$= \begin{pmatrix}1\\0\\0\end{pmatrix} \text{ for red,} \quad \begin{pmatrix}0\\1\\0\end{pmatrix} \text{ for blue,} \quad \begin{pmatrix}0\\0\\1\end{pmatrix} \text{ for green} \qquad (2.3.)$$

There are nine different states for gluon because of combination of colour-anticolour of gluons. These nine states comprise of a "*colour octet*":

$$\left\{\begin{array}{ll} |1> = (r\bar{b} + b\bar{r})/\sqrt{2} & |5> = -i(r\bar{g}\text{-}g\bar{r})/\sqrt{2} \\ |2> = -i(r\bar{b}\text{-}b\bar{r})/\sqrt{2} & |6> = (b\bar{g} + g\bar{b})/\sqrt{2} \\ |3> = (r\bar{r}\text{-}b\bar{b})/\sqrt{2} & |7> = -i(b\bar{g}\text{-}g\bar{b})/\sqrt{2} \\ |4> = (r\bar{g} + g\bar{r})/\sqrt{2} & |8> = (r\bar{r} + b\bar{b}\text{-}2g\bar{g})/\sqrt{6} \end{array}\right\} \qquad (2.4.)$$

And "*colour singlet*":

$$|9> = (r\bar{r} + b\bar{b} + g\bar{g})/\sqrt{3} \qquad (2.5.)$$

The neutral colour, called white, is formed by the combination of the three colours (anti-colours) or a pair of the same colour – anticolour (Hos, 2016).

2.2.1 Asymptotic Freedom and Confinement

A particular element of QCD is the fact that there are two effects for quarks according to the coupling constant of strong interactions. One of them is asymptotic freedom the other is the confinement of colour.

Quarks cannot be remained alone under the normal conditions. They are always in bounded state with other quarks or antiquarks to form hadrons because the energy in the gluon field creates another quark pair when a quark separates from other quarks. However, the condition in which the coupling constant of strong interactions is weak causes the essence of *asymptotic freedom*. The *asymptotic freedom* express that quarks and gluons can behave as quasi-free particles at the short enough distances (Hos, 2016).

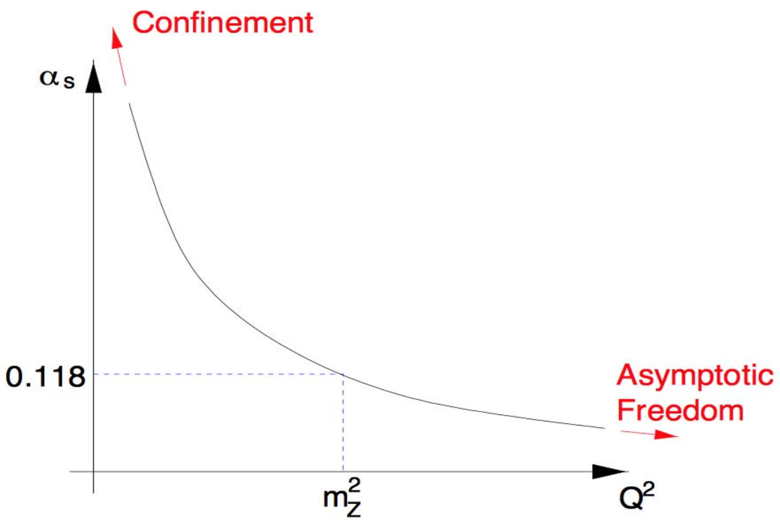

Figure 2.2. Q^2 dependence of α_s (Lambacher, 2007)

One of the properties of strong interaction are the fact that the phenomenon of *confinement*. This means that if the distance between two quarks is large, the coupling constant of relevant interaction becomes very large. Hence quark produced after interaction cannot isolate as free particles and the bound state between two coloured quarks become much stronger. The phenomenon of confinement makes it possible to understand why quarks cannot be observed alone. As shown in Figure 2.2, the confinement become much stronger in the low Q^2 scale and large α_s values (Muta, 2009).

2.2.2 Running of Coupling Constant

The coupling constant obtained from experiments for electromagnetic interactions according to QED theory can be written as:

$$\alpha_{em} = \frac{e^2}{4\pi} \cong \frac{1}{137} \tag{2.6.}$$

Similarly, the strong interactions according to QCD theory have the running coupling constant which is denoted by α_s. The coupling constant for both electromagnetic interactions and strong interactions is the variable to account for the intensity of the interaction and depend on the energy scale of interaction considered. In terms of QCD, the calculation of the coupling constant α_s is controlled by the β function which is obtained from the expression that physical observable cannot depend on renormalization scale (μ_r) (See section 2.2.3). As a result, the coupling constant for strong interactions can be written as (Ellis, 2003) (Muta, 2009).

$$\alpha_s\left(\mu^2\right) = \frac{4\pi}{\beta_0 \log\left(\mu^2 / \Lambda_{QCD}^2\right)} \tag{2.7.}$$

where the Λ_{QCD} is known as QCD-scale and it is a constant (~217 MeV). The energy scale is symbolized by μ. β_0 is a coefficient which depends on the number of active quark flavours (n_f). The β_0 can be written as:

$$\beta_0 = 11 - \frac{2}{3} n_f \qquad (2.8.)$$

The experimental studies for the running coupling constant of QCD is shown in Figure 2.3. The *x* axis of this figure represent to the energy scale while the *y* axis corresponds to the strong coupling constant.

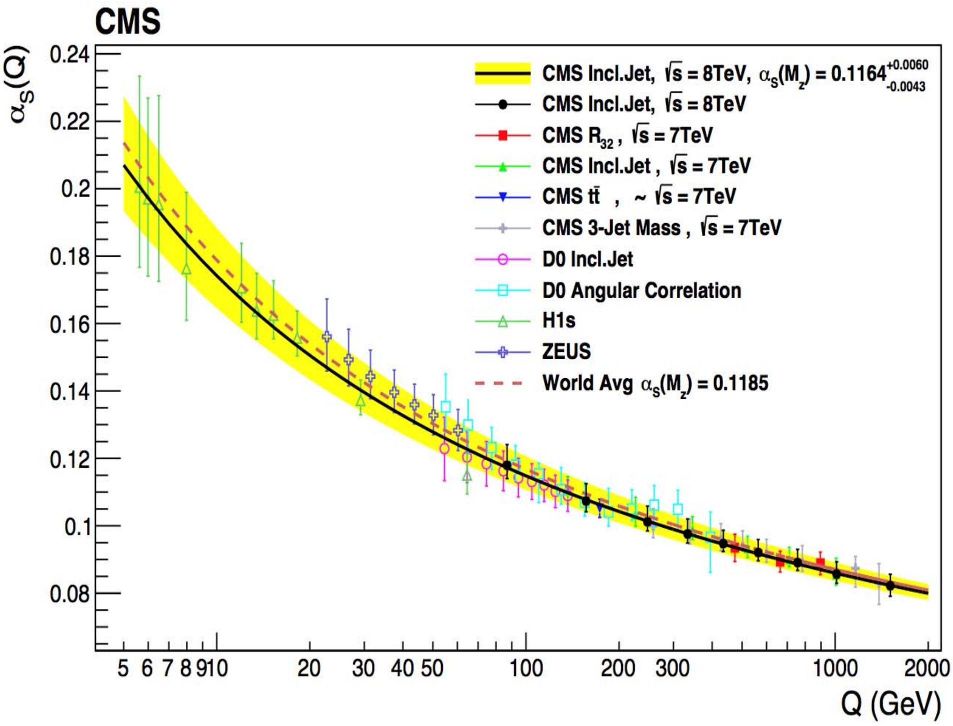

Figure 2.3. Measurements of α_s as a function of Q (CMS collaboration, 2017b)

2.2.3 Renormalisation

The Feynman diagrams consist of points; called vertices, help to understand the interactions described by QCD. The Figure 2.4 shows fundamental vertices in QCD. These interactions can be shown using the simple Feynman diagrams. Diagrams, which contain the fewest number of vertices for an interaction, are named Leading Order (LO) diagrams, while diagrams at the next (higher) order are called Next-to-Leading-Order (NLO). Such diagrams may also contain closed loops, which have important consequences such as leading to divergences appearing in high order calculations. A method called *renormalisation* is used to get rid of these divergences. The renormalisation method makes it possible to overcome these divergences by introducing a second energy scale μ_r^2, which is the point at which the subtraction that removes divergences is performed (Sen, 2011) (Sunar, 2009).

Discrepancies in higher order calculation can be solved by defining the effective coupling constant α_s, which has a dependence of μ_r^2. Any physical observable named as *R* for all orders of α_s must not be dependent on the choice for μ_r^2. The dependence of R on μ_r^2 can be solved by using the dependence of α_s on μ_r^2. By using the renormalization group equation, the dependence of α_s on μ_r^2 can be calculated. The renormalization group equation can be written as:

$$\mu_r^2 \frac{dR}{d\mu_r^2} = \left(\mu_r^2 \frac{\partial}{\partial \mu_r^2} + \mu_r^2 \frac{\partial \alpha_s}{\partial \mu_r^2} \frac{\partial}{\partial \alpha_s}\right) R = 0 \qquad (2.9.)$$

The partial derivative $\partial\alpha_s/\partial\mu_r^2$ corresponds to the dependence of α_s on μ_r^2.

$$Q^2 \frac{\partial \alpha_s}{\partial Q^2} = \beta(\alpha_s) = -\alpha_s \sum_{n=0}^{\infty} \beta_n \left(\frac{\alpha_s}{4\pi}\right)^{n+1} = -\frac{\beta_0}{4\pi}\alpha_s^2(Q^2) - \frac{\beta_1}{16\pi^2}\alpha_s^3 + O(\quad (2.10.)$$

where the coefficients β_0 and β_1 are determined by the number of active quarks flavours which is denoted by n_f.

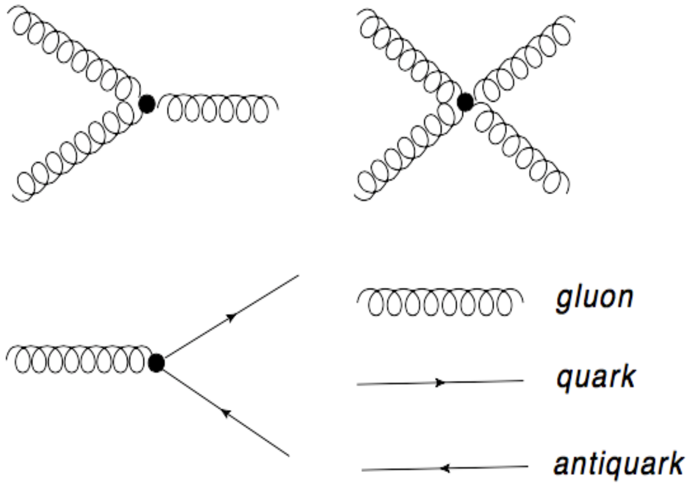

Figure 2.4. Fundamental vertices in QCD, interacting particles including self-interaction of gluon (Sen, 2011)

As a result, the strong coupling constant is reorganized for one loop approximation and it can be written as in equation 2.5. The QCD-scale Λ_{QCD} in equation 2.5 cannot be calculated by using the theory. According to experimental results if the μ_r^2 increases than the value of the α_s decreases. The perturbative QCD does not work under condition which is $\mu_r^2 \rightarrow \Lambda_{QCD}^2$. Therefore, Λ_{QCD}^2 plays a role such as boundary energy scale between perturbative and non-perturbative QCD (Sunar, 2009).

2.3 Description of Hadron-Hadron Collision

Hadron colliders are important to search for production of new particles at high-energy level. They can be either p-p or p-p̄. The most natural way to interact hadrons with each other is to use the beams of particles. Hence the colliding hadrons are complicated process due to the fact that the colliding hadrons are composite objects. The interaction of hadrons means that the interaction of quarks and gluons with each other. During the collision of two hadrons; just as one *parton* of incoming hadrons can participate in interaction, the probability of the participation of other *partons* into interaction cannot be ignored. This makes the hadron collision more complicated. The complexity of a hadronic collision can be represented by distinguishing two different states; the Hard Scattering, hardest part of collision and the Underlying Event (UE), whole remaining part of the hadronic collision. Figure 2.5 shows interactions at these separate states (Sen, 2011).

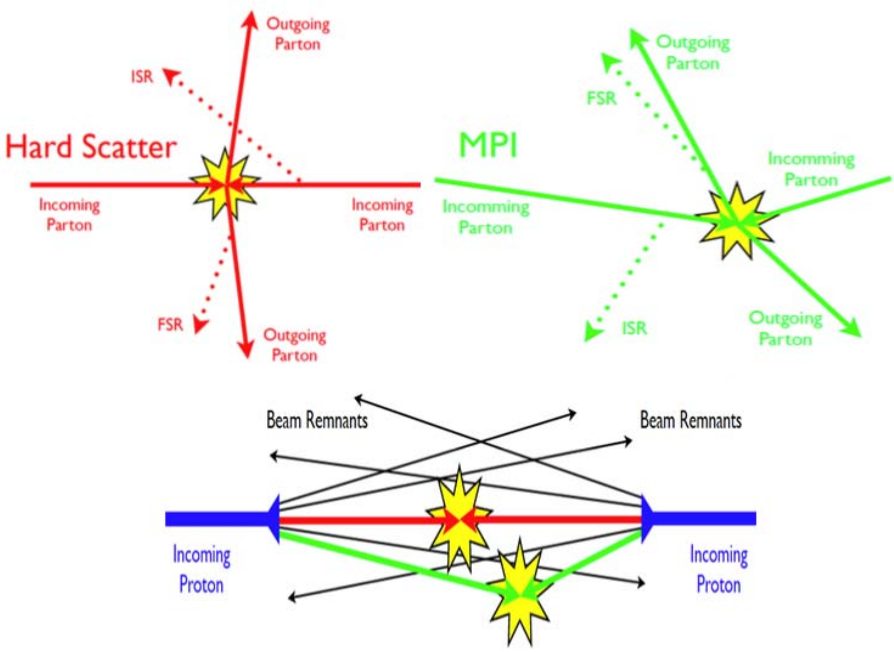

Figure 2.5. Components of hadron-hadron collision (Sen, 2011)

Hard scattering is defined as the strongest interaction in hadron-hadron collision hence it is known main part of an interaction. Moreover, hard scattering processes are described as short-range processes and can be calculated correctly within perturbative QCD (pQCD). These processes with the interaction of high-energy *partons* are defined by a high Q^2 due to the small strong coupling constant α_S. But soft processes cannot be calculated by means of perturbation theory since the coupling constant is too high. Therefore, non-perturbative calculations are needed.

The event kinematics of hadron-hadron collision are described by three variables which are the momentum fractions of two interacting partons (x_1, x_2) and Q. These kinematics variables are three experimentally well-measured quantities. In hadron-hadron collision at high energy, most of interactions are only soft interactions of the constituent quarks and gluons. The momentum transfer of such interactions is small hence pQCD cannot be used. However, if the momentum transfer is large in an interaction (hard interaction) in that case both perturbative and non-perturbative calculations are used (Thomson, 2013) (Ellis, 2003).

2.3.1 Deep Inelastic Scattering

The determination of the structure of the hadrons have been made by the experiments of Deep Inelastic Scattering (DIS), which has played a fundamental role in the exploration of the interior of the nuclei. The first inelastic scattering experiments were made in which, the Standard Linear Accelerator Centre (SLAC) in 1967. The electrons were selected as the projectiles while the protons were selected as the targets. The electron beam of up to 21 GeV was directed on liquefied hydrogen a target of protons. In this type of experiment, the angular and energetic distribution of the diffuse electron is only measured. Indeed, The DIS process is an extension of Rutherford scattering which revealed the structure of the atom at the beginning of the 20th century (Thomson, 2013). Also, it provides better resolution than the previous studies such as Rutherford scattering. Figure 2.6 shows a schematic diagram for first DIS event. DIS is the reaction that is given by the process.

$$e^- + p \rightarrow e^- + X$$

where the final state particle is represented by X and e^- corresponds to the scattered

leptons from the proton. The DIS process in the top is inelastic because of that the initial kinetic energy of the projectile, and target is nor conserved. The part of it is transferred to other processes. Moreover, this scattering is called inclusive because X is not determined by the experiment and one is only interested in the electron diffused in the final state (Ebert, 1995).

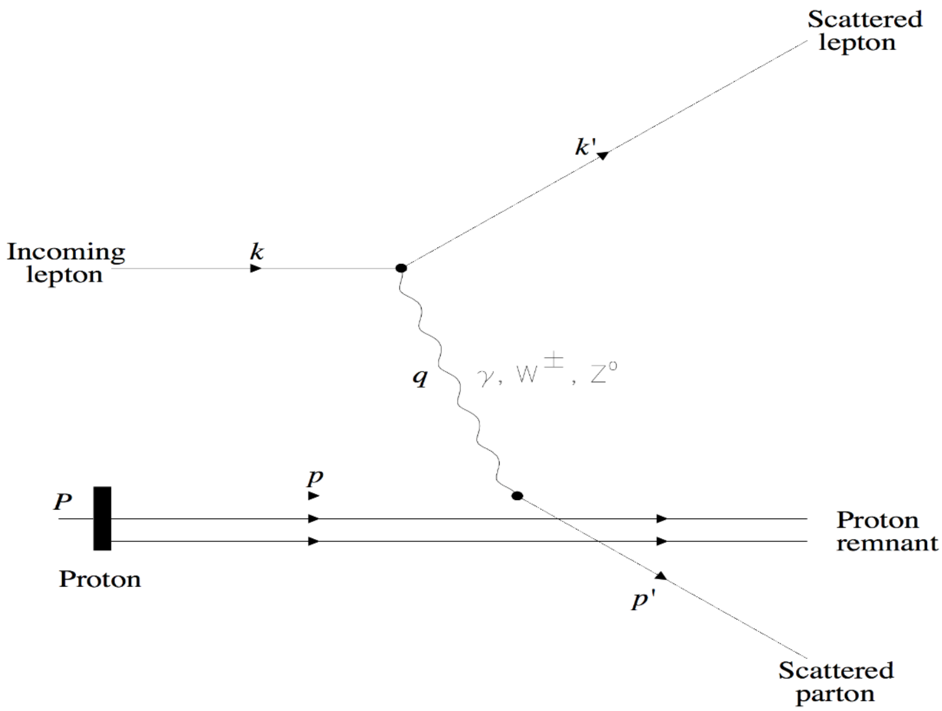

Figure 2.6. Schematic diagram of DIS event (Ebert, 1995)

In order to probe the structure of proton in Figure 2.6, an energetic lepton is sent to interact with a *parton* in the proton. k and k' demonstrate the incoming and scattered leptons, respectively. Also, k and k' represent four-momentum for lepton then momentum transfer between the incoming lepton and the *parton* of the proton is:

$$q = k\text{-}k' \tag{2.11.}$$

The Lorentz invariant quantities x, Q^2, y and W are usually used to define the kinematics of a DIS event. Q^2 which defines resolving power of the probe, is the negative square of the four-momentum transfer:

$$Q^2 = \text{-}q^2 = \text{-}(k\text{-}k')^2 = \left(k^2\text{-}k'^2 + 2k.k'\right)$$

$$Q^2 = 4k\,k' sin^2(\theta/2) \tag{2.12.}$$

where θ is the angle between two vectors k and k'. The Lorenz invariant variable, x is known as Bjorken scaling variable and is a fraction of the proton's momentum carried by the interacting parton:

$$x \ = \frac{Q^2}{2P.q} \tag{2.11.}$$

P in the formula shows the four-momentum of incident proton. In the DIS process, $Q^2 \gg m_p^2$ (deep) and $W^2 \gg m_p^2$ (inelastic), it is assumed that the incident proton has an infinite momentum frame. Therefore, in this frame, all the masses of the *partons* and proton can be neglected. The variable y represents the fractional energy loss of the lepton:

$$y = \frac{P \cdot q}{P \cdot k} \tag{2.12.}$$

The range of the variables x and y lie between 0 and 1 ($0 \leq x, y \leq 1$). Finally, the variable W represents the invariant mass of hadronic final state:

$$W^2 = (q + P)^2 = q^2 + P^2 + 2q.P \tag{2.13.}$$

The kinematic regime of the inelastic scattering processes is experimentally separated in two states. One of them is called *Photon production* state where Q^2 takes approximately zero value ($Q^2 \approx 0$) and quasi-real photon is used as exchanged boson. The other is the state where Q^2 is greater (or equal) 1 GeV ($Q^2 \geq 1$ GeV) and virtual photon is used as exchanged boson (Sunar, 2009).

2.3.2 Structure Functions

The studies of the DIS experiment has improved the understanding of the proton structure. Moreover, the probing of the structure of the proton and the discussing the basic interaction of quarks, gluons and leptons provides to understand the actual frame of a hadronic collision. The differential cross section for DIS process is written as (Connor, 2014).

$$\frac{d^2\sigma}{dxdQ^2} = \frac{4\pi\alpha^2}{xQ^4}\left[xy^2F_1(x, Q^2) + (1 - y)F_2(x, Q^2)\right] \tag{2.14.}$$

where the quantities $F_1(x,Q^2)$ and $F_2(x,Q^2)$ are called the Structure Functions (SF) which contain all information relating to the dynamics of the hadronic part of the diffusion process. The structure functions in DIS process, *$F_1(x)$* and *$F_2(x)$,* can be written using $f_i(x)$.

$$F_2(x) = \sum_i e_i^2 f_i(x)x \tag{2.15.}$$

$$F_1(x) = \frac{1}{2x}F_2(x) \tag{2.16.}$$

where e_i^2 shows the charge of *parton i.* The equation (2.13) is known as the *Callan-Gross* relation, if any structure function in equation 2.13 is known other structure function can be calculated by using related equation (Callan-Gross relation). (Martin, 2006).

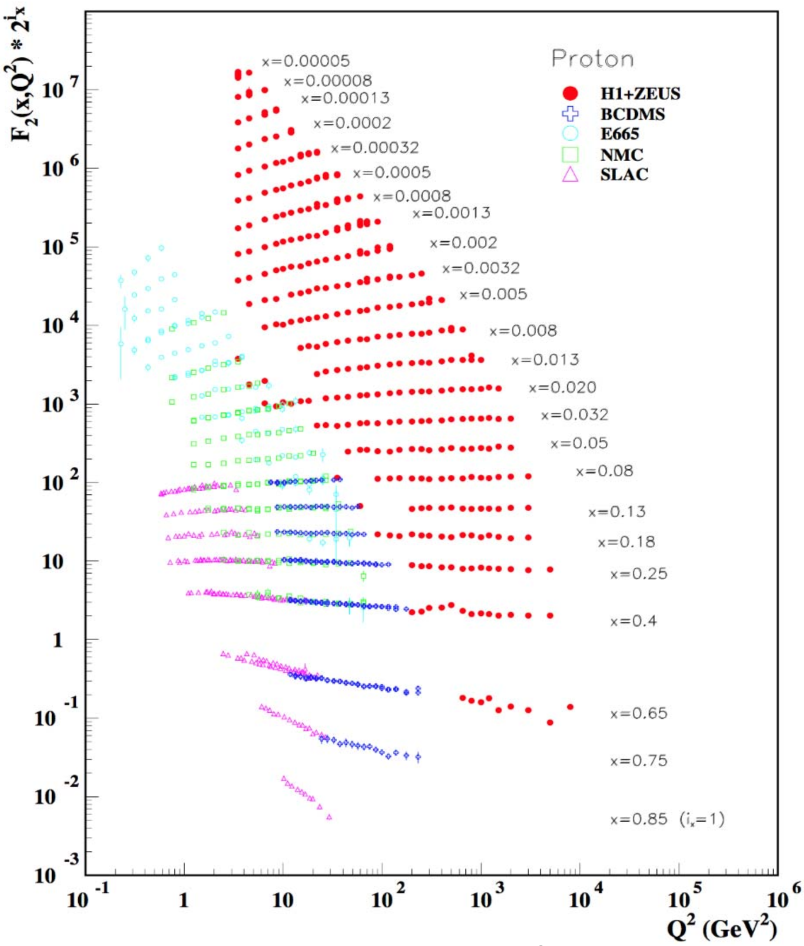

Figure 2.7. The Structure Function as a function of Q^2 (Olive, 2014)

Moreover, an instantaneous distribution of partons is determined by named parton distribution functions $f_i(x)$. They give a probability that *parton i* carries a fraction *x* of momentum of the hadron. The total hadron's momentum includes the sum of all fraction.

$$\sum_i \int_0^1 x f_i(x) dx = 1 \tag{2.17.}$$

The experimental data showing the structure function as a function of Q^2 for fixed values of x are given in Figure 2.7 (Ledwig, 2017).

2.3.3 The Quark Parton Model

p-p collisions examined at LHC are important in order to understand the influence of the strong interactions. Therefore, firstly, the structure of the proton must be well defined. Feynman proposed that proton composed of *partons* which are point-like constituents; quarks and gluons. Proton consist of two kind of quarks; called "valans quarks" (u,u,d), which regulate the macroscopic quantities of proton (like spin, charge, etc.), are "sea quarks" ($u_s\bar{u}_s, d_s\bar{d}_s, s_s\bar{s}_s$), which are virtual quark-antiquark pairs which from upon the splitting of a gluon within the hadron. All quark flavours are in the sea inside the proton with mass $m_q \ll Q$ at scale Q. m_q corresponds to the mass of the quarks. The illustration of the parton structure is shown in Figure 2.8.

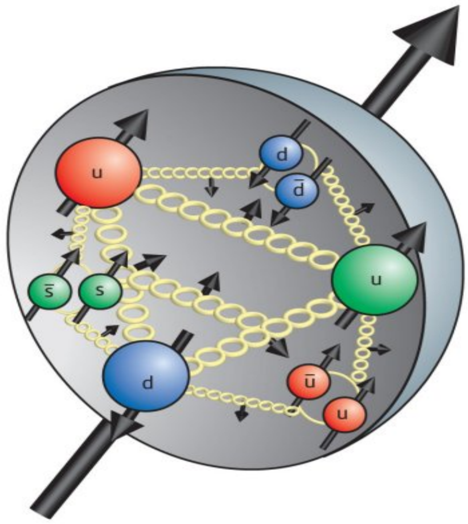

Figure 2.8. The structure of proton (Nathvani, 2017)

In parallel with the developments that took place during the DIS studies, a model was proposed by Feynman. As known Quark Parton Model (QPM), a general model describes the structure of hadrons. According to this model, hadrons consist of *partons* that spin ½ particles. Actually, QPM gives three basic assumptions which are:

- The transversal momentum of partons is smaller than its longitudinal momentum so the intrinsic transversal momentum of partons is neglected.
- The parton is massless
- Also, it assumes that the partons act as free particles during the interaction.

The actual interaction in the hard-scattering process take place between *partons*. As mention before, the dimensionless structure functions $F(x, Q^2)$ which parameterizes the hadron structure during the hadronic collisions are used to describe the process. It is necessary in this case to distribute the total momentum of the hadron between its constituents. A function called Parton Distribution Function (PDF) is used in order to distribute the total momentum of the hadron. PDF defines the behaviours of the *parton* in the hadrons (Gunnellini, 2014).

2.3.4 QCD Correction to QCD Parton Model

As previously mentioned in section 2.2.3, Feynman diagrams help us to understand how processes are performed by QCD. Figure 2.9 shows some Feynman diagrams which define the LO radiative corrections to the QPM. There are some processes to describe the interactions of parton in hadron. The probability to measure a quark in a quark can be named QCD Compton process (QCDC), while the probability to measure a quark in a gluon can be named Boson Gluon Fusion (BGF) process. The other processes are the probability to measure a gluon in a quark and finally the probability to measure a gluon in a gluon (Klundert, 2018).

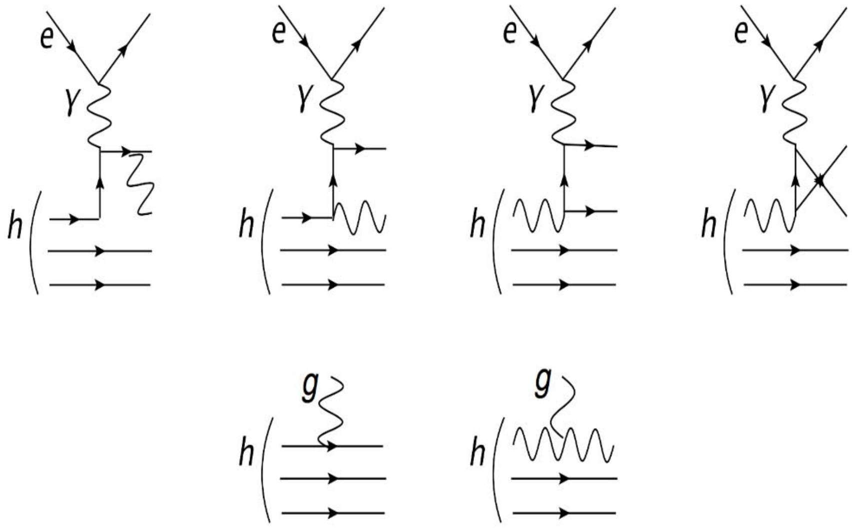

Figure 2.9. The radiative corrections to the QPM (Klundert, 2018)

The upper diagrams in Figure 2.9 cause *e-p* (Klundert, 2018) scattering in LO because a gluon does not directly connect to leptons. The lower diagrams in Figure 2.9 provide a direct contribution in hadron-hadron interaction. The upper left two diagrams correspond to QCDC process while the upper right two diagrams correspond to BGF process. The contribution of measuring a gluon in a quark is represented by the lower left diagram. Finally, the contribution of measuring a gluon in a gluon is denoted by lower right diagram.

Considering the QPM, the cross section of QCDC process can be written as:

$$\frac{d\sigma^{QCDC}}{dk_T^2} = \sigma_0 e_q^2 \frac{\alpha_s}{2\pi} \frac{1}{k_T^2} P_{qq}(z) \tag{2.13.}$$

where k_T^2 represents transversal momentum and $P_{qq}(z)$ is the splitting function. The total cross section can be calculated by integrating over k_T. For $k_T = 0$, a collinear divergence is observed and this can be exceeded by putting the lower cut-off at $k_{T,0}^2$.

$$\sigma^{QCDC} = \sigma_0 e_q^2 \frac{\alpha_s}{2\pi} P_{qq}(z) \left(\ln\left(Q^2 / k_{T,0}^2 \right) + \cdots \right) \qquad (2.14.)$$

Similarly, the equation of total cross section can be improved by adding relevant quark PDF and splitting function. For these processes, the four splitting functions can be given by (Klundert, 2018);

$$P_{qq}(z) = \frac{4}{3}\left(\frac{1+z^2}{1-z}\right) \qquad (2.15.)$$

$$P_{qg}(z) = \frac{4}{3}\left(\frac{1+(1-z)^2}{z}\right) \qquad (2.16.)$$

$$P_{gq}(z) = \frac{1}{2}\left(z^2 + (1-z)^2\right) \qquad (2.17.)$$

$$P_{gg}(z) = 6\left(\frac{z}{1-z} + \frac{1-z}{z} + z(1-z)\right) \qquad (2.18.)$$

2.3.5 Parton Distribution Functions

In a hadronic process, the momentum fraction of the hadron carried by parton and the probability of the interaction of a parton should be known. As mentioned before, the function that describe the distribution of these partons inside the hadrons according to their momentum are called Parton Distribution Function (PDF). The PDFs cannot be calculated fully by using pQCD because of inherent non-perturbative nature of partons. These functions are obtained from experimental measurements such as DIS and fixed target scattering experiments by using the specific energy scale Q_0^2. PDFs generally are denoted by $f(x, Q^2)$ and depend on the energy scale and the momentum fraction carried by parton. If the energy scale is big, quarks carry small part of the total hadron momentum and the internal structure of hadron appear to be significantly gluon. On the other hand, if the energy scale Q^2 is low, resolution inside the hadron is bad (Gunnellini, 2014).

In generally, Dokshitzer-Gribov-Lipoatov-Altarelli-Parisi (DGLAP) matrix equation describes the PDF evolution.

$$Q^2 \frac{\partial}{\partial Q^2} \begin{pmatrix} q_{i(x,Q^2)} \\ g(x, Q^2) \end{pmatrix} = \frac{\alpha_s(Q^2)}{2\pi} \sum_{q_j \bar{q}_j} \int_x^1 \frac{d\xi}{\xi} \times \begin{pmatrix} P_{q_i q_j}\left(\frac{x}{\xi}, \alpha_s(Q^2)\right) & P_{q_i g}\left(\frac{x}{\xi}, \alpha_s(Q^2)\right) \\ P_{g_i q_j}\left(\frac{x}{\xi}, \alpha_s(Q^2)\right) & P_{gg}\left(\frac{x}{\xi}, \alpha_s(Q^2)\right) \end{pmatrix} \begin{pmatrix} q_i(\xi, Q^2) \\ g(\xi, Q^2) \end{pmatrix} \qquad (2.19.)$$

The PDF for quark or gluon with flavour *i* is represented to $q_i(x, Q^2)$ and $g(x, Q^2)$ in Equation 2.16. the $P_{ab}\left(\frac{x}{\xi}, \alpha_s\right)$ correspond to series of splitting functions.

PDF for all quarks can be obtained from experiments. For instance, PDF of up-quark in proton, can be expressed by $u^p(x)$ and $u^p(x)\delta x$ represent the number of up-quarks within proton with momentum fraction between x and $x+\delta x$. Similarly,

$d^p(x)$ defines PDF for down-quark within proton. The gluon and valance quarks distributions at the scale of Q^2 = 1.9 GeV^2 by using inclusive jet measurements at √s= 8 TeV and the HERA data are illustrated in Figure 2.10 (Khachatryan, 2017).

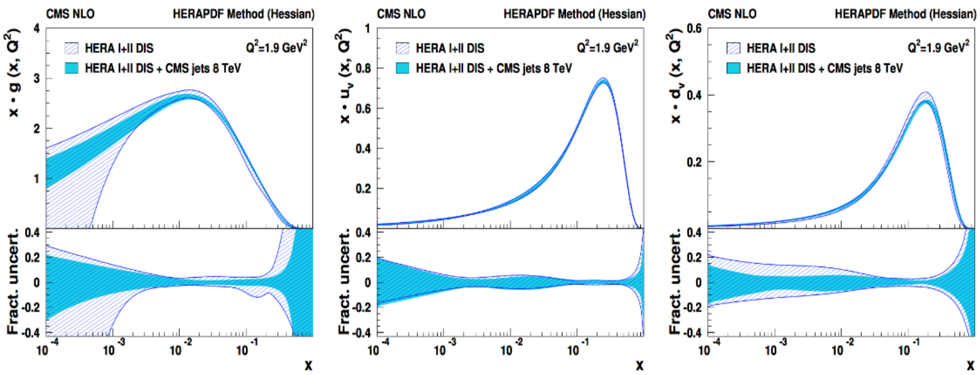

Figure 2.10. The distributions of gluon (left), *u*-valance quark (middle) and *d*-valance quark (right) as a function of *F* at the scale Q^2 = 1.9 GeV^2 (Hos, 2016)

2.4 Phenomenology of Underlying Event

The Underlying Events (UE) are a very important part of the hadronic collisions, consisting of partonic interactions. This valuable component is defined as everything except the hard scattering. In a hadronic collision, it is necessary to understand the UE structure, because it is very important to make more precise measurement of SM processes and also search for new physics at high energies. The UE can be grouped under three different descriptions:

- Initial and Final state radiation (ISR and FSR)
- Beam-beam remnants (BBR)
- Multiple parton interactions (MPI)

During the collision of two hadrons, since they are made up of quark and gluons, a bunch of incoming partons participate in interaction. While several distinct pairs of partons collide with each other, some does not take active part in the collision and are named as beam remnant. The other parts of UE will be explained in section 2.4.1.1 and section 2.4.3

Although some soft interactions in the UE can be calculated within the perturbative framework, the UE often take place under the non-perturbative framework implied phenomenological models based on different kinds of assumption. These models can be tuned to describe the final state using experimental data with the parameters that they have. By looking at the UE in the experimental measurements, these parameters are tuned to correct and improve faulty of phenomenological models (Haevermaet, 2013) (Gunnellini, 2014).

2.4.1 Parton Showers

Because of the composite structure of the beam particles, a hadron-hadron collision has complex calculations. QED and QCD radiation emissions (photon and gluon respectively) can be produced when a hadron-hadron collision occurs. In this process $g \rightarrow gg$, $q \rightarrow qg$, $g \rightarrow q\bar{q}$, $q \rightarrow q\gamma$, $\gamma \rightarrow q\bar{q}$ and $\ell \rightarrow \ell\gamma$, $\gamma \rightarrow \ell\bar{\ell}$ can occur as lepton contributions. Partons involved in the hadronic collisions can emit QCD radiation as gluons. QCD radiations dominate the whole process because of high probability that gluon radiation and splitting which leads to shower effect in a collision, so this process is named as parton shower.

Partons produced in the hadron-hadron collision cannot be directly observed because they fragment and hack into a stream of hadron particles before interacting with detector. The precise calculations of parton shower are based on the perturbation theory but these calculations are complex because of that the number of allowed process increase. Instead, an approximate solution is presented by using different generators which generate parton shower simulation to get rid of these complex calculations.

2.4.1.1 Initial and Final State Radiation

Initial and final state radiation, emitted by partons before and after interaction respectively, has an important role in both soft and hard UE components and can be classified under UE. The measurements related to final-state radiation need to study a leptonic initial state with “coloured" final state while the study of initial state radiation measurements need a hadronic initial state with a leptonic final state.

2.4.2 Hadronization and Fragmentation

Experiments have shown that partons (quarks and gluons) are confined within hadrons because there is no physical condition in which they are observed alone. The increase of strong coupling at long distances leads to confinement while the quarks and gluons at short distances interact with a small coupling. After the conclusion of parton shower, due to the confinement of the outgoing quarks and gluons must form the hadrons which carry zero colour charge. This process is known as *hadronization*. Hadronization process is shown in Figure 2.11. At a scale $Q^2 \sim 1$ GeV where the perturbative method is not valid, the hadronization process begins within the QCD frame. There are different models to describe the transformation from partons to hadrons. These models have been implemented in event generators. Most known hadronization models are the “string” (known as “Lund” model) and the “cluster” model (Brock, 2011) (Driesch, 2016).

The fragmentation describes the QCD radiations which are generated by the partons produced during a QCD process. They are simulated by MC generators similarly to the disintegration of an unstable nucleus. The probability of the particle radiation has a universal expression in the limit where the radiation are collinear and at low energy. It is defined via DGLAP equation to order LO (Altarelli, 1977).

$$dP = \frac{\alpha_s}{2\pi}\frac{dQ^2}{Q^2}\hat{P}(z)dz \qquad (2.20.)$$

where the fraction of the energy recovered by the daughter particle is represented by z and Q is the evolution variable. The fragmentation function defined according to type of fragmentation involved is denoted by P. The fragmentation functions are shown in detail in section 2.3.4. As previously mentioned, when the Q value reaches a minimum value of the order of 1 GeV the fragmentation stops and hadronization begins.

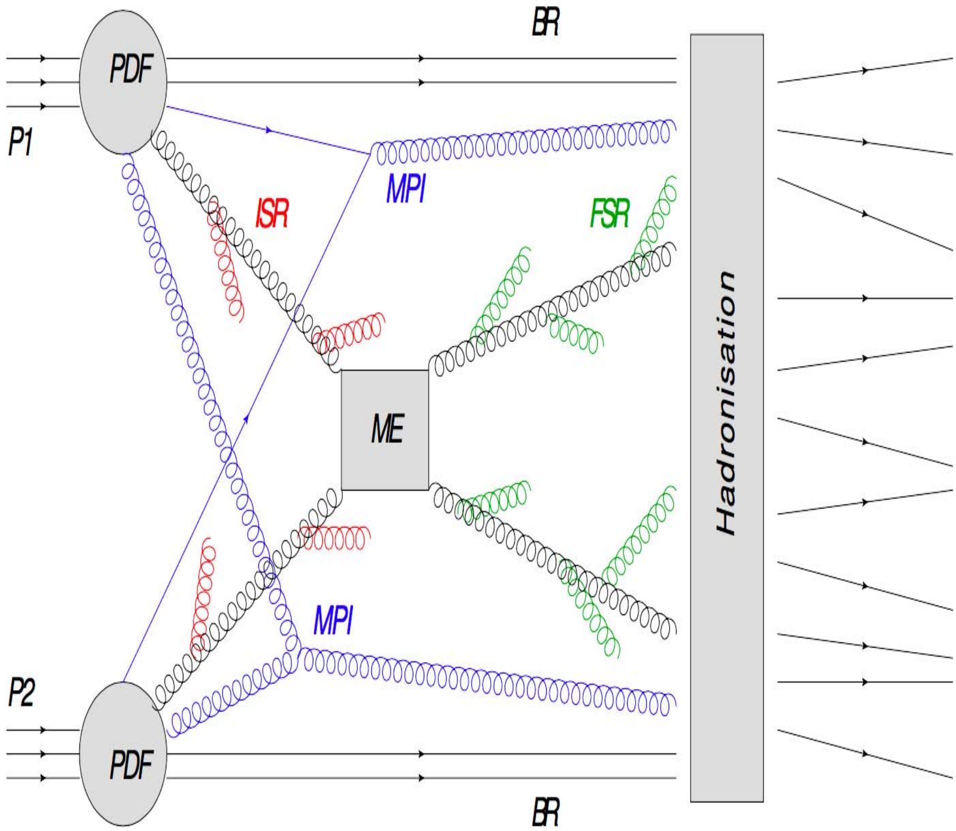

Figure 2.11. Hadronization process

2.4.3 Multiple Parton Interactions

Because of the composite structure of hadrons, a hadron-hadron collision at high energy can cause some complex processes. As discussed in the "Underlying Events-UE" section 2.4, softer interactions can be also occurred in hadronic collisions. These softer interactions named Multiple Parton Interactions (MPI) can be explained within pQCD.

MPI are one of the most important part of the UE. MPI, which show themselves in different ways in hadronic collisions, contain all interactions except hard-scattering. Then it can be expected that there is a relation between typical scale of the partonic scatterings and the multiplicity of partonic scatterings that happen at the same time. There are a lot of hadronic activity in soft regime, which is characterized by small transverse momentum (P_T). The MPI observations for relatively high P_T values focus on two partonic scatterings, such as, on Double Parton Scatterings (DPS). Regrettably, it is difficult to define the MPI in the pQCD depending on the scale of the partonic subprocesses. The pQCD is the most appropriate method to define the MPI in high P_T while it is necessary to make addition to the pQCD in the soft regime (Bartalini, 2011) (Driesch, 2016).

It is important to understand MPI to see the whole picture of hadronic collisions. In order to deal with complexity of hadronic collisions, it is important to understand MPI events in a hadron-hadron collision as much as possible. The evidence for MPI comes from high P_T events observed in hadron collisions. LHC provides great opportunities to measure the influence of MPI (Driesch, 2016).

2.5 Monte Carlo Event Generators and Tunes

We need a tool to compare the experimental results with the predictions from theory like QCD and to give an extrapolation to the experimental results. Therefore, a computer simulation called Monte Carlo (MC) event generator is used. MC event generators reproduce the probability distributions and simulate events in accordance to chosen model. The first step of simulation in MC starts with incoming particles and the hard interaction, then parton shower or bremsstrahlung is generated and finally as the last step hadronization is added. The events generated by MC need to have the same fluctuation and average behaviour as the actual data. These fluctuations in data resulting from quantum effects are simulated by MC using an algorithm.

The MC event generators in particle physics have applications for different purposes. These applications can be summarized as follows:

- useful to determine how events will appear and at what rates.
- help to design new detectors by optimizing current detector performance. The simulation of detector can be done with programs like GEANT.
- useful in determining the analysis strategy and signal-background studies.
- used to estimate detector acceptance corrections. The real signal is obtained by using these corrections (Driesch, 2016).

At MC event generators, if there is a hard interaction between the partons of the incoming hadrons than cross section equation can be written as follows:

$$\sigma(P_1, P_2) = \sum_{i;j} \int dx_1 dx_2 f_i(x_1, \mu^2) f_j(x_2, \mu^2) \hat{\sigma}_{ij}(p_1, p_2, \alpha_s(\mu^2), Q^2/\mu^2) \qquad (2.21.)$$

in which μ^2 is known factorization scale and Q^2 shows the scale of the hard process. The $\hat{\sigma}_{ij}$ indicates the cross section of two incoming partons (*i* and *j*) which are involved in hard interaction and can be calculated inside pQCD. The functions $f(x, \mu^2)$ are known as PDFs while x_i and x_j represent the momentum fractions for both incoming and outgoing partons. The momenta of incoming and outgoing protons can be calculated using this momentum fraction. They are given by $p_1 = x_1 P_1$ and $p_2 = x_2 P_2$. In which P_1 and P_2 represent the momenta of two incoming hadrons. The momentum fraction, x, cannot be subtracted from pQCD calculations, therefore the parton density function related the momentum fraction is considered in non-perturbative frame. But it can be calculated within perturbation theory, depending on their μ scale. These quantities lead to a set of evolution equations.

- The DGLAP equation (named after the authors Dokshitzer, Gribov, Lipatov, Altarelli, Parisi)
- The BFKL equation (The Balitsky-Fadin-Kuraev-Lipatov)
- The CCFM equation (Ciafaloni-Catani-Fiorani-Marchesini)

The DGLAP evolution equation defines effectively the data with high Q^2 values and in a condition that x is not too large. The DGLAP evolution equation based on this assumption that $\log(Q)$ is much bigger than $\log\left(\frac{1}{x}\right)$. The $\log\left(\frac{1}{x}\right)$ scheme are neglected in the Leading Log Approximation (LLA) that the DGLAP evolution equation uses. The DGLAP evolution equations are given by (Gwenlan, 2003).

$$\frac{dq_i(x,Q^2)}{d\ \log Q^2} = \frac{\alpha_s}{2\pi}\int_x^1 \frac{dy}{y}\left[\sum_i q_i(y,Q^2)P_{qq}\left(\frac{x}{y}\right) + g(y,Q^2)P_{qg}\left(\frac{x}{y}\right)\right] \qquad (2.22.)$$

$$\frac{dg(x,Q^2)}{d\ \log Q^2} = \frac{\alpha_s}{2\pi}\int_x^1 \frac{dy}{y}\left[\sum_i q_i(y,Q^2)P_{qg}\left(\frac{x}{y}\right) + g(y,Q^2)P_{gg}\left(\frac{x}{y}\right)\right] \qquad (2.23.)$$

Here, the quark density function for each flavour is indicated by $q_i(x, Q^2)$, in the same way the gluon density function is represented by $g(x, Q^2)$ and the function known as the Alterelli-Parisi splitting functions, $P_{jk}\left(\frac{x}{y}\right)$, show the probability of a parton k (having a momentum fraction *y*) originating from a parton j (having a momentum fraction *x*). These splitting functions have been calculated to LO and NLO in QCD. The solution of the DGLAP evolution equations give us the PDFs depending on the momentum fraction *x* and the hard-scattering scale Q^2 (Gwenlan, 2003) (Hos, 2016).

As already mentioned, the DGLAP evolution equation cannot applied at very small *x* values, for this reason, the BFKL evolution equations allowing the re-summation of terms with $\left(\alpha_s log\left(\frac{1}{x}\right)\right)^n$ and $\alpha_s\left(\alpha_s log\left(\frac{1}{x}\right)\right)^n$ are used. As a consequence, it is expected that the BFKL evolution scheme will be effective in the region of applicable Perturbative Quantum Chromodynamics (pQCD) where $log\left(\frac{Q^2}{Q_0^2}\right) \ll log\left(\frac{1}{x}\right)$. The evolution equation BFKL describing the evolution of the unintegrated parton densities as a function of *x* is expected to become valid with partons strongly ordered in fractional momentum x_i:

$$x_0 >> x_1 >> \cdots x_{n-1} >> x_n \tag{2.17.}$$

And also, there is no ordering on transverse momenta k_T. The integrated gluon density $g(x, Q^2)$ at small *x* can be calculated using the unintegrated gluon distribution function $\mathcal{G}(x, k_T^2)$. The integrated gluon density can be written as,

$$xg(x, Q^2) = \int_0^{Q^2} \frac{dk_T^2}{k_T^2} \mathcal{G}(x, k_T^2) \tag{2.18.}$$

The integrated parton density function can be written in same way using the unintegrated parton density function. Consequently, the evolution equation of BFKL can be written as,

$$\frac{d\mathcal{G}(x, k_T^2)}{d\log(1/x)} = \int \grave{k}_T^2\, K\big(k_T^2, \grave{k}_T^2\big)\mathcal{G}(x, k_T^2) \tag{2.19.}$$

where K, is the kernel known as splitting operator. As mentioned earlier, the $\mathcal{G}(x, k_T^2)$ is the unintegrated gluon distribution function and $k_T(k_T^{'})$ is the transverse momentum of the parent parton (originated parton). The CCFM evolution equation defines the small x and large Q^2 values regions where both the DGLAP and BFKL evolution equations are missing in the description.

There are various MC event generators being used in high energy physics. In this thesis; PYTHIA, QGS and EPOS are used for the comparison and detailed in the following sections.

2.5.1 PYTHIA

PYTHIA (Sjöstrand, 2015) program, one of the most widely used, is a general-purpose and multifunctional event generator in high energy physic. PYTHIA produces hard or soft processes in a collision and calculates parton dynamics using the DGLAP equations. During calculation of parton dynamics, the contributions of the UE such as ISR, FSR, MPI and BBR are taken into account. In this program, PYTHIA, quarks and gluons are hadronised with the Lund string fragmentation model. According to this model the partons are connected by string and these strings gain energy up to the last breaking point to separate the partons from each other. After breaking, quark-anti-quark pairs occur.

Just like all other MCs, PYTHIA uses different tunes to define successively the experimental data such as MONASH, MBR, CTEQ2L … etc. These tunes are constructed using some parameters in PYTHIA and tool like Professor, which is a program for tuning model parameters of MC event generators.

2.5.2 Cosmic Ray Event Generators

Our planet is constantly exposed to radiation caused by high energy particles called cosmic radiations (CRs). The CRs are separated into two groups: the primaries are cosmic radiations caused by the astrophysical sources such as supernova explosions, pulsars, active galactic nuclei etc. The secondary ones are produced by the interaction of the primaries with the interstellar medium. The first measurements of cosmic radiation were made by Victor Hess in 1912 by measuring ionization of atmosphere as a function of altitude. Since their discovery, many experiments have succeeded to measure the composition and flow of cosmic radiation as a function of energy. In total, the CRs compose of about 86% proton, 11% helium and the rest are electrons, heavier nuclei and a small amount of anti-matter (Hess, 1912) (Stanev, 2010).

The CRs entering the atmosphere of the Earth interact with air nuclei and cause the particle shower called “extended air-shower” (EAS). The determination of CRs and their effects is an important issue in terms of fully understanding hadronic interaction. Therefore, the hadronic MC models which describe the interactions of the primary CRs in the upper atmosphere are used to determine the energy and mass of primary ones. Most of primary particle production is controlled by forward and soft QCD interactions. These interactions are modelled Regge-Gribov-bassed approaches. In this analysis, QGSJET II and EPOS MC models were used to understand such effects (David d’Enterria et all, 2008).

QGSJET II : Cosmic ray (CR) investigations play an important role in the modelling of MC at high energy interactions. The QGSJET II (Ostapchenko, 2011) describing multiple scattering, is an addition of Gribovs Reggeon approach to the Quark Gluon String model at high energies. The QGSJET model has been extensively used in order to analyse and interpret data of various experiments. In the multiple scatterings, contributions of scattering in hadronic processes are defined as Pomeron exchanges which correspond to parton (quark, gluon) cascades. The assumption in QGSJET is that Pomeron exchanges in hadronic processes take place independent of each other, but this assumption is not true at high energy regime because parton cascades interact with each other at high energies. This non-linear effects are describe as Pomeron-Pomeron interactions.

In QGSJET II, hadronic interactions are evaluated in the framework Gribov's reggeon approach. The Reggeon Field Theory (RFT) takes contributions from both "soft" and "hard" parton dynamics to the interaction into consideration. Soft non-perturbative interactions, dominating hadronic collisions, play an important role in the calculation of the total and inelastic cross section. Additional, soft non-perturbative interactions are defined as soft Pomeron exchanges.

EPOS : It is a sophisticated MC event generator based on the Parton-Based Gribov Regge Theory. EPOS (Pierog, 2015) was developed by combining two different model VENUS, NEXUS. EPOS is used for minimum bias hadronic interaction generation and particle physics experiment analysis in p-p and heavy ion collisions. EPOS, which stands for

- **E**nergy conversing quantum mechanical multiple scattering approach, based on
- **P**artons (parton ladders)
- **O**ff-shell remnants
- **S**plitting of parton ladders.

EPOS, being a quantum mechanical parton model, consist of many binary parton-parton interactions, each one caused parton ladders.

3 EXPERIMENTAL SETUP

Particle accelerators play an important role in the research of particle physics and the discovery of new physics. These accelerators are divided into two types as colliding beam machine and fixed-target experiment. The first one uses two accelerated beams in collision while the second one uses a single particle beam to fire at a stationary target. Table 3.1 shows some collider and some parameters of them (Thomson, 2013).

Table 3.1. Particle accelerators and their basic parameters (Thomson, 2013)

Collider	Laboratory	Type	√s/GeV	Luminosity /cm^{-2}s^{-1}
PEP-II	SLAC	$e^- e^+$	10.5	1.2×10^{34}
KEKB	KEK	$e^- e^+$	10.6	2.1×10^{34}
LEP	CERN	$e^- e^+$	90 - 209	10^{32}
HERA	DESY	$e^- p/e^+ p$	320	8×10^{31}
Tevatron	Fermilab	$p\bar{p}$	1960	4×10^{32}
LHC	CERN	$p\,p$	14 000	10^{34}

The most powerful accelerator ever built in the world is the Large Hadron Collider (LHC) in Geneva region will be discussed in this chapter.

3.1 The Large Hadron Collider

The Large Hadron Collider (LHC) is a superconducting hadron accelerator and collider has a length of 27 km tunnel located about 100 m underground. LHC located at the French Swiss border near Geneva has been designed to collide protons or heavy nuclei, at center-of-mass energies of up to √s=14 TeV. LHC has a design luminosity of 10^{34} cm^{-2}s^{-1}. The one of the main reason to build LHC is the searching the Higgs mechanism, which is presumed to be responsible for electroweak symmetry breaking. Also, LHC is an important machine to examine the measurements in QCD.

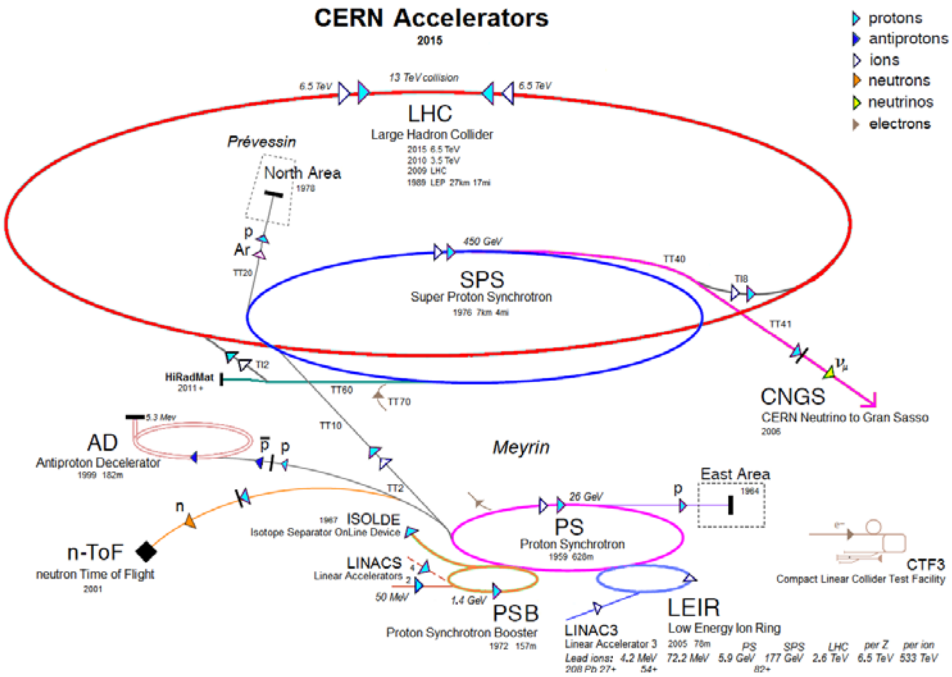

Figure 3.1. CERN Accelerator System (Evans L. and Bryant, 2008)

The accelerator has two rings to accelerate the protons in opposite directions. Protons, obtained from hydrogen gas, are accelerated to 50 MeV in a linear accelerator called LINAC. After that they are injected into Proton Synchrotron Booster (PSB) being the first circular accelerator. The PSB accelerates the protons to 1.4 GeV. The protons than enter the Proton Synchrotron (PS), whose has radius of 100 m accelerating them up to 25 GeV. The next-last-step is the accelerating the protons in Super Proton Synchrotron (SPS) up to 450 GeV. From the SPS whose has radius of 1 km, protons are injected into the LHC where they reach the final energy. The diagram of CERN accelerators complex is given in Figure 3.1.

At the LHC, there are two general purpose detectors, ATLAS and CMS. In addition to these, there are two specialized experiment namely ALICE and LHCb. ATLAS and CMS examine the Higgs boson, precision testing of the SM and studies new physics at the high energies. ALICE being a detector at the LHC is devised to study the quark plasma at very high energies and also to examine hadrons, electrons, muons and photons produced in heavy-ion collision. And LHCb is built to study B-physics and the mater-antimatter imbalance (Evans L. and Bryant, 2008).

3.2 The CMS Experiment

One of the two largest and most powerful particle physics detectors ever built, CMS, located at interaction point 5 of the LHC with a design luminosity of 10^{34} $cm^{-2}s^{-1}$ is a general-purpose detector designed to discover the physics at TeV scale. The main designing goals of CMS are providing quality of central tracking, achieving a high performance of muon system, the best possible electromagnetic calorimeter and a hadron calorimetry with sufficient energy resolution and good hermiticity. CMS is established about 100 meters underground close to French village of Cessy, between Lake of Geneva and the Jura mountains (Chatrchyan S.,et al., 2008). The primary goals of the experiment are to reveal the electroweak (EWK) symmetry breaking mechanism and provide evidence of physics beyond the SM in p-p collisions at $\sqrt{s}$=14TeV.

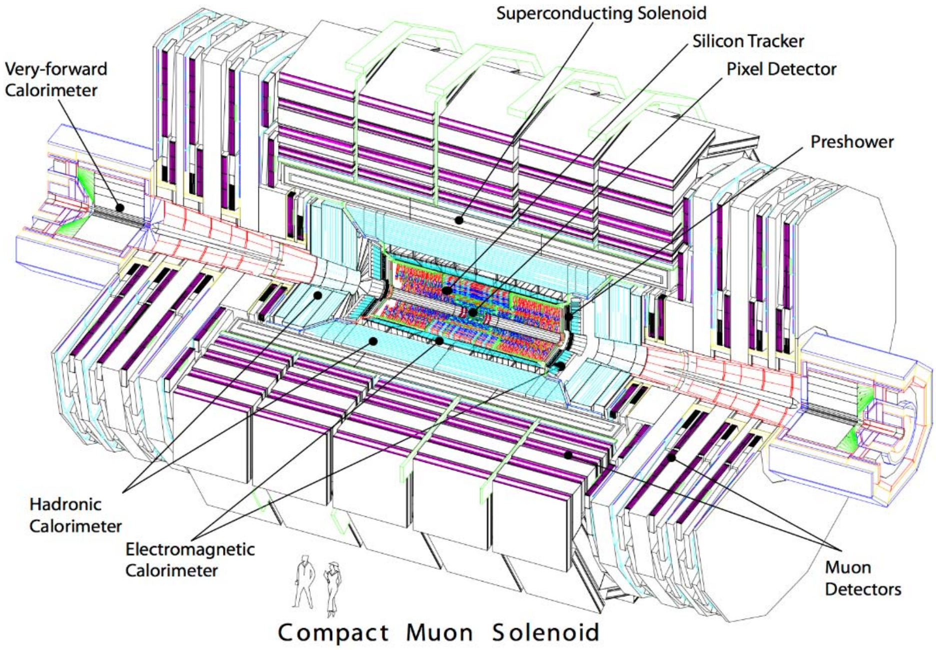

Figure 3.2. Compact Muon Solenoid (CMS) detector (Chatrchyan S.,et al., 2008)

The CMS detector is designed in cylinders arranged concentrically as shown in the Figure 3.2. The CMS detector as a whole are a length of 28.7 m, a diameter of 14.6 m and has a total weight by a steel "yoke" around 14500 tonnes. It is divided parts as an all-silicon-based inner tracking system, a homogeneous scintillating-crystal-based electromagnetic calorimeter, a fully hermitic brass-scintillator hadron detector, superconducting solenoid magnet and muon system, respectively from inside to outside. The tracking system of the CMS makes it possible to measure the charged particles from collisions by means of the magnetic field of 3.8 T. Electromagnetic calorimeter provides to measure the energy of the particle participated in electromagnetic interaction like photon and electron while hadronic calorimeter allows to measure the energy of hadrons. Finally, muon system in CMS is designed to measure the momentum of muon. The key element of CMS detector is superconducting solenoid magnet provides a magnetic field of

3.8 Tesla. Figure 3.3 shows the detection process of different types of particles by CMS detector. (Chatrchyan S.,et al., 2008).

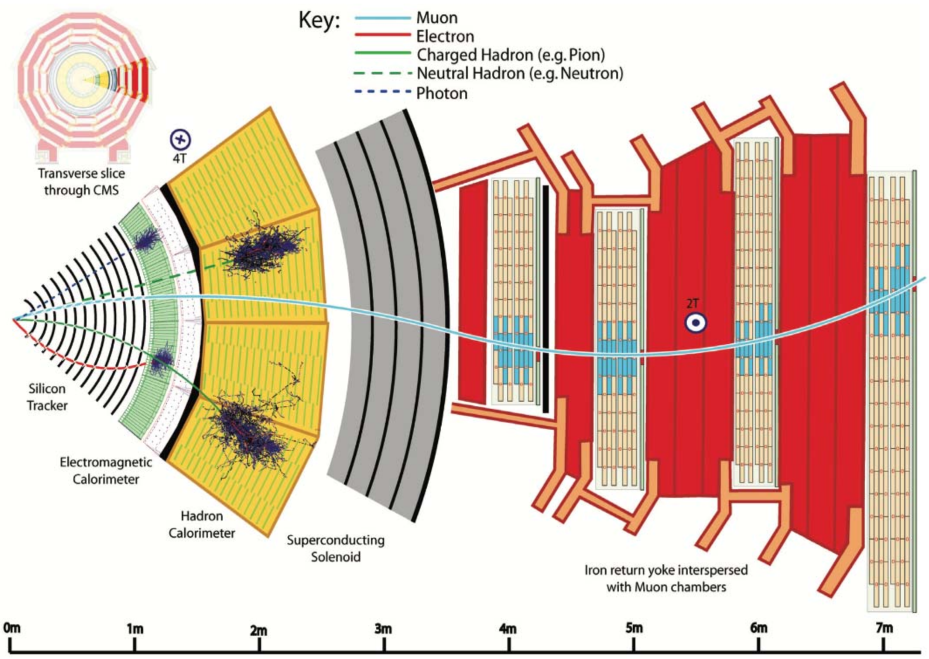

Figure 3.3. Detection process of the CMS detector (Lazaridis, 2011)

3.2.1 The Coordinate System of CMS

The interaction point of collision is taken the origin of the system. The coordinate system adopted by CMS is oriented such that the *x*-axis indicates towards south to the center of the LHC ring, the *y*-axis indicates vertically upward and *z*-axis is in the direction of the beam to the west. The transverse plane in CMS coordinate system is defined by the *x-y* plane. The *r*, ϕ and *z* are defined as the associated cylindrical coordinate system. ϕ, known as azimuthal angle, is measured from the x-axis in the x-y plane and character *r* represents the radial coordinate in this plane. θ, known as the polar angle, is defined in the *rz* plane with respect to the z-axis. The pseudorapidity is defined as below by using the polar angle θ:

$$\eta = -\ln \tan(\frac{\theta}{2})$$

Also, rapidity is defined as a function of energy (E) and momentum component along the z-axis (P_Z).

$$y = \frac{1}{2}\ln\left(\frac{E+P_Z}{E-P_Z}\right)$$

Figure 3.4 shows the definition of the CMS coordinate system taking into account that the geometry of CMS detector is a cylindrical structure around the beam circulation axis.

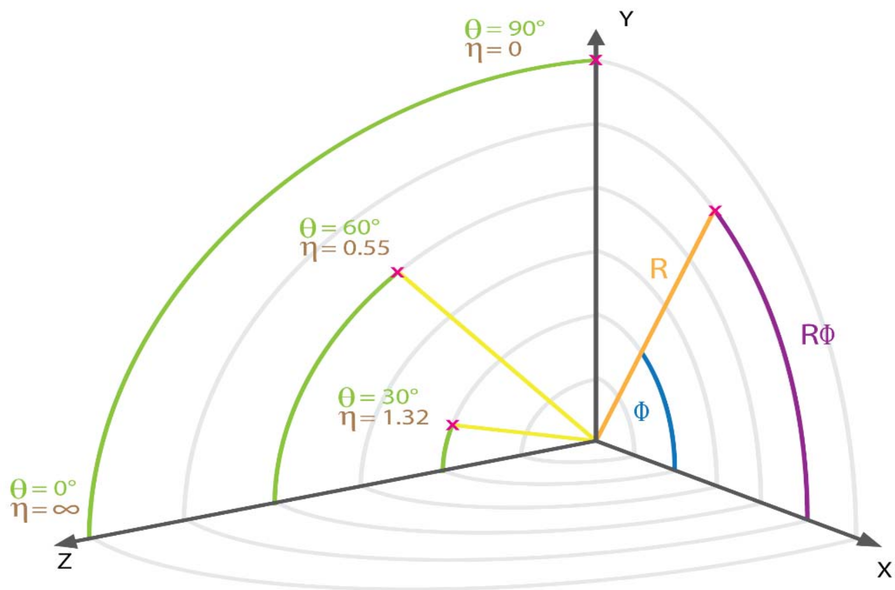

Figure 3.4. A graphical representation of CMS coordinate system (Lenzi, 2013)

Addition, the CMS coordinate system is shown on part of the CMS detector in Figure 3.5.

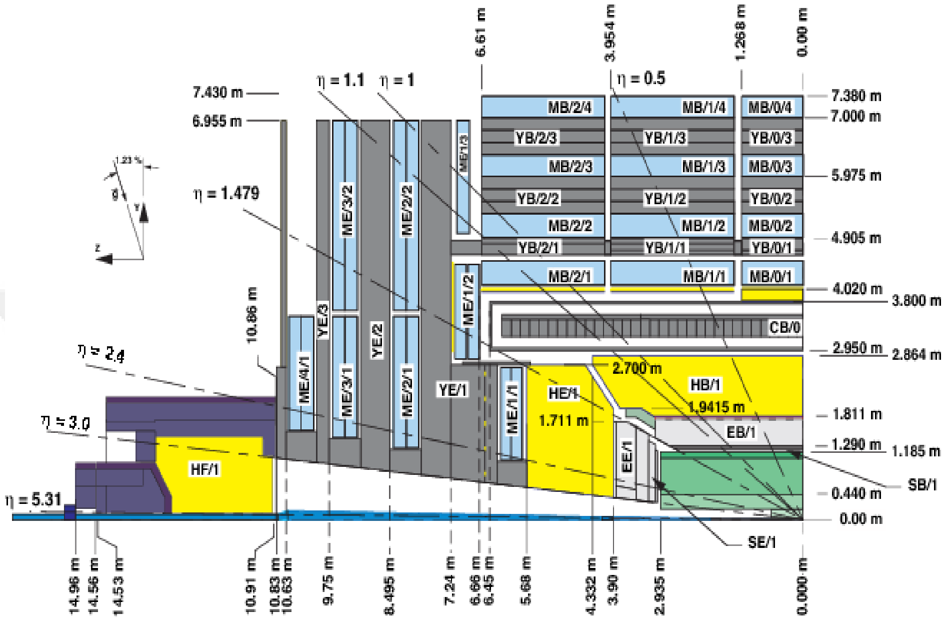

Figure 3.5. CMS Coordinate System (Bayatian G.L., et al., 2000)

3.2.2 Tracking System

The interaction point is surrounded by tracking system which has a length of 5.8 m and diameter 2.5 m. It was designed to provide a precise and efficient measurement of the trajectories of charged particles emerging from the LHC collision and to detail a reconstruction of secondary vertices. A homogeneous magnetic field over the tracker is provided by the CMS solenoid. Under nominal operating conditions of the LHC, average more than 1000 particle will be generated at the point of interaction due to the interaction of 20 protons per 25 ns. Therefore, the tracker system of the CMS must be a detector which has high granularity, fast and resistant to radiation. The tracker system of the CMS is made out of a pixel detector and a silicon strip tracker. The pixel detector composed of three detection layer in the barrel at radii between 4.4 cm and 10.2 cm. The pixel detector covering an area of approximately of 1m^2 has 1440 pixel modules. The pixel system in CMS contributing precise measure of tracking point in in *r*- ϕ and *z* is important for good reconstruction of the secondary vertex. The silicon strip tracker of CMS will be by far the largest silicon tracker in the world, it is important for efficient mass production and rigid quality control. The silicon strip tracker occupied the region between 20 cm and 116 cm. The silicon strip tracker is composed of four different subsystems which has 15 148 detector modules. These four basic detectors are The Inner Barrel (TIB), The Inner Disk, (TID), The Outer Barrel (TOB) and a Tracker End Cup (TEC). A schematic view of CMS tracking system is shown in Figure .3.6. (Chatrchyan S.,et al., 2008).

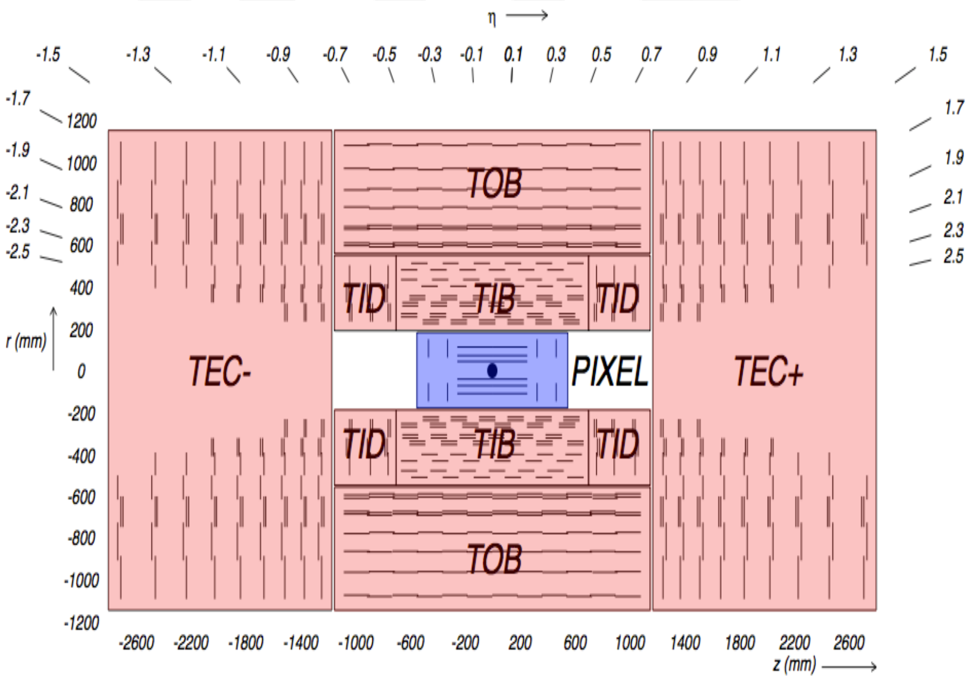

Figure 3.6. A shematic view of CMS tracking system. Each detector module and back-to-back modules are represented by a line and double lines respectively (Chatrchyan S.,et al., 2008)

3.2.3 Electromagnetic Calorimeter

The electromagnetic calorimeter (ECAL) has been designed to be a radiation-resistant, fast response and compact detector. Lead tungstate crystal ($PbWO_4$) were chosen as scintillating materials for ECAL calorimeter. Because of that $PbWO_4$ crystal has high density (8.28 g/cm^3), short radiation length (0.89 cm), small Moliere radius (2.2 cm), fast response time and good radiation resistance. Scintillation crystals are used to measure of electromagnetically interacting particles, likely electrons and photons. ECAL made of 61200 $PbWO_4$ crystals in barrel region and 7324 ones in the endcaps. ECAL is a hermitic homogeneous detector with a large pseudorapidity coverage up to $|\eta| < 3$.

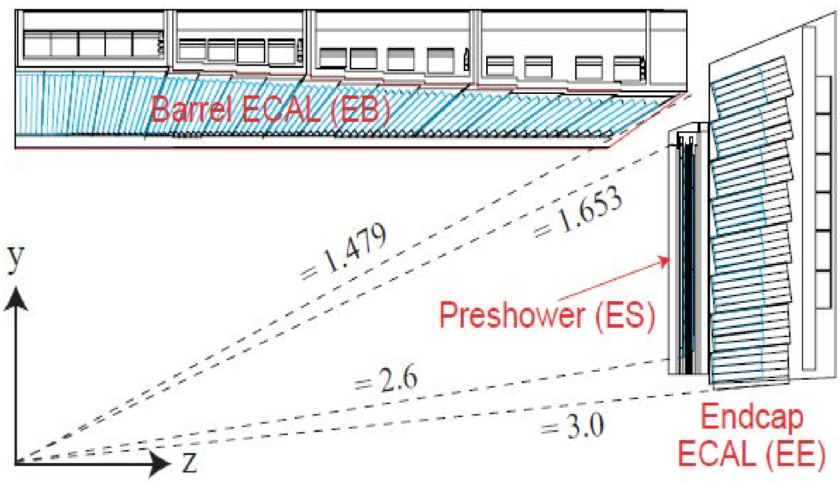

Figure 3.7. A geometric view of one quarter of the ECAL (CMS Collaboration, 1997a)

The ECAL is composed of two regions named as Electromagnetic Barrel (EB) and Electromagnetic Endcap (EE). The EB part of ECAL covers the pseudorapidity range of $|\eta| < 1.479$. The EE part of ECAL covers pseudorapidity of $1.479 < |\eta| < 3$. The EB has a volume of 8.14 m^3 and front face of EB is at radial distance of 1.29 m from the interaction point. The EE is located a longitudinal distance of 3.15 m from the interaction point. In addition, the ECAL contain a detector called the ECAL preshower (ES) located in front of the EE part of ECAL. The ES detector has been designed to identify neutral pions in critical pseudorapidity ranges of $1.653 < |\eta| < 2.6$. Moreover, it plays an important role in determining the exact position of electron and muon thanks to its high granularity. The Figure 3.7 shows one quarter of the ECAL (CMS Collaboration, 1997a).

The following expression can parametrize the energy resolution of electromagnetic calorimeter:

$$\left(\frac{\sigma}{\mathrm{E}}\right)^2 = \left(\frac{\mathrm{S}}{\sqrt{\mathrm{E}}}\right)^2 + \left(\frac{\mathrm{N}}{\mathrm{E}}\right)^2 + \mathrm{C}^2$$

where *S* is known as the stochastic term which has three basic contributions. These contributions are given as event to event fluctuations, a photostatistics contribution of 2.1% and fluctuations in the energy deposited in the preshower absorbers in ECAL. *N* represent to noise term which involves contributions of the electronic noise. The constant term is represented by *C* which respect to some contributions. These contributions are non-uniformity of the longitudinal light collection, intercalibrations errors and leakage of energy from the back of the crystal.

3.2.4 Hadronic Calorimeter

The hadronic calorimeter (HCAL) of CMS has been designed to measure the energy of neutral and charged hadrons. HCAL particularly important for the measurement of hadron jets and neutrinos or exotic particles. HCAL, located behind the tracker and ECAL (as seen from the point of interaction), covers the covers the pseudorapidity region $|\eta| < 5.2$. HCAL consist of four sub-detectors:

- İnner Hadronic Barrel (HB)
- Hadronic Outer (HO)
- Hadronic Endcap (HE)
- Hadronic Forward (HF)

These sub-detectors are shown in Figure 3.8 with the longitudinal view of CMS. All sub-detectors are composed of two parts as an absorber part and a scintillator part therefore HCAL is a sampling calorimeter. Absorber part of HCAL leads to trigger and develop hadronic sheaf while scintillator part provides to measure the energy of the particle.

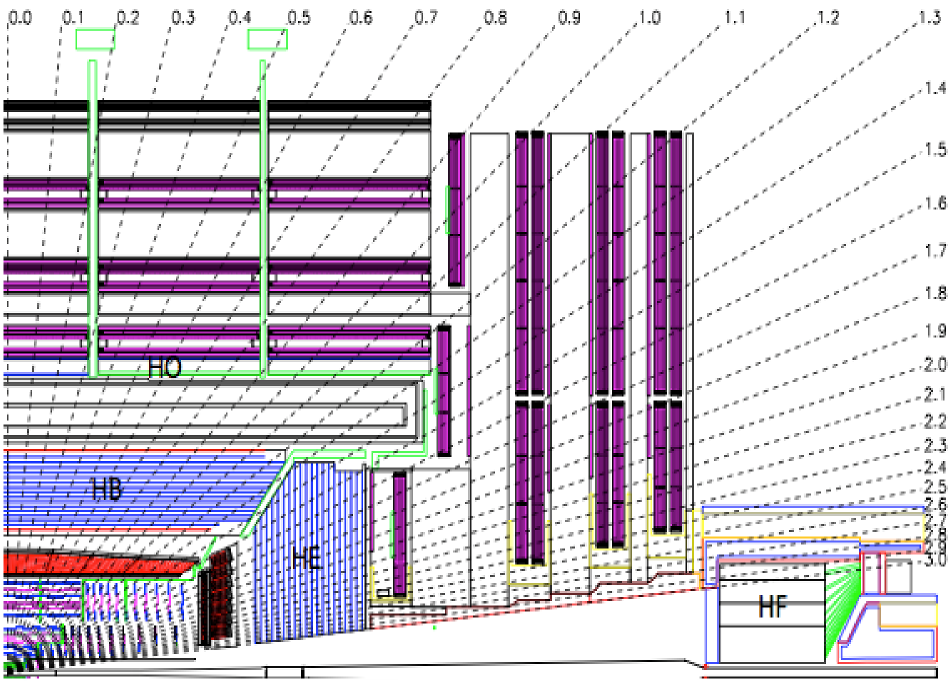

Figure 3.8. Longitudinal view of the CMS detector (Chatrchyan S.,et al., 2008)

The HB part of HCAL is located between ECAL (r <1.77 m) and the solenoid magnet of CMS (r < 2.95 m) on the pseudorapidity range of $|\eta| < 1.3$. The HB calorimeter plays an important role to measure the missing transverse energy. HB is separated into two half barrel as HB+ and HB– and each half-barrel consist of 18 wedges which are developed out of the flat brass absorber. A schematic view of HB wedges is shown in Figure 3.9. The brass has been retained because it is not sensitive to magnetic field generated by solenoid magnet of CMS.

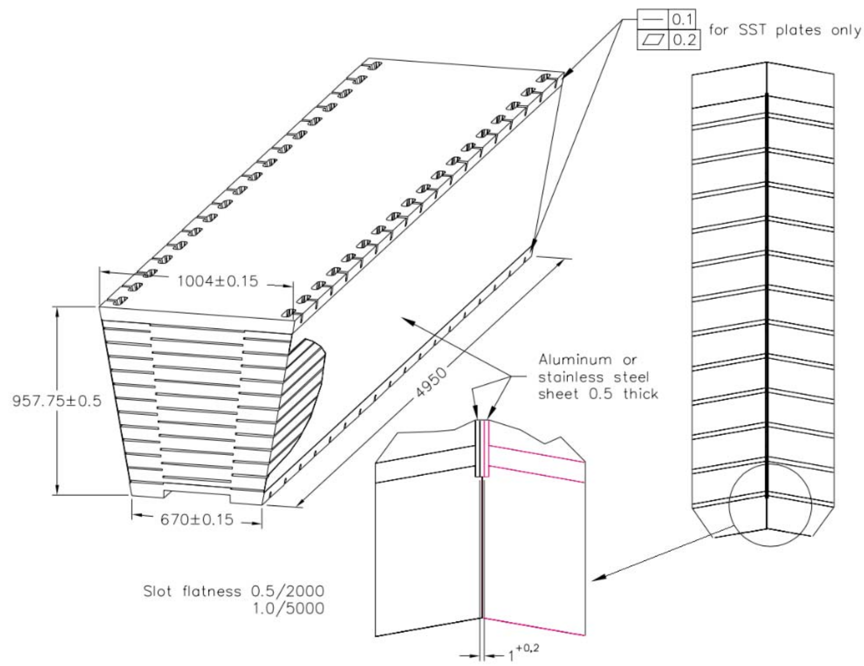

Figure 3.9. The shematic view of the HB wedges (Chatrchyan S.,et al., 2008)

Each wedge also subtends 20 degrees of $\emptyset$ and extends from CMS detector mid-plane about 4.3 meter in z and weighs 25.7 metric tonnes.

The HO of HCAL is extended over outside the entire length of the iron for return of field $|\eta| < 1.3$. The HO has been designed to recover the energy loss of hadronic shower behind the volume of HB. The HO calorimeter is divided into five rings which are compatible with the structure of the muon ring. These rings are named as -2, -1, 0, 1 and 2 with increasing η. The HO calorimeter constrained by the geometry of the muon system is shown Figure 3.10.

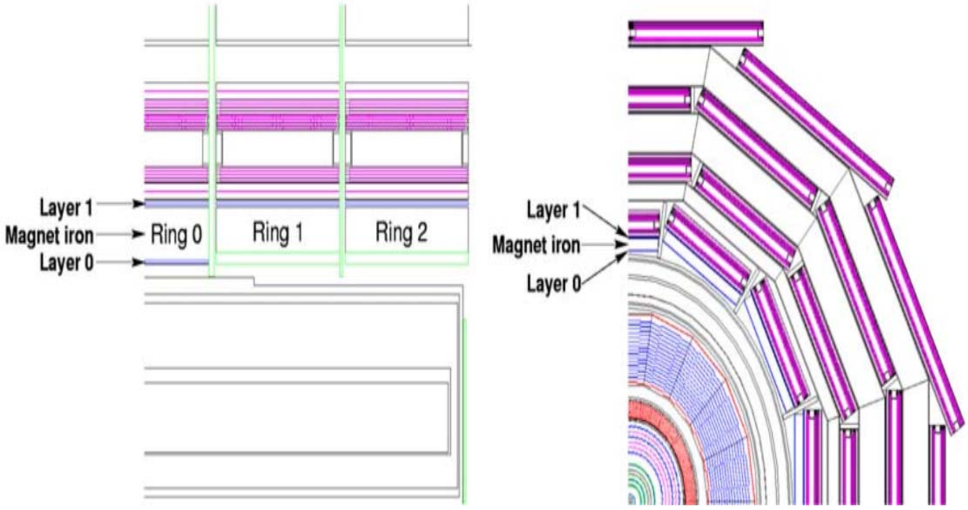

Figure 3.10. HO calorimeter and the position of the HO layer in the rings (Chatrchyan S.,et al., 2008)

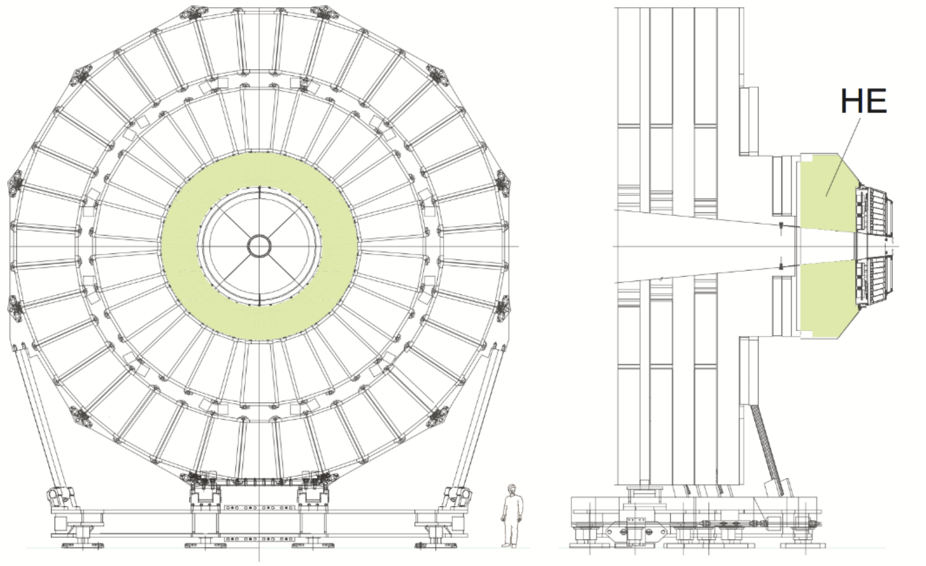

Figure 3.11. The HE calorimeters mounted on the CMS detector (Chatrchyan S.,et al., 2008)

The pseudorapidity range of $1.3 < |\eta| < 3$ in CMS is occupied by the HE. In addition, the region of HE contains about 34% of the particles produced in final state. It is a fast detector which has high radiation resistance because of the high luminosity of the LHC (10^{34} $cm^{-2}s^{-1}$). Non-magnetic material is used as an absorber in HE in order to avoid the influence of magnetic field since HE is embedded into the ends of solenoid magnet. The HE calorimeter mounted on CMS detector is shown in Figure 3.11.

The HF is placed in a longitudinal distance of 11.2 m from the interaction point on both sides of detector and covers a large pseudorapidity range of $3 < |\eta| < 5$. The HF detectors in CMS plays an important role to improve jet detection and missing transverse energy resolution. The HF exposes to high radiation because of that average 760 GeV energy per interaction is deposited in the HF while average 100 GeV energy per interaction is deposited in the rest of detector. Therefore, quartz fibers that provides strong resistance to radiation were chosen as the active elements and over 1000 km of fibers are used in HF calorimeters. Using these fibers in HF calorimeter, the signal is generated by detecting the light of the hadronic shower particles above Cherenkov threshold ($E > 190$ keV for electron).

The HF calorimeter has a steel absorber structure composed of 5 mm thick grooved plates. Fibers are placed in these grooves. The HF detector is functionally subdivided into two longitudinal segments; half of the fibers named as long fiber (L) run over the full depth of absorber (165 cm $\approx 10\lambda_I$), other half named short fiber (S) starts at a depth of 22 cm from the front of detector. These two sets of fibers read out separately make it possible to distinguish shower generated by electrons and photons. The calorimeter is essentially a cylindrical steel structure subdivided into 20^omodular wedges and HF calorimeter consist of thirty-six such wedges (18 on either side of the interaction point). The entire calorimeter system is placed in a shielding component which comprise of layers of 40 cm thick steel, 40 cm of concrete and 5 cm of polyethylene. The shielding segments provides a hermitic radiation protecting. Figure 3.12 shows a cross sectional view of the HF.

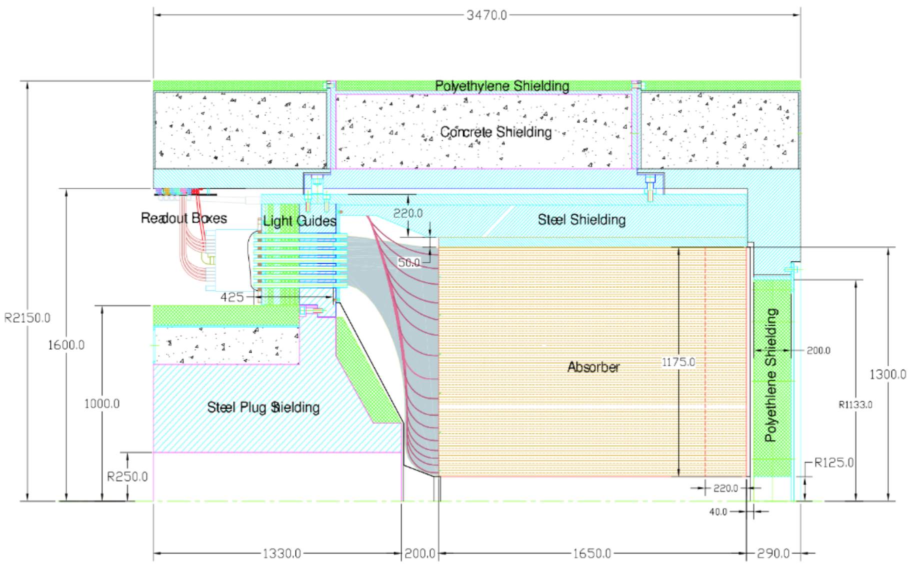

Figure 3.12. The cross sectional view of the HF. All dimensions are in mm (Chatrchyan S.,et al., 2008)

3.2.5 Magnet

The superconducting magnet with a 12.5 m long and 6 m diameter is a very important instrument for CMS. The superconducting magnet for CMS, which has been designed to reach a 4 T field, provides the measurement of transverse momentum of charged particle using the curvature of it in magnetic field. The iron yoke instrumented with muon stations provides to return the magnetic field. The magnetic flux is generated by the superconducting coil. At the same time, it is surrounded by a 1.5 m thick saturated iron yoke. The return yoke designed as a 12-sided structure plays an important role to identify well muon momentum resolution and trigger capability. There is a balance between the outer diameter of the yoke and size of the muon stations while trying to maximise the azimuthal acceptance for measurement of the muon. Two main components composed of the yoke. These are named as the barrel yoke (the cylinder surrounding the superconducting coil) and endcap yoke (the disk that magnetically close the barrel yoke). The superconducting magnet is the most powerful magnet ever built. The capacity of magnet at the full current is a stored energy of 2.6 GJ. The field of 3.8 T brings substantial benefits not only for the muon tracking and inner tracking but also for electromagnetic calorimetry. The iron return yoke with weight of 10000 tons is composed of five barrels and two endcaps of three layers each (CMS Collaboration, 1997c)

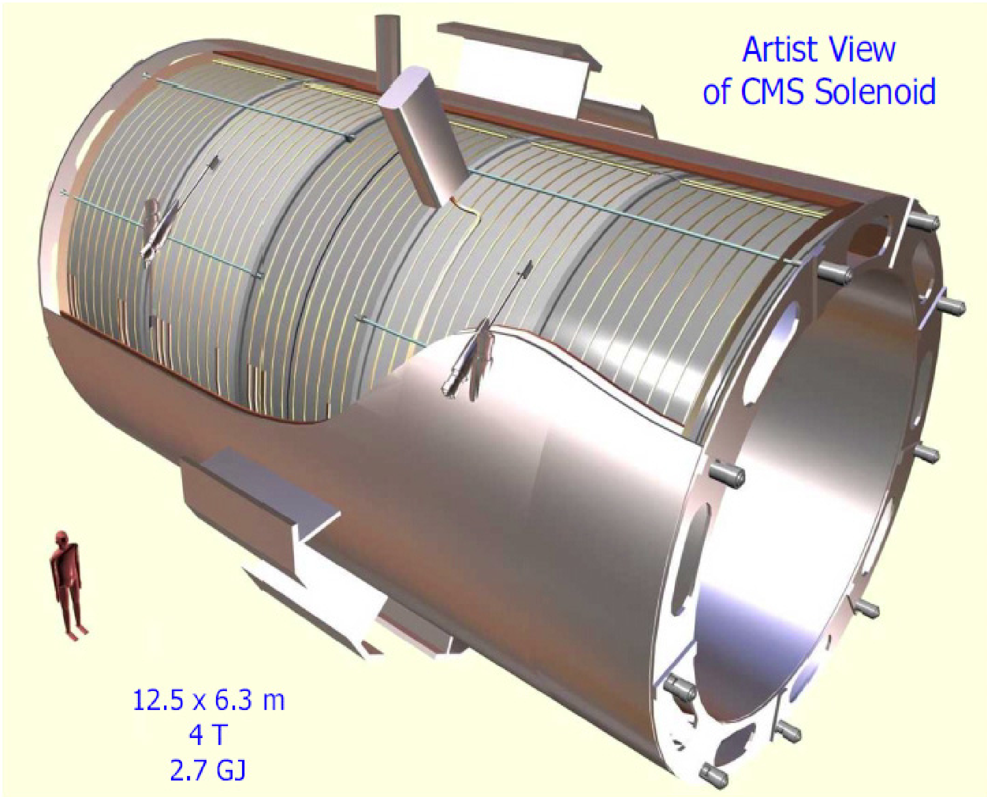

Figure 3.13. CMS Solenoid Magnets (Chatrchyan S.,et al., 2008)

3.2.6 Muon System

The muon system of the CMS is placed at the edge of experiment because the muons can pass through significant amount material without losing much energy because of its big mass. The muon system has three goals: muon idenfication, measurement of muon momentum and triggering. The muon system consists of about 25000 m^2 of detection planes. The high field solenoid magnet and its flux-return yoke play an important role for good muon momentum resolution and trigger capability.

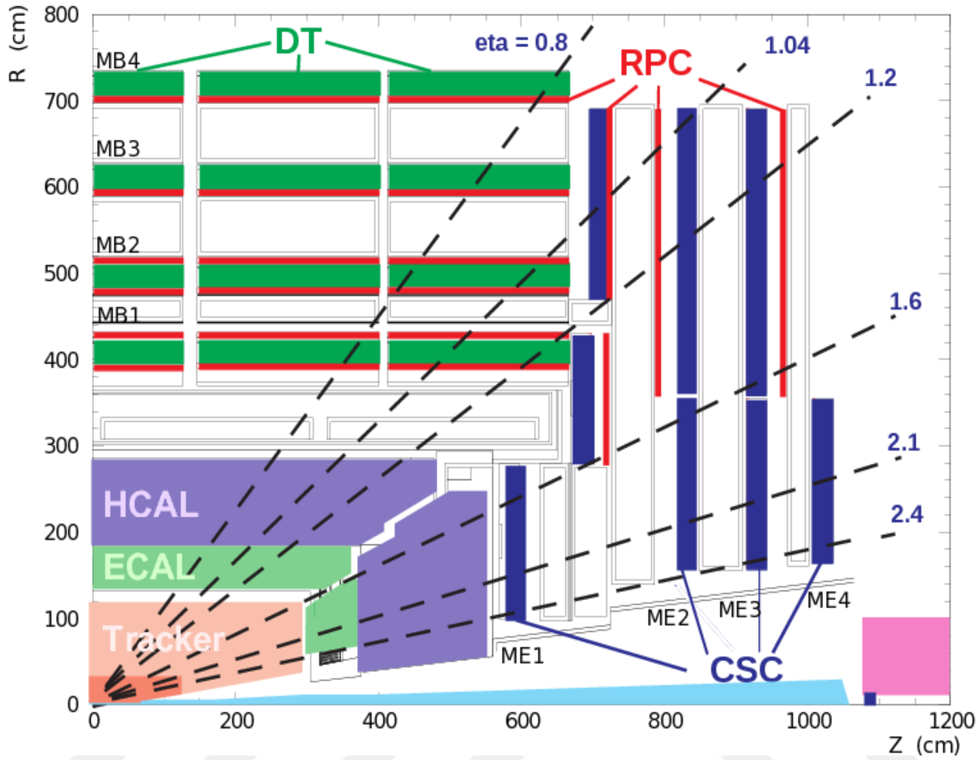

Figure 3.14. CMS Muon System (Bayatian G. L. et al., 2006)

The muon system of the CMS is composed three kind of detector located inside the empty volume of iron return yoke. These three detectors have three different technologies. It can be summarized these detectors follow:

- Drift Tubes (DT) in the barrel region where the muon rate is low and the 4-T magnetic field is uniform and mostly contained in the steel yoke. The barrel drift tube chambers cover the pseudorapidity range $|\eta| < 1.2$.
- Cathode Strip Chambers (CSC) in the endcap region where the muon rates are high and the magnetic field is large and non-uniform. The CSC is used in the endcap region because of their fast response, fine segmentation and radiation resistance. And these regions cover the pseudorapidity range $0.9 < |\eta| < 2.4$.

- And last detector type is Resistive Plate Chambers (RPCs) in the both barrel and endcap region. The RPCs have a very fast time response, comparable in fact to scintillators. The RPCs can be sufficiently highly segmented to make it possible not only to measure transverse momentum but to do it at trigger time (Chatrchyan S.,et al., 2008)

3.2.7 Forward Detectors

Forward physics at LHC is important due to particles produced at very small polar angles. The maximum possible rapidity at LHC is $y_{max} = \ln(\sqrt{s}/m_{\pi}) \approx 11.5$ hence the CMS detector includes several subdetectors. These detectors are CASTOR (Centauro and Strange Object Research) detector and ZDC (Zero Degree Calorimeter) detector. Both of them are sampling detector. Meaning of sampling is that they are made of repeating layers of dense absorber and tiles of scintillators (Volyanskyy, 2010).

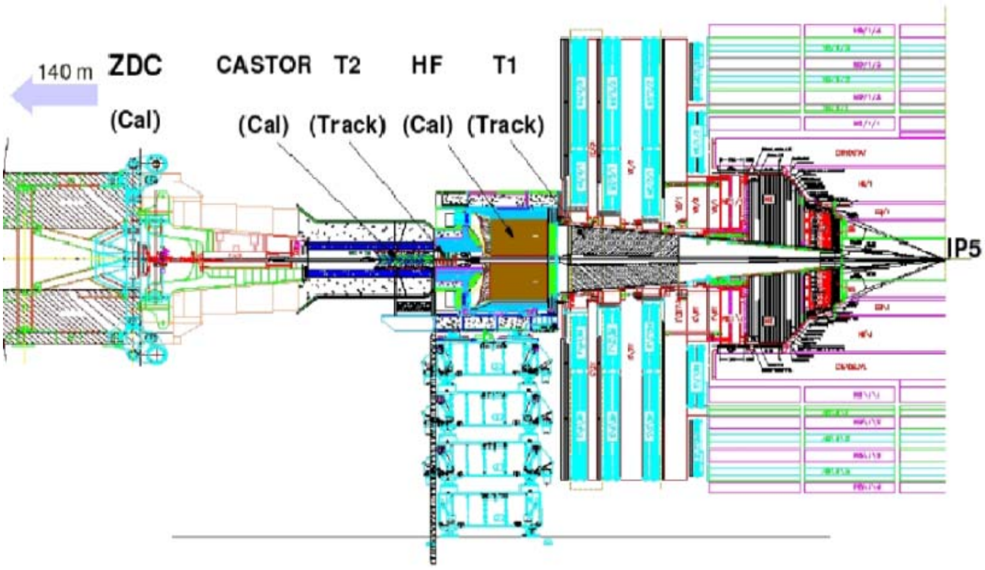

Figure 3.15. The Forward detectors in CMS (Chatrchyan S.,et al., 2008)

3.2.7.1 CASTOR Detector

The CASTOR detector being a Cerenkov-based sampling calorimeter similar in concept to the HF and covering the pseudorapidity range $-6.6 < \eta < -5.2$, which is placed at a distance of 14.4 m from the interaction point. The tungsten plates are used as absorber and fused silica quartz plates as active medium in the CASTOR detector, since the plates provides the smallest possible shower size. The plates are inclined by 45 degree to efficiently capture the Cerenkov light produced by relativistic charged particles passing through the quartz emit Cerenkov photons (Volyanskyy, 2010).

The compact calorimeter CASTOR with the physical size of about 65 cm x 36 cm x 150 cm is embedded into a skeleton (constructed) made of stainless steel. The CASTOR detector consists of 14 longitudinal modules. Each of these modules comprises 16 azimuthal sectors organized in two half calorimeters. First 2 modules constitute the electromagnetic section. The thicknesses of tungsten and quartz plates are 5.0 and 2.0 mm in the electromagnetic section respectively. The other 12 modules constitute the hadronic section. The thicknesses of plates in hadronic section are 10 mm for tungsten and 4.0 mm for quartz plates (Chatrchyan S.,et al., 2008).

3.2.7.2 ZDC Detector

The ZDC (Zero Degree Calorimeter) is a sampling calorimeter with pseudorapidity coverage of $|\eta| \geq 8.3$. The ZDC at the CMS very forward region are located inside the TAN absorbers being of 1 m length, 96 mm width and 607 mm height the neutral particle absorber at the distance of 140 m on both sides from the interaction point. The quartz fibers as the active material and the tungsten plates as an absorber material is used in this Cerenkov sampling calorimeters. The goal of ZDC design is that to measure neutrons and very forward photons providing detection. The design of ZDC includes two independent parts: the electromagnetic (EM) and hadronic (HAD) sections (Chatrchyan S.,et al., 2008).

3.3 Trigger System

The p-p and heavy-ion collisions at the LHC give rise to the unpresented high luminosity and instruction rates. And this high luminosity results in a rate of 40 MHz The CMS trigger system is used to cope with these situations. In order to solve these problems, selecting rare events, supressing background as effectively as possible, the CMS is using two trigger levels called Level1 (L1) and High Level Trigger (HLT). In this context, these triggers are very important tools to store the information coming from all sub-detectors.

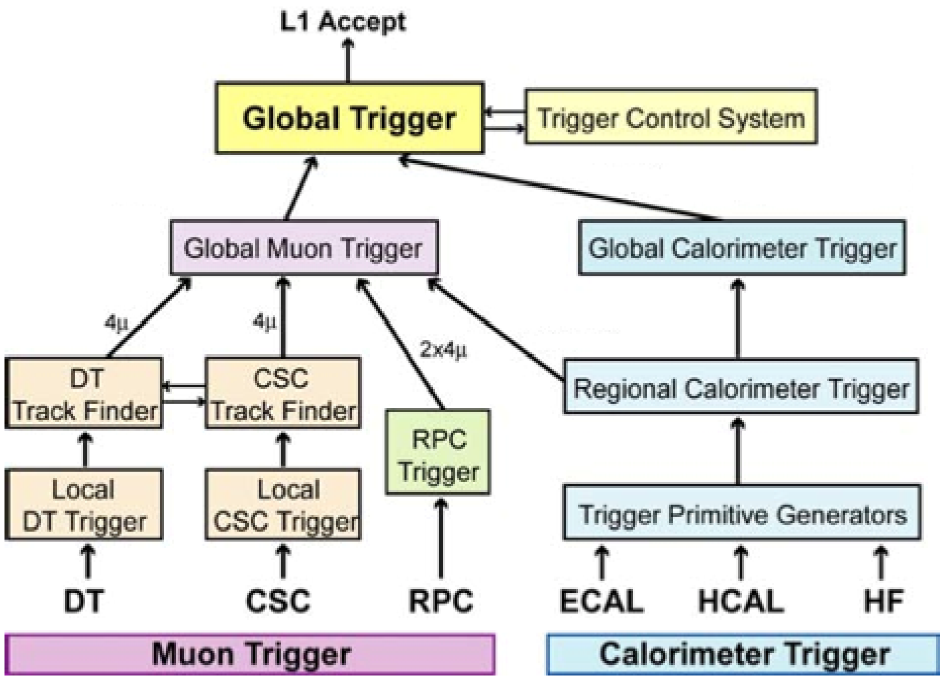

Figure 3.16. Trigger System (Bayatian G.L., et al., 2000)

The L1 trigger based on programmable electronics is located in two places: the experimental cavern UXC55 and the auxiliary service cavern USC55 where CMS detector region under the ground. The L1 trigger system is divided into three subsystems, which are the L1 calorimeter trigger, the L1 muon trigger and the L1 global trigger. The stored energies left by electrons, muons, taus and jets in the ECAL, HCAL and HF calorimeter cells are used to build decision in the L1 calorimeter trigger. Also, the muon trigger is divided into three different muon detector systems as the Drift Tube (DT) trigger, the Cathode Strip Chamber (CSC) trigger and the Resistive Plate Chamber (RPC) trigger. On the other hand, the L1 muon trigger includes the global trigger. The trigger information coming from the DT, CSC and RPC trigger systems combine the global muon trigger, which sends the information to the L1 global trigger.

The L1 trigger system must be able to accept a new event every 25 ns because of the time between beam crossings at the LHC. This time is too short to read out the data for every event. But anyways, every process in the trigger must be repeated every 25 ns. The design output rate of L1 trigger is 100 kHz. This rate for L1 corresponds to a minimum rejection rate of 10^4 at the nominal LHC design luminosity of 10^{34} $cm^{-2}s^{-1}$.

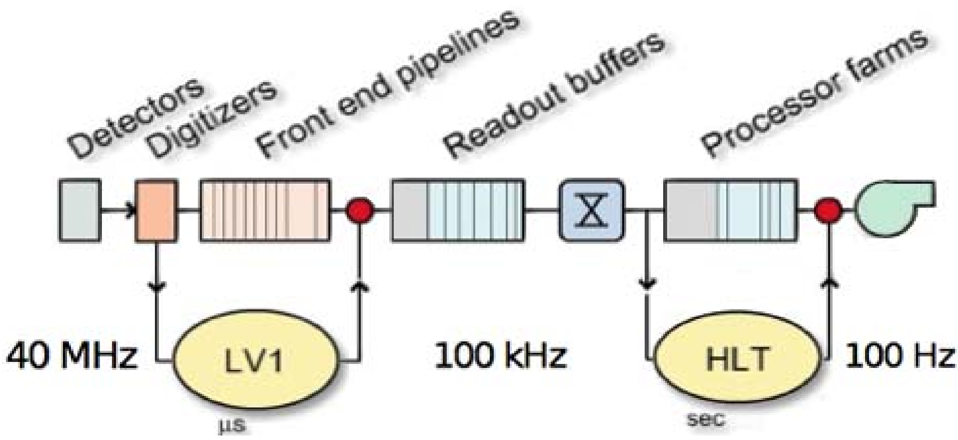

Figure 3.17. Trigger Rate (Bayatian G.L., et al., 2000)

The HLT being a software system in the CMS reduces the rate of data corresponding to the selected events passing the L1 trigger to about 1 kHz or less. The HLT triggers have a permission to take all information from L1 trigger.

Consequently, HLT can make other topological calculations on digital list of objects. Event selection process is performed in order to optimize the data flow by using a series of HLT filters. The HLTs use the full event data for the decision to keep an event. Finally, The HLTs send the events selected by filters farm in HLT to Storage Manager system (Bayatian G.L., et al., 2000).

3.4 Data Acquisition

The DAQ (Data Acquisition) in the CMS experiment plays an essential role because of the rates of the collision and the overall data. These rates are much higher than the rate at which one can write data to mass storage (the rate of the data writing to mass storage). At the design luminosity and bunch crossing frequency of 40 MHz of LHC, each crossing result in around 20 inelastic p-p events producing approximately 1 MB of zero-suppressed data in the CMS read out system. The L1 trigger is designed to reduce the rate of events to 100 kHz. After that The HLT reduce this L1 rate of 100 kHz to a final output rate of 100 Hz.

The main purpose of DAQ system is to read the CMS detector information for the selected events by the L1 trigger and to select the most interesting events for output to mass storage. Also, the CMS DAQ system perform the readout of the front-end electronics after a L1 accept. Another crucial function of DAQ system is the operation of Detector Control System (DCS) for the operation and supervision of all detector components and general infrastructure of experiment. The DCS is a key element for the operation of CMS, and guarantees its safe operation to obtain high-quality physics data (CMS Collaboration, 2002).

4 MEASUREMENT OF ENERGY DENSITY

In this chapter, a measurement of energy density and transverse energy density are presented in p-p collisions at LHC for center-of-mass energy of $\sqrt{s}$ =13 TeV. The data used in this analysis have been recorded by the CMS in 2015. The energy density and transverse energy density measurements are performed as a function of pseudorapidity in HF and CASTOR regions. The results from analysis are compared to the different model predictions produced MC event generator (that describe high-energy hadronic interactions). A further comparison to earlier p-p collisions data at $\sqrt{s}$=900 GeV and $\sqrt{s}$=7 TeV allows to test the hypothesis of limiting fragmentation. This hypothesis suggested nearly four decades ago inform that the produced particles, in rest frame of one of the colliding hadrons, will approach a limiting distribution. The distribution describes the momentum distribution of the fragments of the other hadron.

4.1 Physics Motivation

In 2015, protons in LHC circle collided at the centre-of-mass energy of $\sqrt{s}$=13 TeV. LHC allows new discussions and physics through this operation called Run2. In this process, determining the average energy per event (energy density) in specific angular regions is important. The measurement of the energy density in forward region is directly sensitive to the ISR and MPI. Further, the measurement of the energy density can provide some input to determination of parameters in MPI models, can discriminate between different MPI models. Moreover, the measurement is performed for various event types (soft-inclusive-inelastic, non-single-diffractive enhanced, single-diffractive enhanced events) to investigate MPI effects in high-energy p-p collisions.

In this study, beam fragmentation is also studied at the regions close to beam rapidities. The studies of the beam fragmentation supply some important input for the MC model tuning. The results at different center-of-mass energy are compared using the shifted pseudorapidity which is obtained with the beam rapidity $y_{beam} = \cosh^{-1}\left(\frac{\sqrt{s}}{2m_p}\right)$. The shifted pseudorapidity can be written as $\eta^{'} = \eta\text{-}y_{beam}$.

In this section, a measurement of energy density covering a pseudorapidity range of $3.15 < |\eta| < 5.20$ and $-6.6 < \eta < -5.2$ is presented. Also, the previous measurement that have been performed at lower center-of-mass energies by ATLAS (ATLAS Collaboration, 2012), LHCb (LHCb Collaboration, 2013) and CMS (CMS Collaboration, 2011) collaborations are used for the comparison. The average energy density per event is defined in Equation 4.1 as:

$$\frac{dE}{d\eta} = \frac{1}{N_{evt}} \sum_i E_i \frac{c(\eta)}{\Delta\eta} \qquad (4.1.)$$

where N_{evt} defines the selected events after the noise and pile-up (PU) contributions have been corrected, $\sum_i E_i$ shows the summed energy of all calorimeters towers within a bin of pseudorapidity having a width $\Delta\eta$. $c(\eta)$ is the η-dependent conversion factor from the calorimeter measurements.

4.2 MC sets used in Analysis

In this analysis, different MC samples are used to compared prediction from a theory with the final corrected results. The MC samples that were generated for 0 T and 3.8 T are used in the present analysis are given in Table 4.1 and Table 4.2, respectively CMSSW release version and Global Tag are indicated in the names of datasets.

General purpose event generator, PYTHIA 8 (version8.212) was used with different tunes like MONASH 2013 (P. Skands, 2014), CUETP8M1 (CMS Collaboration, 2016), CUETP8S1 (CMS Collaboration, 2016) and MBR model

(Goulianos, 2013) which is used together with 4C (R. Corke and T. Sjostrand, 2011) and CUETP8M1. The parameters in these tunes are set to define the measurement of the UE at Tevatron and LHC. The tunes providing a different description of UE are built using different PDF) sets (NNPDF2.3 LO (NNPDF Collaboration, 2013) and CTEQ6L1 (J. Pumplin et al, 2002).

Table 4.1. The MC Samples which were generated at B = 0 T (i.e., Magnet OFF) Used in The Present Analysis

MinBias_TuneMonash13_13TeV-pythia8/RunIISpiring15DR74 NoPU0TRawReco magnetOff MCRUN2740TV0_v1/GEN-SIM-RECO
MinBias_TuneMBR_13TeV-pythia8/RunIISpiring15DR74-NoPU0TRawReco_magnetOff_MCRUN2740TV0_v1/GEN-SIM-RECO
ReggeGribovPartonMC_13TeV-EPOS/RunIISpiring15DR74-NoPU0TRawReco_magnetOff_MCRUN2740TV0_v1/GEN-SIM-RECO
ReggeGribovPartonMC_13TeV-QGSJetII/RunIISpiring15DR74-NoPU0TRawReco_magnetOff_MCRUN2740TV0_v1/GEN-SIM-RECO

Table 4.2. The MC Samples which were generated at B = 3.8 T (i.e., Magnet ON) Used in The Present Analysis

/MinBias TuneMonash13 13TeV-pythia8/hvanhaev-RunIISpring15DR74-NoPU castor MCRUN2 74 V8-v1- 63052cce62044e1bf5327c7faa65 4082/USER
/MinBias TuneMBR 13TeV-pythia8/RunIISpring15DR74-NoPURawReco castor MCRUN2 74 V8B-v1/GEN-SIM-RECO
/MinBias TuneEE5C 13TeV-herwigpp/RunIISpring15DR74-NoPURawReco castor MCRUN2 74 V8B-v1/GEN-SIM-RECO
/ReggeGribovPartonMC 13TeV-EPOS/RunIISpring15DR74-NoPURawReco castor MCRUN2 74 V8B-v1/GEN-SIM-RECO
/ReggeGribovPartonMC 13TeV-QGSJetII/RunIISpring15DR74-NoPURawReco castor MCRUN2 74 V8B-v1/GEN-SIM-RECO

Based on the Gribov's Reggeon approach, the EPOS-LHC (version 1.99) and QGSJETII.4 are used to describe the extensive air shower that high-energy cosmic rays are caused to. Hence soft physics is important. A combination of Gribov-Regge multiple scattering, perturbative QCD and string fragmentation are the corner stones for the both models.

4.3 Data and Event Selection Strategy

The measurement of the energy density is performed using data selected online in an unbiased way by triggering data acquisition system (Beam Pick-up-Timing for the eXperiments – BPTX device). Moreover, data with 0.06 nb^{-1} of integrated luminosity was collected without magnetic field (B=0T) through the CMS detector in 2015 with a small PU value is of 5%. Meaning of small PU is the collected data has relatively low average number of p-p interactions per bunch crossing.

In this analysis, three different data samples are used to understand the effect of PU and magnetic field. These samples are summarized in Table 4.3. Run 247324 and Run 247920 referred to "LHCf runs" has no magnetic field (B=0T) although Run 255019 referred to "Vdm runs" has a magnetic field of 3.8 T. The PU value of these samples is 5% for Run 247324, 30 % for Run 247920 and 50% for Run 255019.

Table 4.3. Summary of runs at B = 0T and B = 3.8 T used in the analysis

Run	Approx. PU	Initial lumi Section	Effective luminosity
***B* = 0 T**			
247324	5%	97-311	0.25 μb^{-1}
247920	30%	1-771	16.27 μb^{-1}
***B* =3.8 T**			
255029	50%	40-422	17.31 μb^{-1}

All data handled by using CMSSW release 7_4_14 with global tag 74X_dataRun2_v2 are updated HCAL conditions (HcalRespCorrs_v5.0_offline). Furthermore, these conditions include some calibrations and bad channel list of CASTOR detector (P. V. Mechelen et al. , 2015). The data were triggered by ZeroBias trigger which is a totally inclusive trigger and corresponds to a random read out from the detector.

The events used in this analysis have been chosen by considering three different strategies for offline selection. These three different selections are defined as follows:

- An inclusive inelastic (INEL) selection allowing significant fraction of diffractive events.
- A non-single-diffractive-enhanced selection (NSD-Enhanced) where the contributions from single diffractive dissociation are suppressed.
- Single-diffractive-enhanced (SD-Enhanced) where the contributions from single-diffractive dissociation events are considered.

These different selections are achieved by using the energy deposit of HF calorimeter above noise level. INEL event selection refers to activity on at least one side of HF calorimeter while NSD-Enhanced selection require an activity on both side of HF calorimeter. Lastly SD-Enhanced selection require an activity in exactly one side of HF calorimeter and the veto condition must be applied to other side. Figure 4.1 shows the illustration of event selection criteria for INEL, NSD-Enhanced and SD-Enhanced. The activity in HF means here corresponds a reconstructed calorimeter tower with energy above evaluated value of energy thresholds which are obtained from a study of events without beam. These energy threshold value provides an effective reduction on the contribution from the detector noise. Figure 4.2 gives the measured distribution with noise distribution obtained from data without the presence of LHC beams and simulated events.

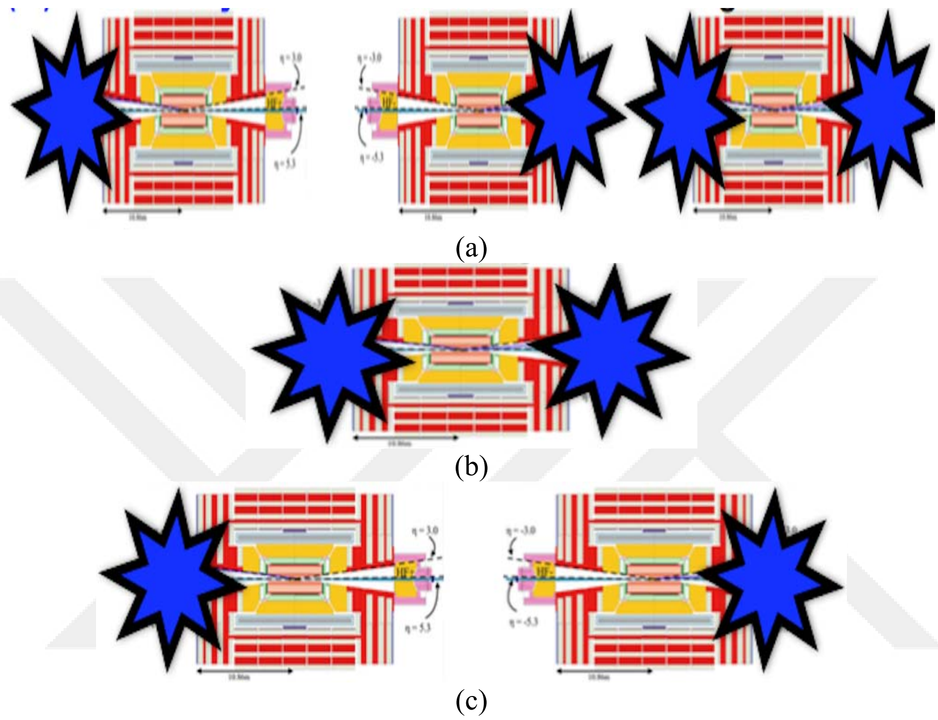

Figure 4.1. Event selection strategies (a) INEL selection (b) NSD-Enhanced event selection (c) SD-Enhanced event selection

In Figure 4.2, E_{HF^-} represents the highest energy in negative pseudorapidity region while E_{HF^+} corresponds to the highest energy in positive side for HF calorimeter. From the distribution in Figure 4.2, an energy threshold of $E_{threshold} = 5$ GeV is defined as the optimal threshold value to avoid the influence of the detector noise and used for all event selection. Due to the fact that the interaction possibility of collision data is about 5%, the noise peaks in data contain inevitably more events than in simulations because the simulation samples are generated without PU. In addition, the detector noise distribution obtained from empty-beam data (without beam) are overlaid as shaded areas.

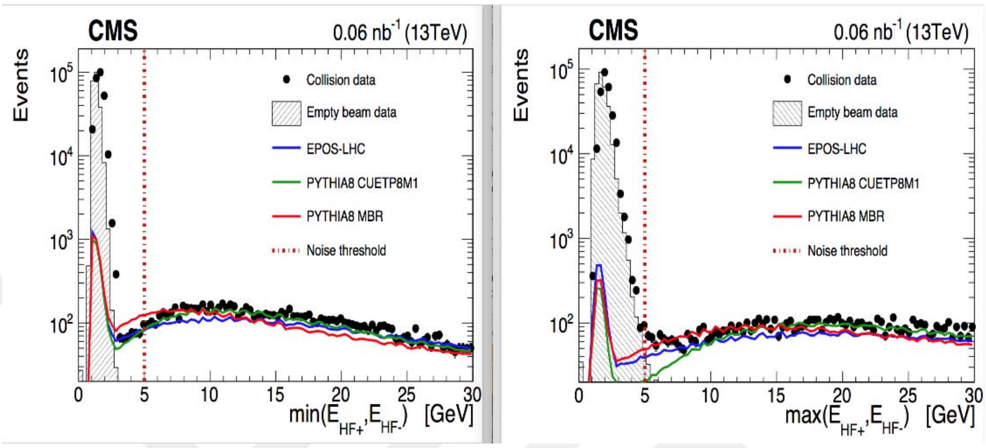

Figure 4.2. The number of the events distribution as a function of the tower energy. The left plot gives the smaller of the two HF calorimeter energies and the right plot gives the higher of the two HF calorimeter energies. The simulations are represented by lines the markers shows the data. The shaded areas correspond to measured detector noise.

The cluster of the stable final-state particles is split on two systems by using the largest rapidity gap in the event. These systems are called *X* and *Y*. All particles at negative side constitute the *X* system while all particles at positive side represent the *Y* system. In Equation 4.2, the invariant masses in the *X* and *Y* system, M_x and M_y, are calculated using the four momenta of the individual particles. The ratio of the invariant mass to the centre-of-mass energy is described as ξ_x and ξ_y

$$\xi_x = \frac{M_x^2}{s}, \qquad \xi_y = \frac{M_y^2}{s} \tag{4.2.}$$

ξ is determined by the way of looking on the maximum value between ξ_x and ξ_y ($\xi = \max(\xi_x, \xi_y)$). Within the simulations produced via the MC event generators, at the stable particle level (i.e for particles with proper decay length $c\tau > 1$ cm), the soft-INEL events are selected through the $\xi > 10^{-6}$ condition. NSD-Enhanced events at the stable particle level are selected by using a requirement of at least one stable particle (either charged or neutral) within the pseudorapidity acceptance of the HF calorimeters $3.15 < |\eta| < 5.2$ on both side of the interaction point. At the stable particle level SD events are selected by the presence at least one stable particle with energy $E > 5$ GeV with in the pseudorapidity range $3.15 < |\eta| < 5.2$ on one side and the other side must be devoid of the particles with energy $E > 5$ GeV. In Table 4.4, phase space definitions are given for INEL, NSD-Enhanced and SD-Enhanced event selections. The last row of Table 4.4 is reserved for the event selection criteria needed for the limiting fragmentation study.

Table 4.4. Summary of event selections used for the different event categories in data at detector level and in simulations at the stable-particle level.

Class	Detector Level	Stable-Particle Level
INEL	$E_{HF+} > 5$ GeV or $E_{HF-} > 5$ GeV	$\xi > 10^{-6}$
NSD-Enhanced	$E_{HF+} > 5$ GeV and $E_{HF-} > 5$ GeV	At least one stable particle with $E > 5$ GeV in HF region (both side)
SD-Enhanced	$E_{HF+} > 5$ GeV $E_{HF-} < 5$ GeV or $E_{HF+} < 5$ GeV or $E_{HF-} > 5$ GeV	At least one stable particle with $E > 5$ GeV in one side of HF, vetoing particles $E > 5$ GeV on other side
Limiting Fragmentation Study	$E_{HF+} > 4$ GeV and $E_{HF-} > 4$ GeV	One stable particle in $3.9 < |\eta| < 4.4$

4.4 Calculation of Corrected Events, Noise and Pile up

As stressed before the determination of quantities in Equation 4.1, N_{evt} and $\sum_i E_i$, is important to measure the energy density. The number of selected events, N_{sel}, is corrected by subtracting the noise contribution and the corrected number of events, N_{corr} is obtained with events containing only signal. Events triggered by zerobias (unbiased) trigger are denoted by N_{ZB}, while events triggered by empty bunch trigger are denoted by N_{EB}. The fraction of such offline-selected events is indicated by f_{ZB} and f_{EB}. In this case, the number of selected collision events can be defined as $N_{sel} = N_{ZB} f_{ZB}$ and number of noise events correspond to $N_{noise} = N_{ZB} f_{EB}$. The latter contains $N_{sig+noise} = N_{corr} f_{EB}$ events that are selected because towers in the same events are above threshold signal and noise fluctuations. Hence, the corrected number of events is given as

$$N_{corr} = N_{sel} \text{-} N_{noise} + N_{sig+noise} = \frac{N_{ZB}(f_{ZB} \text{-} f_{EB})}{1 - f_{EB}} = N_{ZB} f_{ZB} p \qquad (4.3.)$$

where the purity is defined as $p = (1 - f_{EB}/f_{ZB})/(1 - f_{EB})$. In this analysis, the purity of the data is calculated as 99%. And also, the contribution of noise depends weakly on event selection criteria.

The reconstructed number of events is also corrected for PU effect. The Poisson distribution, $(n, \lambda) = \lambda^n e^{-\lambda}/n!$, with an average value (λ) is suitable to define the number of p-p interactions in each bunch-crossing (n). In this case, $e^{-\lambda} = 1 - N_{corr}/N_{ZB}$ defines the probability of no interaction and this means λ

can be calculated from inelastic collision in data. By using the value of the f_{EB}, $\lambda =$ - $\ln(1 - f_{ZB}p)$ is determined from the INEL event selection.

The number of visible collision in N_{tot} bunch crossing is given as $N_{coll} = N_{tot}\epsilon \sum_{i=0}^{n} nPois(n;\lambda) = N_{tot}\epsilon\lambda$ where the probability for each collision to be observed and selected is denoted by ϵ. The probability of observed events with n simultaneous collision is an important quantity for PU and given by $\epsilon_n = 1 - (1 - \epsilon)^n$. The average number of actually observed events is given as $N_{obs} = N_{tot} \sum_{n=0}^{\infty} \epsilon_n \, Pois(n;\lambda)$. In this case, the PU correction factor is given as

$$f_{PU} = \frac{N_{coll}}{N_{obs}} = \epsilon\lambda \left(\sum_{n=0}^{\infty} \epsilon_n Pois(n;\lambda) \right)^{-1} \quad (4.4.)$$

The corrected number of collisions are used for counting inelastic events in Equation 4.1 and it is given by $N_{evt} = N_{coll} = N_{ZB} f_{ZB} p f_{PU}$. In general, the event selection strategy has an effect on the impact of PU. Especially the exclusivity criteria in SD-Enhanced selection causes less selected events in presence of the more number of simultaneous collisions. The number of SD-Enhanced events can be calculated by using the formula $N_{SD} = 2N_{INEL}$-$N_{HF\text{-}}$-N_{HF+} where N_{INEL} indicates the correct number of inelastic collisions, $N_{HF\text{-}}$ and N_{HF+} indicates the corrected number of events negative and positive side of HF respectively. Likewise, the number of NSD-Enhanced events is calculated by using $N_{NSD} = N_{HF\text{-}}N_{HF+}$-$N_{INEL}$. The results from all these calculations are summarized in Table 4.5.

Table 4.5. Selection factor and purities for various event selection categories. The last two rows are derived using the formulae in the text. The porbability ϵ to select a single collision is determined from simulations, and the value quated here is the avarage value from al levent generators, with a maximal model dependence of 2%. The rightmost column quantifies the combined correction due to noise and pileup. All statistical uncertainties are negligible.

	f_{ZB}	f_{EB}	p	$\epsilon\ (MC)$	f_{PU}	$p\ f_{PU}$
INEL	0.0490	0.0005	0.9902	0.9051	1.0250	1.0149
HF+	0.0442	0.0003	0.9935	0.8224	1.0227	1.0161
HF-	0.0439	0.0002	0.9956	0.8232	1.0228	1.0183
NSD-Enhanced	----	----	----	----	----	1.0044
SD-Enhanced	----	----	----	----	----	0.9804

Run 247920 is selected to compare with the low PU (5%) data (247324) to study the PU effect. The energy density distribution for INEL (soft-inclusive-inelastic) events selection after PU correction is shown in Figure 4.3 (left hand side) while the PU uncorrected state for same distribution is shown in Figure 4.3 (right hand side). In the same figure, it can be seen that (botton) the ratio distribution of what both state of PU corrected and state of PU uncorrected for Run 247324. The ratio of two states is flat and no significant change is observed between bins. For this reason, it can be said that the PU effect does not depend on η and can be neglected. Since the ratio distribution is close to 1, the uncertainty is $< 1\%$. This proves that PU correction technique works well. As it can be seen from Figure 4.3 (bottom) there is approximately 1% of PU effect for run 247324 datasets.

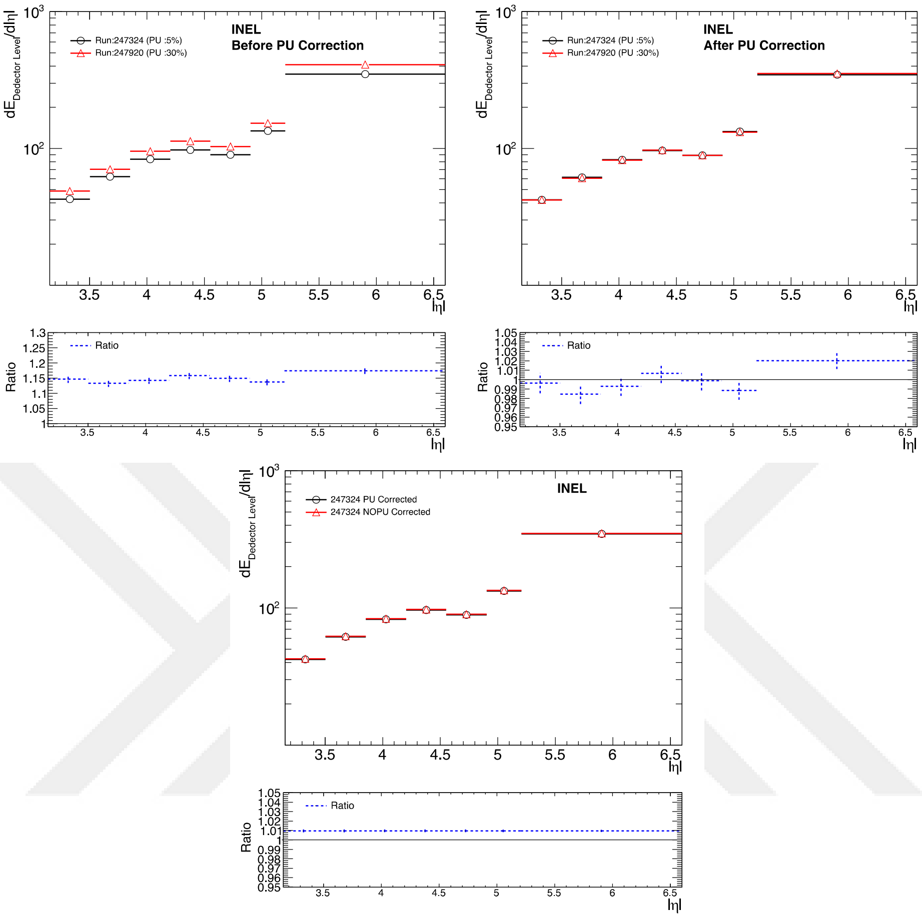

Figure 4.3. Energy density distributions of Run 247324, has PU of 5% and Run 247920, has PU of 30% before (upper left) and after PU correction (upper right) with ratio of Run 247324 to Run 247920. Lower plots shows the energy density distribution before and after PU correction for Run 247324.

4.5 The Effect of Magnetic Field

In this analysis, a comparison between data which has been taken with and without magnetic field is studied to understand effect of the magnetic field on the measurement. As mentioned before, Run247920 with high PU was selected to compare with the low PU data. Figure 4.4 show a comparison of data for INEL events to some various MC simulation such as PYTHIA 8 tune with MBR (upper left), EPOS-LHC (upper right) and QGSJetII.4 (bottom plot). Data 0T in Figure 4.4 represents to data collected by CMS with magnetic field OFF while Data 3.8 T corresponds to data with magnetic field ON. Similarly, all MC samples used for this comparison are shown in Figure 4.4 with and without magnetic field simulations. Bottom panel for each plot shows a ratio plot of magnet OFF to magnet ON for data and MC samples.

Considering the magnitude of the magnetic field, in the first bins the variation of MC simulations shows approximately 5% inconsistency while for the last bins the inconsistency is around 1%. For data, the inconsistency, between magnet ON and OFF is around 5% for the first bin and 1% for the rest. This inconsistency can be seen as a potential source of uncertainty for the data taken at full magnetic field. However, this source of uncertainty is not considered for the final result of this analysis because the data used in analysis was taken without magnetic field.

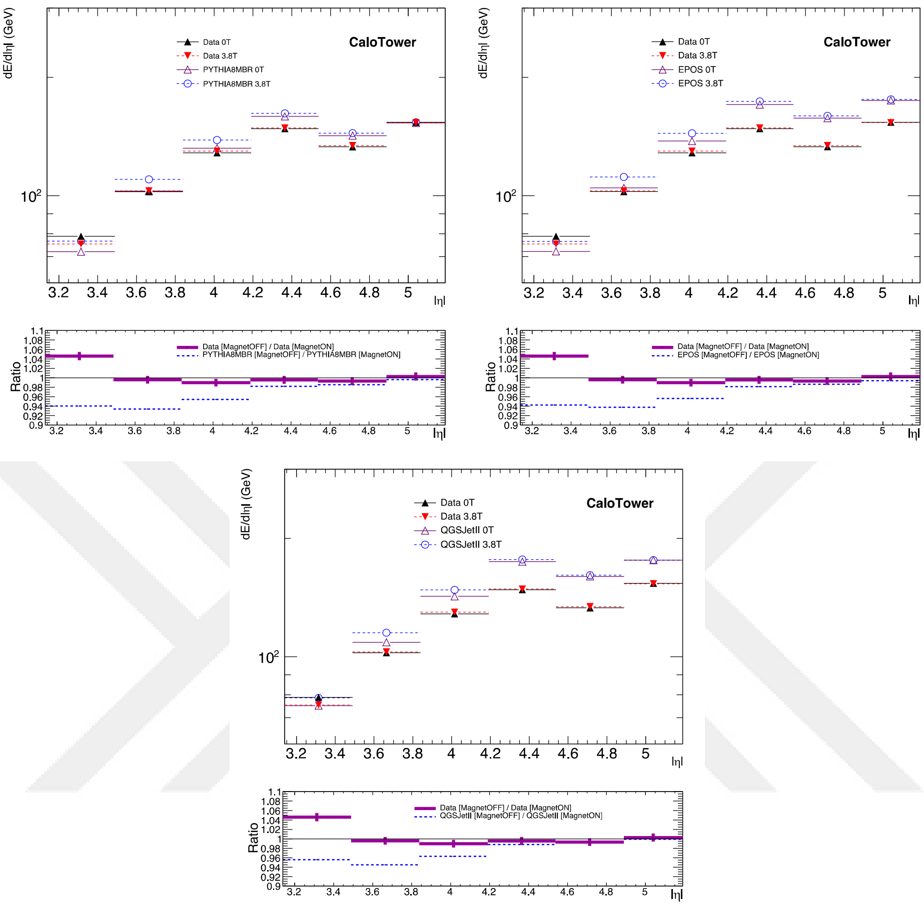

Figure 4.4. Energy density distributions of the data and PYTHIA8 4C+MBR (upper left), EPOS-LHC (upper right) and QGSJETII.4 (bottom) MC samples for the cases of magnetic field on and off for CaloTower. The bottom panels of each plot represent the ratios energy density with magnet OFF to the energy density with magnet ON.

4.6 Data and MC comparison at the Detector Level

Here in this chapter, the results acquired with the information of event selections used for the different event categories for data at detector level and for the simulations at the stable-particle level (INEL, NSD-Enhanced and SD-Enhanced) summarized in Table 4.4. The HF tower energy distributions are given in for INEL, NSD-Enhanced, SD-Enhanced data at $B = 0\,T$ in Figure 4.5, Figure 4.6 and Figure 4.7 respectively with the comparison of different MC generators (PYTHIA 8 tune MONASH, PYTHIA 8 tune 4C with MBR, EPOS-LHC, QGSJETII.4). All distributions in these figures are normalized by the total number of events in the related sample. As can be seen from the distributions, data and MC simulations deviate from each other at high values of tower energy except QGSJETII for all data sets.

The left-hand side plot in Figure 4.8 shows the comparison of energy density measurement at the detector level for MC simulations and INEL events at $B = 0\,T$. The ratio of the uncorrected data to MC predictions at detector level is given in the plot on the right-hand side of Figure 4.8. Likewise, the energy flow distributions of data and MC simulations at detector level for the other two selections which are NSD-Enhanced and SD-Enhanced are given in Figure 4.9 and Figure 4.10 respectively.

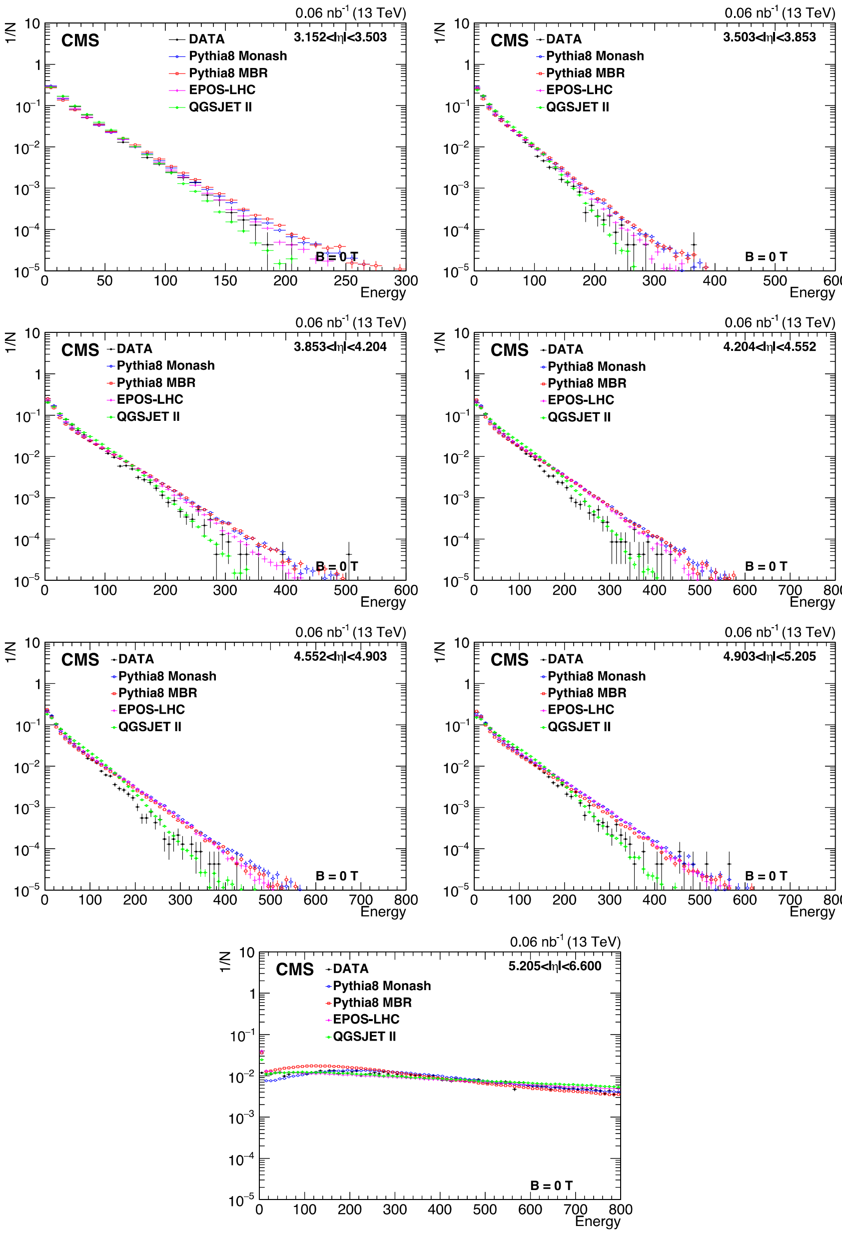

Figure 4.5. Comparison of the calorimeter tower energy distribution for soft-INEL selection for data with simulations from MC event generators. All distributions are normalized total number of events per sample

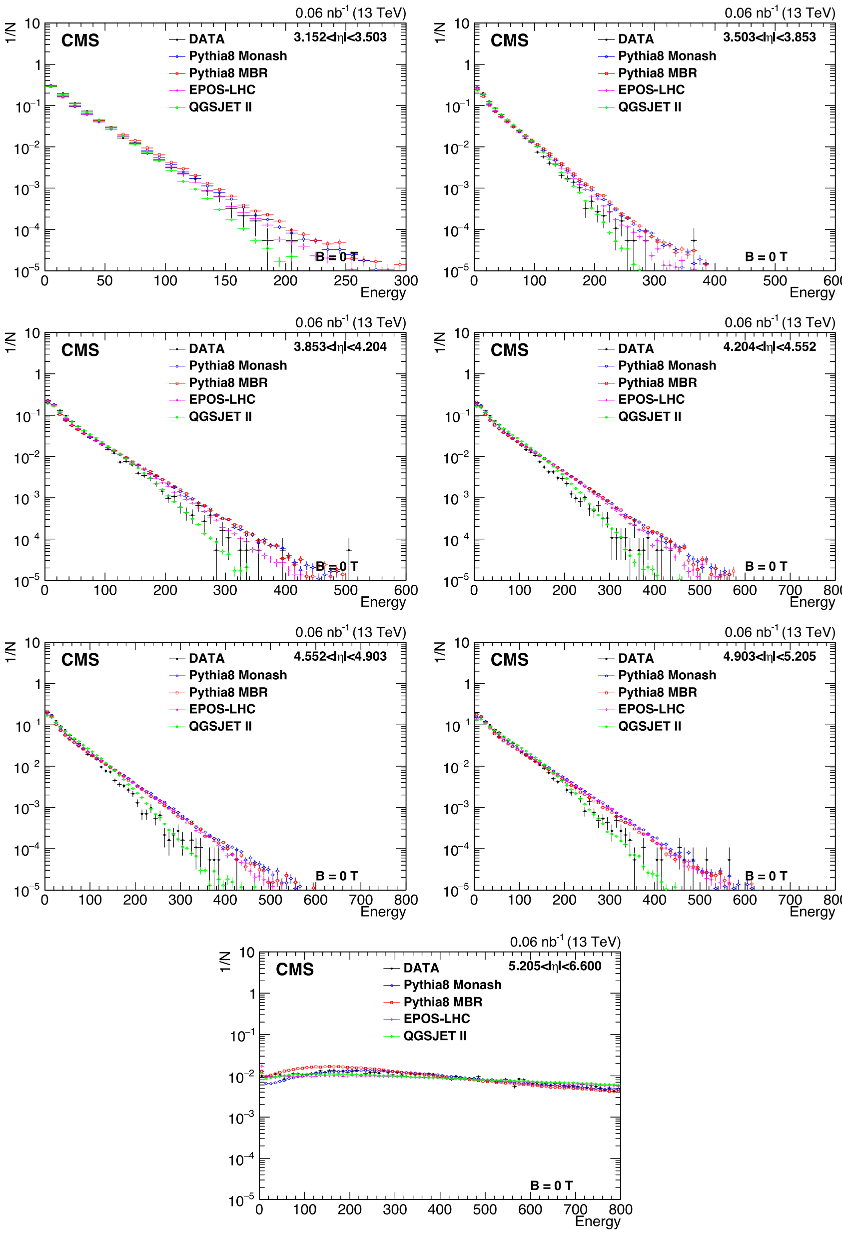

Figure 4.6. Comparison of the calorimeter tower energy distribution for NSD-Enhanced selection for data with simulations from MC event generators. All distributions are normalized total number of events per sample

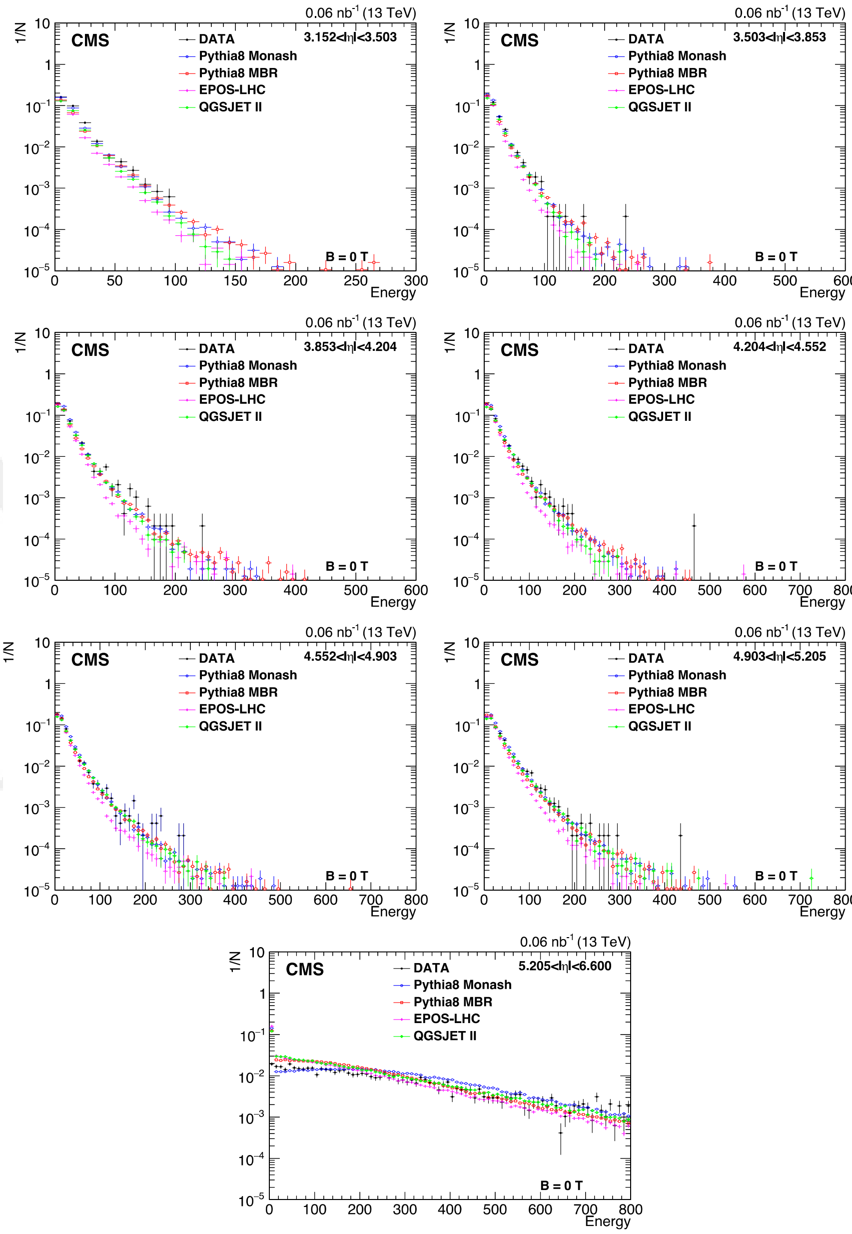

Figure 4.7. Comparison of the calorimeter tower energy distribution for SD-Enhanced selection for data with simulations from MC event generators. All distributions are normalized total number of events per sample.

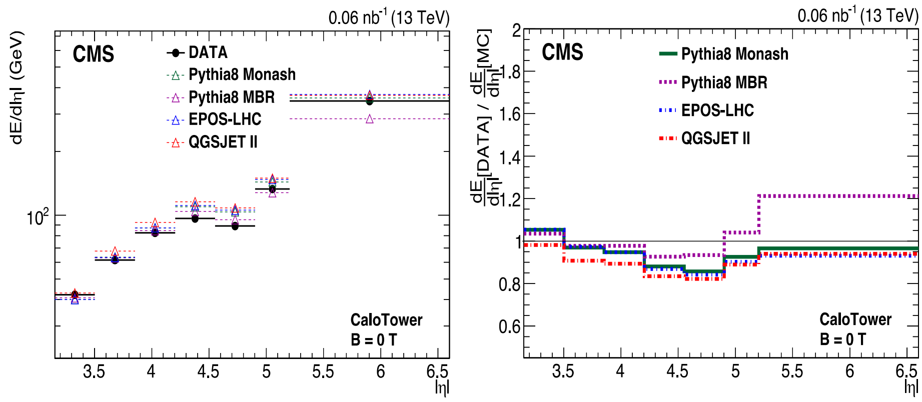

Figure 4.8. Left: Comparison of the measured energy flow (uncorrected data for soft-INEL selection) with simulations from MC event generators (PYTHIA8 MONASH13 and 4C+MBR tunes, EPOS-LHC and QGSJETII.4) at the detector level. Right: The ratio of the uncorrected data to the MC predictions at the detector level.

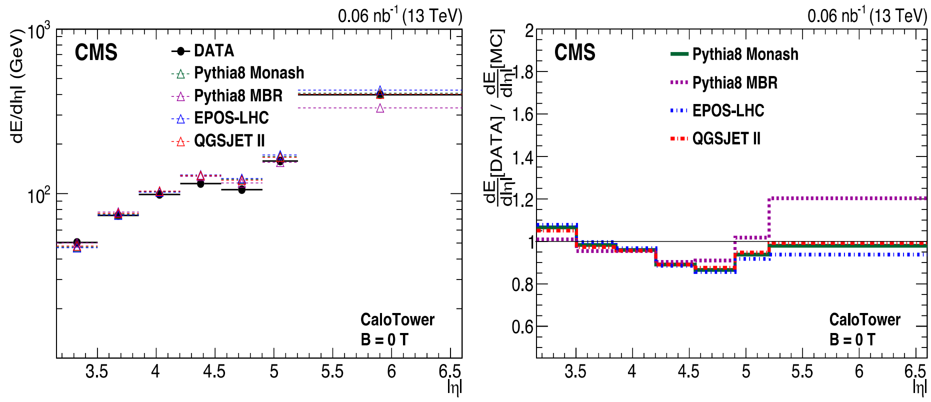

Figure 4.9. Left: Comparison of the measured energy flow (uncorrected data for NSD-Enhanced selection) with simulations from MC event generators (PYTHIA8 MONASH13 and 4C+MBR tunes, EPOS-LHC and QGSJETII.4) at the detector level. Right: The ratio of the uncorrected data to the MC predictions at the detector level.

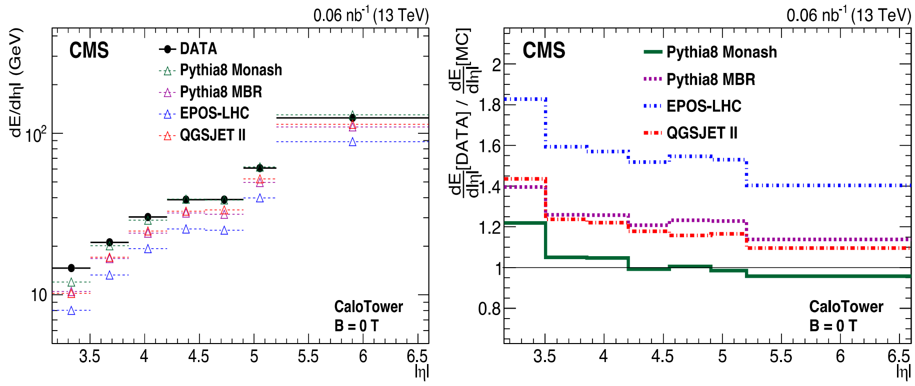

Figure 4.10. Left: Comparison of the measured energy flow (uncorrected data for SD-Enhanced selection) with simulations from MC event generators (PYTHIA8 MONASH13 and 4C+MBR tunes, EPOS-LHC and QGSJETII.4) at the detector level. Right: The ratio of the uncorrected data to the MC predictions at the detector level

4.7 Correction from Detector Level to Particle Level

The measured data used in this analysis is corrected to the stable-particle level by using the bin-by-bin correction factor which is evaluated from the ratios the predictions at the stable-particle level to the predictions at the detector level for every $|\eta|$ bins. These corrections are determined with the PYTHIA8 MONASH13, PYTHIA8 4C with MBR, EPOS-LHC and QGSJETII.4 MC generators together with a simulation of the CMS detector based on GEANT4. The final corrections are obtained by using the average of these four different simulated samples. The magnitude of final correction from the average of four different MC predictions changes from 1.5 to 2.5 depending on the $|\eta|$ value.

In this thesis, two method performed by previous CMS analysis efficiency, correction or bin-by-bin factors, are used as in previous similar CMS analyses (CMS Collaboration, 2011) (CMS Collaboration, 2013) (CMS Collaboration, 2015). Response matrices are decided to be used for procedure. During the analysis mean values for a set of energy spectra are measured, thus fluctuations would not be worth to consider. There is a dedicated analysis for CASTOR region (CMS

Collaboration, 2017a) is used for comparison of our results obtained with efficiency correction to their fully unfolded results. The large systematics on global calorimeter energy scales has the largest role on the uncertainties.

Leaks from one cell to the other cell are counted for the correction factors from the detector to the particle level provided by MC. However, there are some leaks which are compensated by other leaks in opposite direction. Because of the characteristic response of calorimeters and corrected event selection acceptance and inefficiency, no significant migrations and smearing effects are expected from this source.

Stable-particle and detector level energy density measurements at B = 0 T for the various MCs used within the analysis are given in Figure 4.11, Figure 4.12 and Figure 4.13. The bin-by-bin correction factor components are calculated considering Figure 4.11 for soft-INEL event selection, Figure 4.12 for NSD-Enhanced event selection and Figure 4.13 for SD-Enhanced event selection. Because of the large amount of dead material plus the crossing of the beam pipe, a bump appears for all event selections in the range of 4.55< $|\eta|$< 4.9. And additionally, on the HF border side, there's a leakage of the shower that reasons a bump inside the 4.9< $|\eta|$< 5.2 region. While there is a large discrepancy between different MC models at the detector level, the discrepancy of the correction factors is smaller. This case indicates that the magnitude of detector effects plays important role. These four different MC samples are used to obtain RMS and the envelope. Maximum variation of the correction factor, so model dependency may be evaluated as a systematic effect.

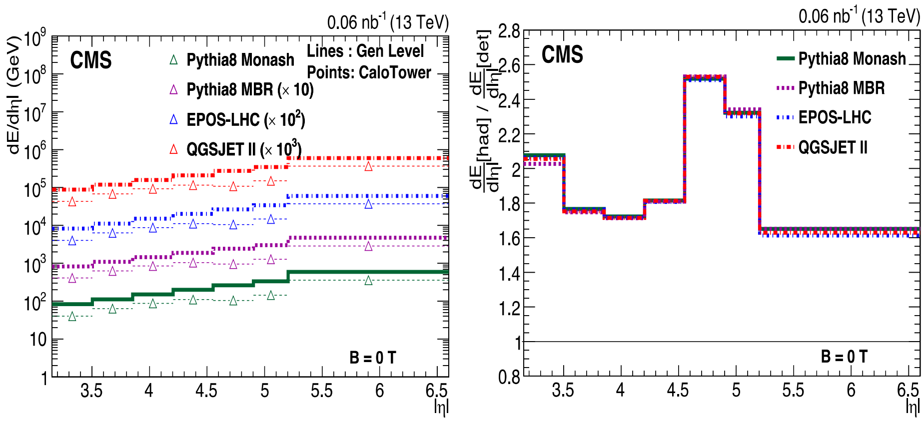

Figure 4.11. Left: Comparison of detector level (for soft-INEL selection) and particle level ($\xi > 10^{-6}$) for different MC samples. Points show the detector level results while lines corresponds to predictions obtained from different MC samples. Right: Ratio of detector level to particle level i.e bin-by-bin correction factor.

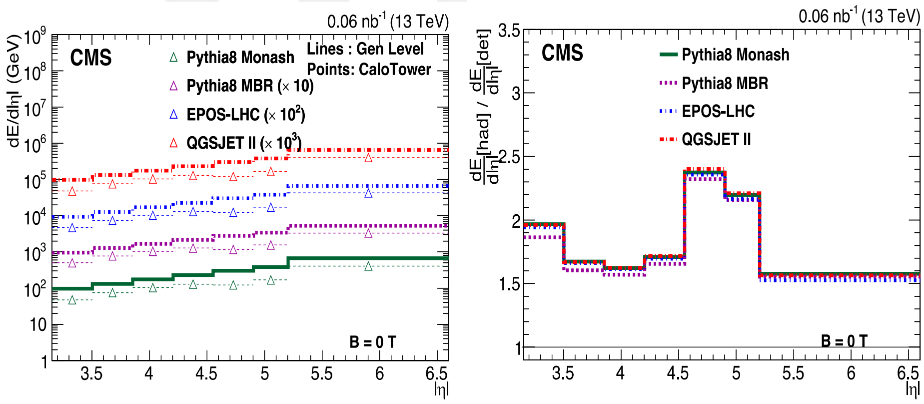

Figure 4.12. Left: Comparison of detector level (for NSD-Enhanced selection) and particle level for different MC samples. Points show the detector level results while lines corresponds to predictions obtained from different MC samples. Right: Ratio of detector level to particle level i.e bin-by-bin correction factor

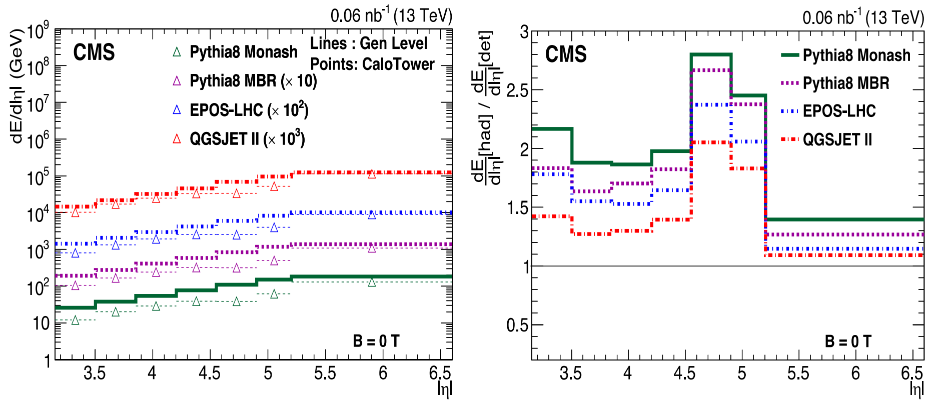

Figure 4.13. Left: Comparison of detector level (for SD-Enhanced selection) and particle level for different MC samples. Points show the detector level results while lines corresponds to predictions obtained from different MC samples. Right: Ratio of detector level to particle level i.e bin-by-bin correction factor.

4.8 Systematic Uncertainty

The uncertainty sources on the energy density measurement can be given as the energy scales for the HF and CASTOR calorimeters, the energy thresholds in calorimeter towers, the contribution of the noise and PU, the uncertainties on the event selections, the model dependency and statistical uncertainties. The uncertainty resulting from energy scale in HF and CASTOR calorimeter dominates the experimental uncertainty. For HF and CASTOR, the uncertainty from the energy scale have been estimated with an accuracy of 10% (CMS Collaboration, 2011) and 17% (V. Andreev et al., 2010) respectively.

The energy threshold value used in each event selection and energy sum of the calorimeter is increased by the uncertainty of HF energy scale (10%). In this way, the possible influence of remaining calorimeter noise on HF is better assessed. The energy flow obtained by increasing the threshold energy value is compared with the energy flow obtained from the nominal threshold energy value. After these evaluations, the uncertainty results from the energy threshold choosing 5 and 5.5 GeV are calculated as 0.7% for INEL, 0.01% for NSD and 5% for SD event selection. The resulting uncertainty is shown in Figure 4.14 for soft-INEL selection, Figure 4.15 for NSD-Enhanced selection and Figure 4.16 for SD-Enhanced selection. Furthermore, the threshold for tower energy sum is increased to study the influence of the energy threshold by using the energy scale uncertainty. This case leads to uncertainties of 1% for three event selections strategy. Figure 4.17, Figure 4.18 and Figure 4.19 show the uncertainty applied energy scale uncertainty of HF (10%) for INEL, NSD-Enhanced and SD-Enhanced respectively.

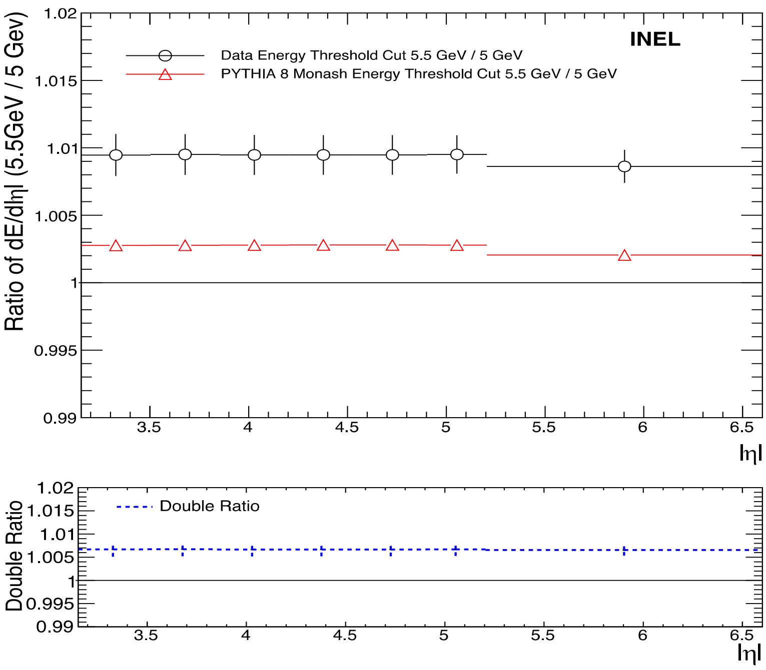

Figure 4.14. Variation of results in data and MC due to variation of the cut applied for selection of events for soft-INEL

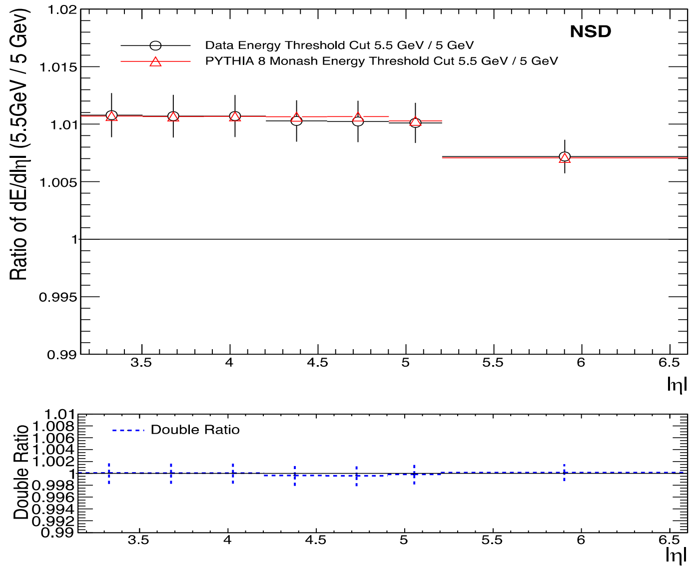

Figure 4.15. Variation of results in data and MC due to variation of the cut applied for selection of events for NSD-Enhanced events

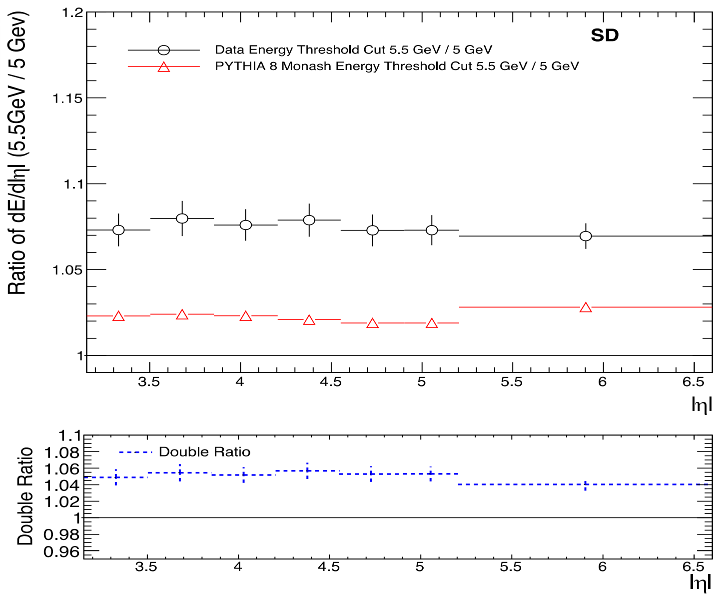

Figure 4.16. Variation of results in data and MC due to variation of the cut applied for selection of events for SD-Enhanced events.

The uncertainty from model dependency which is considered as systematic effect, is determined as lower than 3.5% for INEL and NSD (see Figure 4.11-right and Figure 4.12-right). For SD selection, it changes bin-by-bin from 16% to 37% (see Figure 4.13-right). The uncertainty from model dependency obtained by using different MC predictions (PYTHIA8 with MONASH and 4C+MBR tunes, EPOS-LHC, QGSJETII.4) is summarized in Table 4.6.

Table 4.6. The uncertainties in the energy density measurement for the three event selection categories. The results depend slightly on the pseudorapidity.

Source of uncertainty	INEL	NSD-Enhanced	SD-Enhanced
HF energy scale	10%	10%	10%
CASTOR energy scale	17%	17%	17%
Noise and pileup	$\approx 10^{-3}$	$\approx 10^{-3}$	$\approx 10^{-3}$
Event selection	0.7%	0.01%	0.5%
Energy threshold in calorimeter towers	1%	1%	1%
Model dependence	$< 3.5\%$	$< 3.5\%$	$16 - 37\%$
Statistical	$< 1\%$	$< 1\%$	$< 1\%$

The individual contributions for each $|\eta|$ bin are assumed to contribute quadratically to the total systematic uncertainty since the contributions are not correlated within a bin; the systematic uncertainties are correlated between different $|\eta|$ bins.

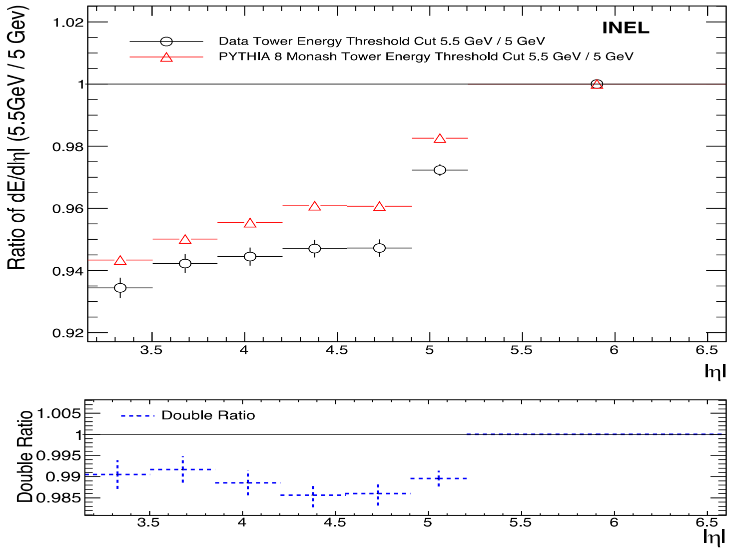

Figure 4.17. Variation of results in data and MC due to variation of the cut applied the energy scale uncertainty for soft-INEL selection.

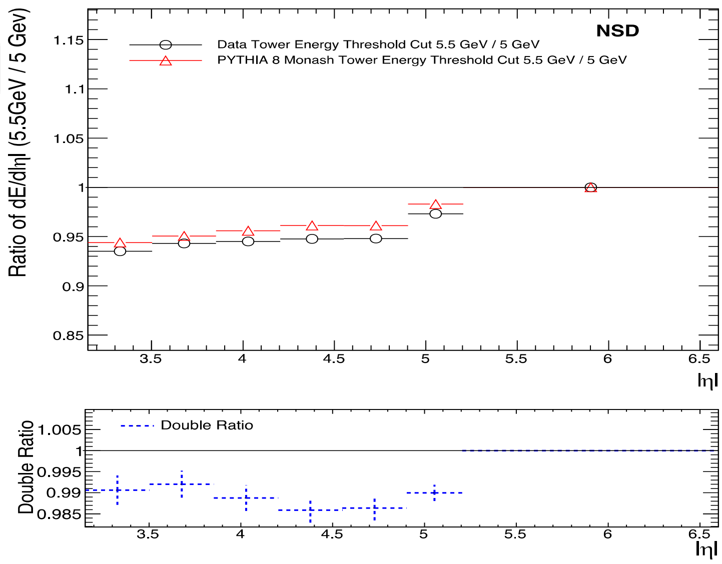

Figure 4.18. Variation of results in data and MC due to variation of the cut applied the energy scale uncertainty for NSD-Enhanced selection

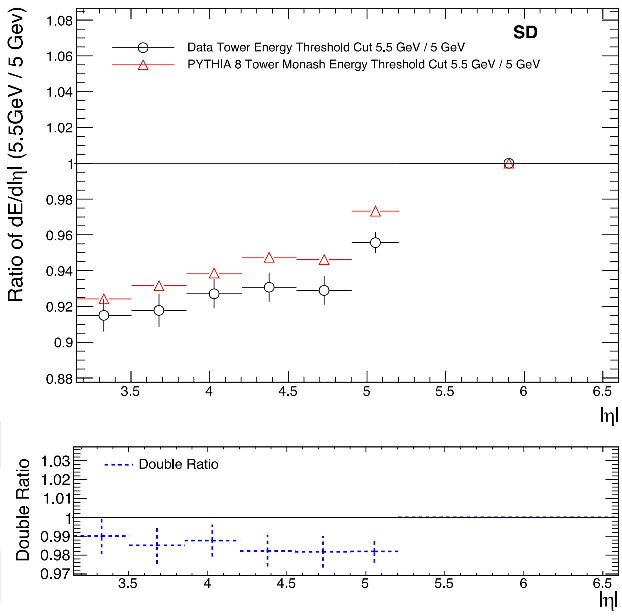

Figure 4.19. Variation of results in data and MC due to variation of the cut applied the energy scale uncertainty for SD-Enhanced selection

4.9 Results

In this analysis, for every pseudorapidity bin, the total detector-level energy is described the CaloTower energy reconstructed with final correction factor which is obtain by using four different MC samples. This final correction factor is used to obtain the particle-level energy flow as a function of $|\eta|$.

A study during analysis is performed to assess the contribution of MPI effect in HF, CASTOR region and high mass diffraction on event selections. This study using data and PYTHIA8 CUETP8M1 tunes with MPI effect (ON-OFF) and mass diffraction (Diffraction:mMinPert=1 and Diffraction:mMinPert=3000) is shown in Figure 4.20. MPI effect-ON corresponds to that the effects of MPI are considered while the meaning of MPI effect-OFF corresponds to that there is no contributions from MPI. The mass diffraction of the system is controlled by parameter of Diffraction:mMinPert. If this parameter value is set to greater than CMS energy than there will be no perturbative explanation at all (PYTHIA8, 2019).

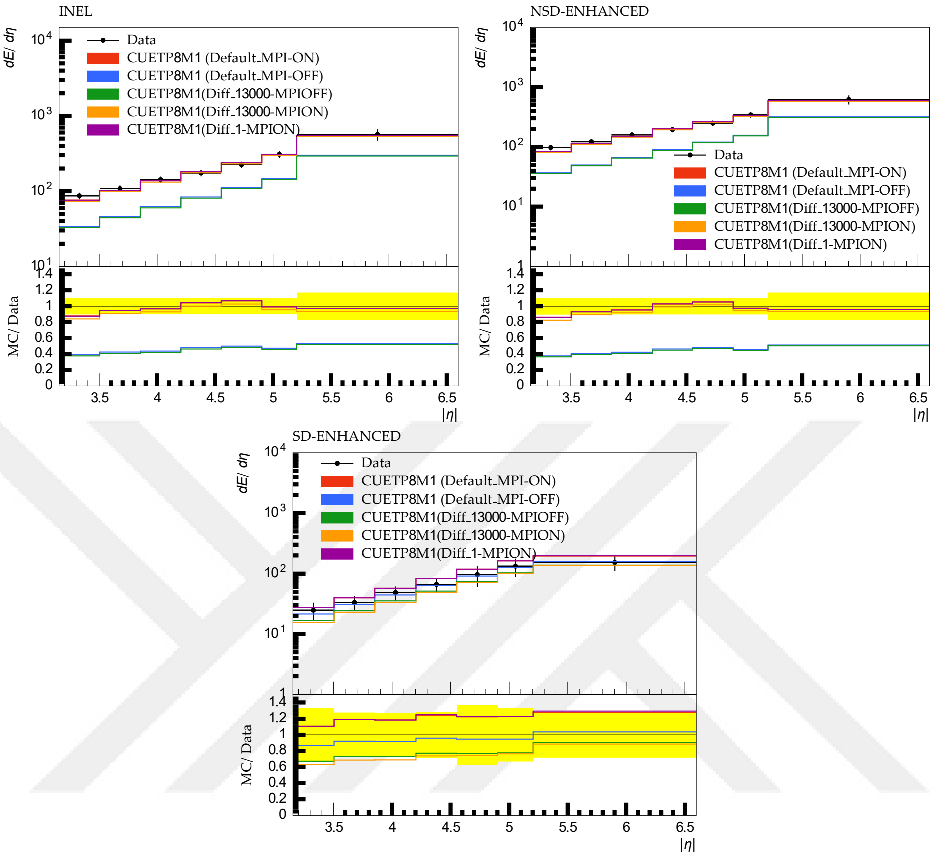

Figure 4.20. Comparisons of the data to PYTHIA8 CUETP8M1 tunes with and without MPI effect. Mass diffraction for each selection

As can be understand from the distribution in Figure 4.20, energy flow measurement is very sensitive to the underlying modelling of MPI, while the effect of mass diffraction is very small for INEL and NSD-Enhanced selection. However, the effect (influence) of mass diffraction is very sensitive for SD-Enhanced selection. In addition, the sensitivity of event selection on MPI is investigated by giving various values (1.8, 2.0 and 2.5) to $P_{T\mathrm{Min}}$ parameters. Figure 4.21 shows the comparison of data to prediction of PYTHIA8 with CUETP8M1Tune by using various value of $P_{T\mathrm{Min}}$ parameters. Furthermore, similar study is performed for different parameters (MultipartonInterections:expPow and

ColourReconnection:Range Parameter). In the PYTHIA8 event generator, the impact parameter dependency is regulated by several parameters. One of them is MultipartonInterections:expPow parameter. This parameter gets value of 1 and varies between 0.4 and 10 (PYTHIA8, 2019).

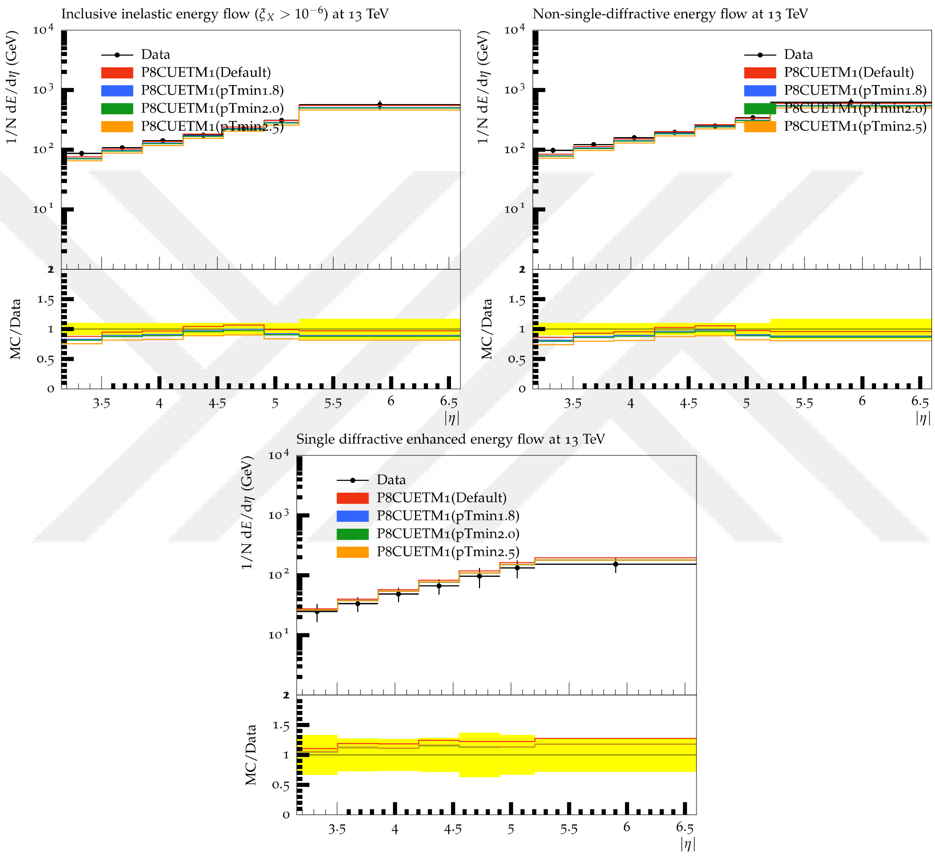

Figure 4.21. Comparisons of the data to PYTHIA8 CUETP8M1 tunes with various values of P_{Tmin} for each selection.

The default value of expPow corresponds to a simple exponential drop, which is not very different from the overlap obtained with the standard double Gaussian parameter. Figure 4.22 shows the study with these parameters for the event selections of INEL(upper left),NSD-Enhanced (upper right) and SD-

Enhanced (Bottom) . QCD colour rules are incorporated in colour reconnection and determine the likelihood of reconnection being allowed. In PYTHIA8, one of the parameters regulating reconnection is ColourReconnection:Range parameter. With the higher value of this parameter more reconnection can occur. For values, greater than unity, the reconnection rate tends to saturate because most systems are already connected with each other (PYTHIA8, 2019).

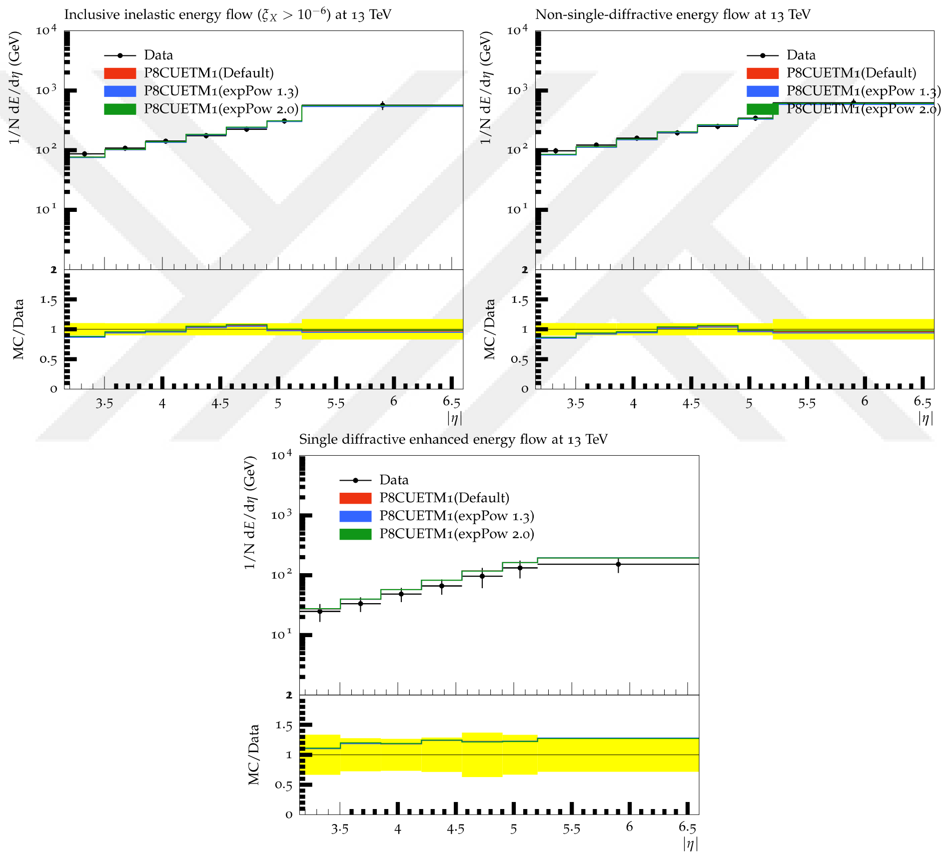

Figure 4.22. Comparisons of the data to PYTHIA8 CUETP8M1 tunes with matter distribution for each selection.

For soft-INEL selection, the measurement of energy density as a function of η in the particle-level is shown in Figure 4.23. Also, data and MC predictions such as PYTHIA8 MONASH13, EPOS-LHC and QGSJETII are compared with each other. Total uncertainty is represented by the grey band. The right plot in Figure 4.23 represents the ratio of MC predictions to measured data. A comparison of the measured energy density to MC simulations for NSD-Enhanced events is given in the left plot of Figure 4.24. The right plot in Figure 4.24 corresponds to the ratio of model predictions to measured data. A similar comparison of the energy density for SD-Enhanced events is shown in the left plot in Figure 4.25, while the right plot corresponds to the ratio of model predictions to measured data. The data in Figure 4.23, Figure 4.24 and Figure 4.25 are indicated by point while model predictions are represented by the dash lines.

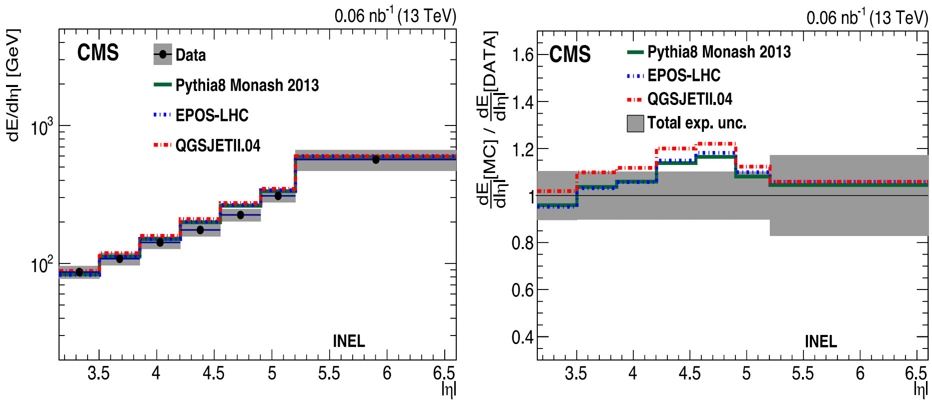

Figure 4.23. Energy density measurement at stable-particle level for soft-INEL events

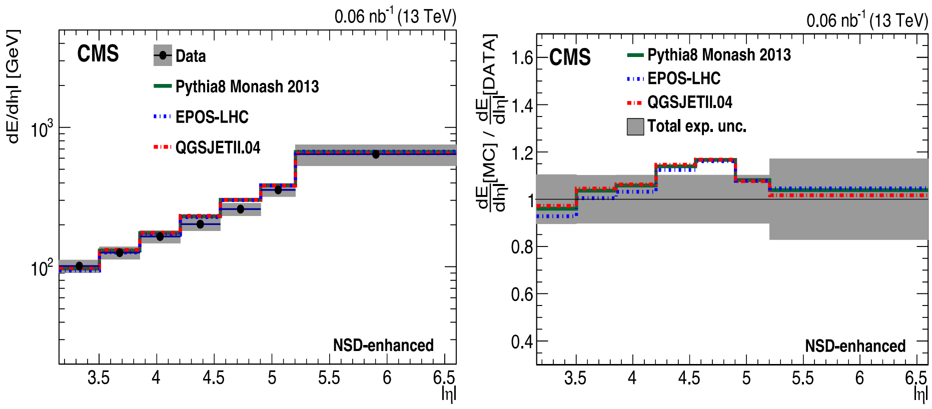

Figure 4.24. Energy density measurement at stable-particle level for NSD-Enhanced

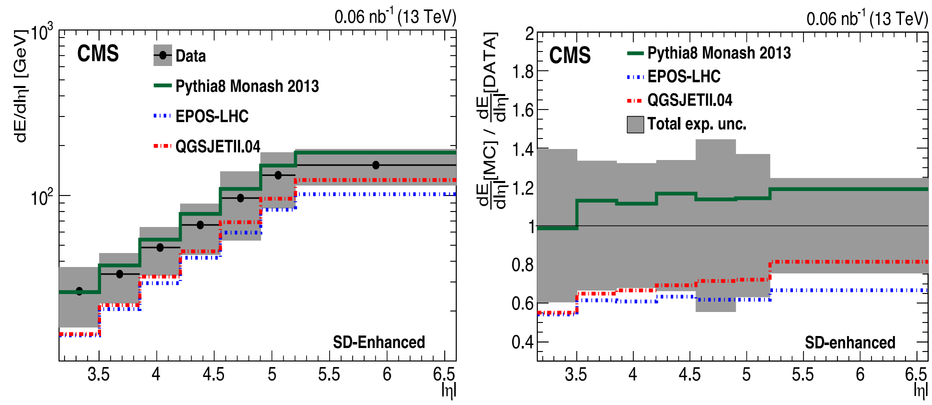

Figure 4.25. Energy density measurement at stable-particle level for SD-Enhanced

Furthermore, in this analysis, a study was performed in order to see the behaviour of PYTHIA8 with different tunes and the effect of the MPI. The measurement of the energy density for INEL selection with measured data and PYTHIA8 MC prediction (tunes of CUETP8M1, CUETP8M1+MBR and CUETP8S1) is shown in Figure 4.26 (left-side). The right plot in Figure 4.26 corresponds to the ratio plot of MC prediction to measured data. The red band corresponds to the envelope of uncertainties of the tune parameters of PYTHIA8 CUETP8S1 tune.

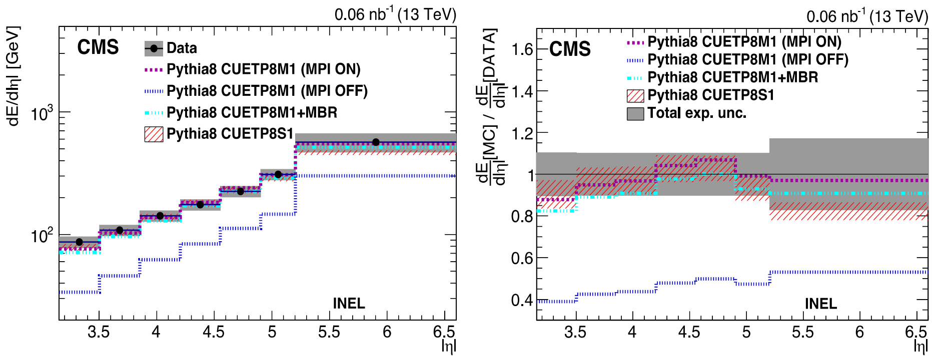

Figure 4.26. Energy density at stable-particle level for INEL selection compared to predictions from PYTHIA8 with tunes CUETP8M1, CUETP8M1+MBR and CUETP8S1. The gray band shows the total systamatic uncertainty. The band around PYTHIA8 CUSETS1 corresponds to the uncertainties of tune parameters. The right panel shows the ratio of model predictions to measured data.

The energy density at stable particle level for NSD-Enhanced selection is shown in Figure 4.27 left side while the ratio plot of MC prediction to measured data is shown in the right side for relevant measurements. The grey band corresponds to total uncertainty.

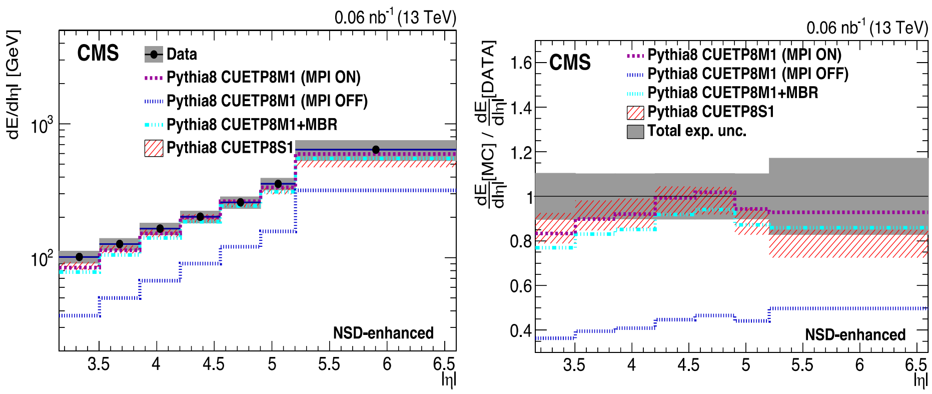

Figure 4.27. Energy density at stable-particle level for NSD-Enhanced selection compared to predictions from PYTHIA8 with tunes CUETP8M1, CUETP8M1+MBR and CUETP8S1. The gray band shows the total systamatic uncertainty. The band around PYTHIA8 CUSETS1 corresponds to the uncertainties of tune parameters. The right panel shows the ratio of model predictions to measured data.

Similar results for SD-Enhanced selection are given in Figure 4.28. The measurement of energy density as a function of $|\eta|$ for SD events is shown in the left side of Figure 4.28. Right side plot of Figure 4.28 shows the ratio of MC prediction to measured data.

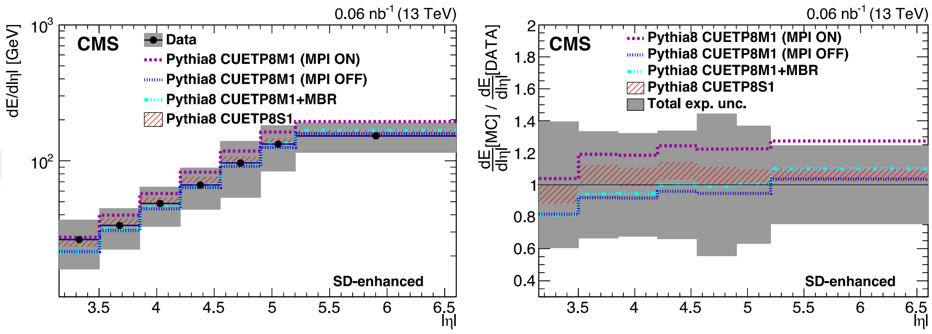

Figure 4.28. Energy density at stable-particle level for SD-Enhanced selection compared to predictions from PYTHIA8 with tunes CUETP8M1, CUETP8M1+MBR and CUETP8S1. The gray band shows the total systematic uncertainty. The band around PYTHIA8 CUSETS1 corresponds to the uncertainties of tune parameters. The right panel shows the ratio of model predictions to measured data.

For a detailed comparison, the transverse energy density, $dE_T/d\eta^{'}$, is compared to the previous published results of the energy density at the lower center-of-mass energy. The whole measurement for NSD-Enhanced event selection is repeated with a reduced energy threshold of 4 GeV to combine all results. Figure 4.29 shows a comparison of corrected transverse energy density as a function of the shifted pseudorapidity ($\eta^{'} = \eta\text{-}y_{beam}$) at different center-of-mass energies.

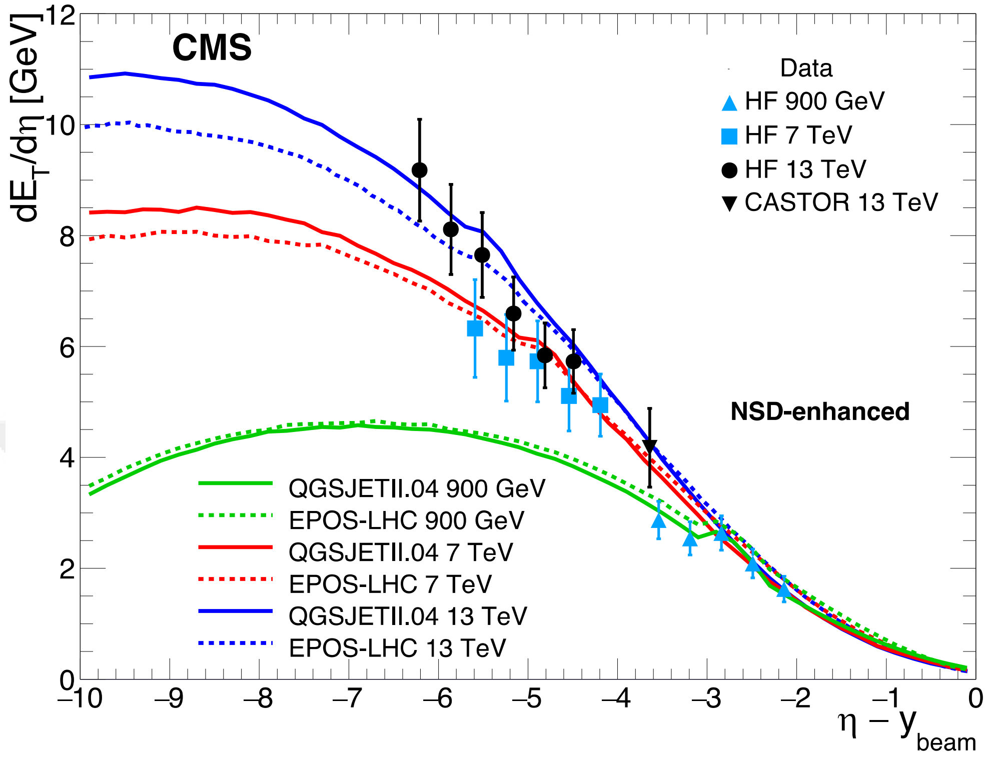

Figure 4.29. A comparison of measurements of transverse energy density as a function of shifted pseudorapidity to different models and earlier published p-p data for several center-of-mass energies for NSD events

In Figure 4.29, The data correspond to points while MC predictions are shown as line. The error bars also indicate the total uncertainties correlated across pseudorapidity bins.

5 SUMMARY AND CONCLUSİONS

In this thesis, the energy density as well as the transverse energy density measurements are performed for three different event selection using CMS data taken at $\sqrt{s} = 13$ TeV center-of-mass energy. These measurements include HF ($3.15 < |\eta| < 5.20$) and CASTOR ($-6.6 < \eta < -5.2$) regions. The results from these measurements are compared to the MC models tuned to describe high-energy hadronic interaction (PYTHIA8) and predictions used cosmic ray physics (EPOS-LHC and QGSJETII.04) for three different selections (soft-inclusive-inelastic-(INEL), non-single-diffractive (NSD) -Enhanced and single-diffractive (SD)-Enhanced).

According to the results, INEL and NSD-Enhanced events are intensely sensitive to multi-parton interactions but SD-Enhanced events essentially unaffected from MPI (see Figure 4.26, Figure 4.27 and Figure 4.28), while EPOS-LHC, QGJETII.04 (cosmic ray models) and PYTHIA8 MONASH tune define the data well at $|\eta| < 4$. These predictions overshoot the data around $|\eta| \approx 4.5$. The differences between model predictions for NSD-Enhanced events are smaller compared with INEL events. The predictions of PYTHIA8 with CUETP8M1, CUETP8M1+MBR and CUETP8S1 tunes have the best description of data for INEL events. QGSJETII.4 overestimate the measurement, except for the first and last bins while EPOS-LHC and PYTHIA8 MONASH13 describe the data within the uncertainties. For SD-Enhanced events, while the all prediction of PYTHIA8 tunes overestimates the data within uncertainty band both QGSJETII and EPOS-LHC models underestimate the data. As a mention, multi-parton interactions in simulations has no impact on the model predictions for SD-Enhanced events thus SD-Enhanced event selection is an effective way to minimize the effect of the MPI.

In this analysis, the measurement of transverse energy density, $dE_T/d\eta^{'}$, ($E_T = \cosh(\eta)$) are performed in p-p collision at $\sqrt{s} = 13$ TeV center-of-mass energies and compared with different center-of-mass-energies. The EPOS-LHC and QGSJETII.04 models describe the combined data well in the forward pseudorapidity range close to projectile fragmentation region. The mechanism of limiting fragmentation is supported according to the result obtained from the analysis.

REFERENCES

Altarelli, G. e. (1977). *Asymptotic freedom in parton language.* Nuclear Physics B.

ATLAS Collaboration. (2012). *Measurements of the pseudorapidity dependence of the total transverse energy in proton-proton collisions at √s= 7 TeV with ATLAS.* JHEP 11.

Bartalini, P. a. (2011). *Multi-Parton Interactions at the LHC.*

Bayatian G. L. et al. (2006). *Tehcnical Design Report, Volume I: Detector Performance and Software.* CMS TDR 8.1, CERN/LHCC.

Bayatian G.L., et al. (2000). *CMS Collaboration CMS TriDAS project: Technical Design Report, Volume 1: The Trigger Systems.* CERN-LHCC-2000-038.

Brock, C. I.-S. (2011). *Physics at Trescale.* WILEY-VCH.

Cerci, Sunar Cerci, Zorbilmez et al. (2015). *Measurement of the pseudorapidity dependence of the energy and transverse energy flow in pp collisions at √s = 13 TeV with CMS.*

Chatrchyan S.,et al. (2008). *The CMS experiment at the CERN LHC.* JINST 3 S08004.

CMS Collaboration. (1997a). *The Electromagnetic Calorimeter Project: Technical Design Report.* CERN-LHCC-97-033.

CMS Collaboration. (1997b). *CMS Hadronic Calorimeter Project Technical Design Report.* CERN/LHCC-97-31.

CMS Collaboration. (1997c). *CMS Magnet Technical Design Report.* CERN/LHCC-97-10.

CMS Collaboration. (2002). *CMS: The TriDAS project. Technical design report, Vol. 2: Data acquisition and high-level trigger.* CERN-LHCC-2002-026.

CMS Collaboration. (2011). *Measurement of energy flow at large pseudorapidities in pp collisions at √s = 0.9 and 7 TeV.* JHEP.

CMS Collaboration. (2013). *Study of the underlying event at forward rapidity in pp collisions at √s = 0.9, 2.76, and 7 TeV.* JHEP.

CMS Collaboration. (2015). *Centrality and pseudorapidity dependence of transverse energy flow in pPb collisions at √sNN=5.02 TeV.*

CMS Collaboration. (2016). *Event generator tunes obtained from underlying event and multiparton scattering measurements.* Eur. Phys. J. C.

CMS Collaboration. (2017a). *Measurement of the inclusive energy spectrum in the very forward direction in proton-proton collisions at √s=13 TeV.* JHEP.

CMS collaboration. (2017b). *Measurement and QCD analysis of double-differential inclusive jet cross sections in pp collisions at √s = 8 TeV and cross section ratios to 2.76 and 7TeV.* JHEP03(2017)156.

CMS Collaboration. (2019). *Measurement of the energy density as a function of pseudorapidity in proton–proton collisions at √s = 13 TeV.* Eur. Phys. J. C (2019) 79:391.

Connor, P. L. (2014). *Study of the Drell-Yan Process at High Invariant Mass at LHC.* CERN THESIS-2014-418.

David d'Enterria et all. (2008). *Cosmic-ray Monte Carlo predictions for forward particle production in p-p, p-Pb, and Pb-Pb collisions at the LHC.*

Driesch, M. (2016). *On parton showers and multi parton interaction.* Hamburg.

Ebert, T. (1995). *Hadronic Energy Flow in Deep Inelastic Electron-Proton Scattering and Proton Structure at Low Bjorken x.* Liverpool.

Ellis, R. K. (2003). *QCD and collider physics.* United Kingdom: CAMBRIDGE UNIVERSITY PRESS.

Evans L. and Bryant, P. e. (2008). *LHC Machine.* JINST 3 S08001.

Goulianos, R. C. (2013). *MBR Monte Carlo Simulation in PYTHIA8.* PoS ICHEP2012.

Gunnellini, P. (2014). *Study of double Parton scattering using four-jet scenarios in proton-proton collision at √s = 7 TeV with the CMS experiment at Large Hadron Collider.*

Gwenlan, C. (2003). *Jets and Energy Flow in Photoproduction using the ZEUS Detector at HERA.* London.

Haevermaet, H. V. (2013). *Study of Underlying Event at Forward rapidity in pp Collisions at √s = 0.9 , 2.76 and 7 TeV.*

Hess, V. F. (1912). *Über Beobachtungen der durchdringenden Strahlung bei sieben Freiballon- fahrten.* Physikalische Zeitschrift.

Hos, I. (2016). *Measurements of Inclusive Low-pt Jets Cross-section and Azimuthal Angle Decorrelation of Jets with Large Rapidity Separation using Run 1 CMS Data.* Adana.

J. Pumplin et al. (2002). *New generation of parton distributions with uncertainties from global QCD analysis.* JHEP.

Khachatryan, V. e. (2017). *Measurement and QCD analysis of double-differential inclusive jet cross sections in pp collisions at √s = 8 TeV and cross section ratios to 2.76 and 7 TeV.* Springer Berlin Heidelberg JHEP.

Klundert, M. H. (2018). *Search for gluon saturation in proton-lead collisions at √s = 5.02 TeV with the very forward CASTOR calorimeter at the CMS experiment.*

Lambacher, M. (2007). *Study of full hadronic tt ̄decays and their separation from QCD multijet background events in the first year of the ATLAS experiment.* Munich.

Ledwig, O. (2017). *Next-to-leading order QCD corrections to the Drell-Yan process.*

LHCb Collaboration. (2013). *Measurement of the forward energy flow in pp collisions at √s = 7 TeV.* Eur. Phys. J.

Martin, B. R. (2006). *Nuclear and Particle Physics.* John Wiley & Sons Ltd.

Muta, T. (2009). *Foundations of Quantum Chromodynamics.* World Scientific .

Nathvani, R. (2017, 05 11). *Quantum Diares*. www.quantumdiaries.org: https://www.quantumdiaries.org/tag/proton-structure/ adresinden alındı

NNPDF Collaboration. (2013). *Parton distributions with LHC data.* Nucl. Phys. B.

Ostapchenko, S. (2011). *Monte Carlo treatment of hadronic interactions in enhanced Pomeron scheme: I. QGSJET-II model.* Phys. Rev. D.

P. Skands, S. C. (2014). *Tuning PYTHIA 8.1: the Monash 2013 Tune.* Eur. Phys. J. C.

P. V. Mechelen et al. . (2015). *Measurement of the inelastic proton-proton cross section at sqrt(s)=13tev.* CMS Note 2015/118,.

Perkins, D. H. (2000). *Introduction to High Energy Physics.* Cambridge University Press.

Pierog, T. e. (2015). *EPOS LHC: Test of collective hadronization with data measured at the CERN Large Hadron Collider.* Phys. Rev. C.

PYTHIA8.(2019, 08 11). http://gpppc6.lps.umontreal.ca/azuelos/Documentation/ pythia8201/htmldoc/Welcome.html

Robson, B. (2017). *The Generation Model of Particle Physics.*

Sen, N. (2011). *Measurement of Energy Flow at Large Pseudorapidities for sqrt(s) = 0.9 and 7 TeV at Large Hadron Collider using Compact Muon Solenoid.* Hamburg.

Sirunyan, A. M. (2016). *Measurement of the pseudorapidity dependence of the energy and transverse energy density in pp collisions at √s = 13 TeV with CMS.*

Sjöstrand, T. a. (2015). *AnIntroductiontoPYTHIA8.2.* Comput.Phys.Commun.

Stanev, T. (2010). *High Energy Cosmic Rays.* Springer-Verlag.

Sunar, D. (2009). *Measurement of K (892) Production in Deep Inelastic ep Scattering with H1 detector at HERA .*

Thomson, M. (2013). *Modern Particle Physics.* Cambridge University Press.

V. Andreev et al. (2010). *Performance studies of a full-length prototype for the CASTOR forward calorimeter at the CMS experiment.* Eur. Phys. J. C 67.

Volyanskyy, D. (2010). *Forward Physics with the CMS Experiment at the Large Hadron Collider.* ARXIV:1011.5575.

Zorbilmez, C. (2018). *Enerji Yoğunluğunun Psüdorapitidenin Fonksiyonu olarak √s=13 TeV'lik Kütle merkezi Enerjisinde Ölçülmesi* . 1st National Workshop on CERN Activities.

CURRICULUM VITAE

He was born on February 3, 1981 in Adana and graduated from the Department of Physics of Çukurova University in 2006. He got master degree in High Energy Physics in Çukurova University in 2012 by working in CMS experiment at the CERN. Later that same year he began his doctoral studies at Çukurova University by working in CMS experiment.